

AVAILABLE TO THE PUBLIC

BOEING

FACILITY FORM 60-1

g Co.)
(ACCESSION NUMBER)
120
(PAGES)
CR-114424
(NASA CR OR TMX OR AD NUMBER)

20 p

(THRU)
G3

(CODE)
82

(CATEGORY)

Unclas
18461



D210-10347-1

September 1971

AN EXPERIMENTAL INVESTIGATION OF THE
HELICOPTER ROTOR BLADE ELEMENT AIRLOADS
ON A MODEL ROTOR IN THE BLADE STALL REGIME

by

Richard K. Fisher, Jr.
Jerome E. Tompkins
Christopher J. Bobo
Richard F. Child

Distribution of this report is provided in the interest of information exchange. Responsibility for the contents resides in the author or organization that prepared it.

Prepared under Contract NAS2-5473 by
THE BOEING COMPANY, Vertol Division
Boeing Center, P.O. Box 16858
Philadelphia, Pennsylvania 19142

for

NATIONAL AERONAUTICS AND SPACE ADMINISTRATION

PRECEDING PAGE BLANK NOT FILMED

SUMMARY

A wind tunnel test program was conducted on an eight foot diameter model rotor system to determine blade element airloads characteristics in the unstalled and stalled flight regimes. The fully articulated model rotor system utilized three blades with a Vertol 23010-1.58 airfoil section, the blades being 1/7.5 scale models of the CH-47C rotor blades. Instrumentation was incorporated at the blade 75% radial station to measure pressure and skin friction distributions, surface streamline directions and local angle of attack. The test program was conducted in three phases; non-rotating, hover and forward flight at advance ratios of 0.15, 0.35 and 0.60.

Test data were analyzed with respect to providing insight to the mechanisms affecting blade stall, particularly retreating blade stall during forward flight conditions. From such data, an assessment was made as to the applicability of current theoretical analyses used for the prediction of blade element airloads in the stall regime. These analyses utilize empirical corrections to account for portions of three dimensional, unsteady environment; namely, the oscillating airfoil motion and the swept wing effects.

The test results have indicated that the blade stalling process is delayed in comparison with a static, two-dimensional airfoil. The stalling process appears to be a sequence of events that develop over a significant segment of the rotor azimuth, rather than a sharp and distinct breakdown of the flow field. These events can be identified as follows:

1. Onset of separation-like disturbances within the boundary layer and a slight shift of the center of pressure.
2. Beginning of a rapid rearward shift of the center of pressure and an increase in C_m .
3. Collapse of the leading edge suction peak.
4. Achievement of maximum C_n .
5. Achievement of maximum C_m .
6. Completion of the stalling process.

These observed stall events provide support to the hypothesis that retreating blade stall is a phenomenon of three major phases: (a) a dynamic overshoot of leading edge suction and $C_{n_{max}}$, (b) a subsequent loss of leading edge suction and the shedding of circulation in some form, perhaps as a modified vortex, from the leading edge region, and (c) complete upper surface separation.

Prior to the commencement of the stalling process, the test data indicate that the three-dimensional nature of the flow field does not significantly affect the blade element airloads. Rather, the forces and moments resemble those that have been observed on two-dimensional airfoils oscillating in pitch. Correlation of test data with the aforementioned theoretical analyses indicates that the current empirical theories that account for three-dimensional unsteady effects can adequately predict blade element airload on the advancing blade and during the onset of stall, but not after complete blade stall has occurred. These shortcomings are attributed to uncertainties in the blade element angle of attack, the local dynamic pressure and in the basic behavior of unsteady three-dimensional separated flow fields.

The analysis has drawn heavily on the skin friction gage data, none of which is presently in suitable form for publication. These data will be incorporated into a subsequent report available from Dr. W. J. McCroskey.

TABLE OF CONTENTS

	<u>Page</u>
SUMMARY	iii
LIST OF ILLUSTRATIONS	vi
LIST OF SYMBOLS	x
TEST EQUIPMENT	4
Wind Tunnel	4
Dynamic Rotor Test Stand	4
Rotor Blades	4
Pressure Transducers	7
Skin Friction Gages	10
Differential Pressure Transducer and Angle of Attack Measurement Technique	15
Blade Loads and Motion Gages	18
Data Acquisition System	17
TEST PROGRAM	26
Test Procedure	26
Instrumentation Problems	28
Data Reduction	29
Data Analysis	30
TEST RESULTS AND DISCUSSION	33
Nonrotating (Static) Testing	33
Hover Testing	37
Forward Flight	39
Additional Comments on the Airloads in Stall	85
CONCLUSIONS	91
APPENDIX	93
REFERENCES	108

LIST OF ILLUSTRATIONS

<u>Figure</u>		<u>Page</u>
1	Effects of Empirical Radial Flow and Unsteady Corrections on Rotor Performance.....	3
2	Pressure Blades Mounted on Dynamic Rotor Test Stand.....	5
3	Vertol 23010-1.58 Airfoil.....	6
4	End to End System Calibration Check Through Data Acquisition System.....	8
5	Pressure Transducer Installation in the Rotor Blade.....	9
6	Rotor Blade Instrumentation.....	13
7	Effect of Sweep Angle on Leading Edge Differential Pressure.....	17
8	Effect of Mach Number on Leading Edge Differential Pressure.....	19
9	Effect of α On Leading Edge Differential Pressure.....	20
10	Comparison of Model Scale and Full Scale Angle of Attack Measurements.....	21
11	Calibration Results of Leading Edge Differential Pressure Angle of Attack Transducer.....	22
12	Data Acquisition System.....	23
13	Data Reduction Flow Path.....	25
14	Comparison of Full-Scale and Model Section Airload Characteristics.....	34
15	Statically Obtained Pressure Distributions.....	35
16	Statically Obtained Pressure Distributions.....	36

<u>Figure</u>		<u>Page</u>
17	Effect of Engineering Approximations on Blade Element Aerodynamic Coefficients.....	38
18	Hover Performance, $V_T = 250$ FT/SEC.....	40
19	Comparison of Hover and Static Pressure Distribution.....	41
20	Comparison of Hover and Static Pressure Distributions.....	42
21	Decay of Rotor Sensitivity to α_g	44
22	Rotor Performance AT $\mu = .15$, $V_T = 250$ FPS.....	45
23	Rotor Performance AT $\mu = .35$, $V_T = 250$ FPS.....	46
24	Rotor Performance at $\mu = .6$, $V_T = 250$ FPS.....	47
25	Rotor Propulsive Efficiency at $C_T'/\sigma = .08$, $V_T = 250$ FPS.....	48
26	Model Rotor Performance Data in Forward Flight.....	50
27	Measured Angles of Attack on the Pressure and Skin Friction Blades.....	51
28	Aerodynamic Coefficients Obtained from Integrated Pressures @ $r/R = 0.75$ $\mu = .35$, $\theta_{.75} = 13.5$, $V_T = 500$ FPS.....	52
29	Aerodynamic Coefficients Obtained From Integrated Pressures @ $r/R = 0.75$ $\mu = .35$, $\theta_{.75} = 13.5$, $V_T = 500$ FPS.....	53
30	Aerodynamic Coefficients Obtained From Integrated Pressures @ $r/R = 0.75$ $\mu = .35$, $\theta_{.75} = 13.5$, $V_T = 500$ FPS.....	54
31	Maximum Blade Loads.....	56
32	Measured Airloads at $V_T = 500$ fps and Various Thrust Levels, $\mu = 0.35$	57

<u>Figure</u>		<u>Page</u>
33	Lift Hysteresis Prior to Signs of Rotor Stall..	59
34	Lift Hysteresis With Blade Stall.....	60
35	Theoretical Rotor Section Airfoil Characteristics Using Empirical Radial Flow and Unsteady Corrections.....	61
36	Pressure Distribution at Various Azimuth Locations.....	62
37	Pressure Distribution at Various Azimuth Locations.....	64
38	Comparison of Rotating and Nonrotating Lift and Moment Data.....	65
39	Blade Element Elastic Twist and Airloads.....	67
40	Map of Stall Events, $\mu = .35$, $V_T = 500$ FPS.....	68
41	Map of Stall Events - $\mu = .35$, $V_T = 250$ FPS....	70
42	Comparison of Blade Element Airloads at $V_T = 250$ and $V_T = 500$ FPS.....	71
43	Map of Stall Events - $\mu = .15$, $V_T = 250$ FPS...	73
44	Blade Element Airloads Below Stall $\mu = .15$, $C_T/\sigma = .08$	74
45	Blade Element Airloads in Stall Region $\mu = .15$, $C_T/\sigma = .126$	75
46	Blade Element Airloads at $\mu = .15$	76
47	Blade Element Pressure Distributions.....	77
48	Blade Element Pressure Distributions.....	78
49	Blade Element Pressure Distributions at an Advance Ratio of .6, $C_T/\sigma = .09$, $V_T = 400$ FPS...	80
50	Blade Element Airloads at an Advance Ratio of .6.....	81

<u>Figure</u>		<u>Page</u>
51	Blade Element Pressure Distributions at an Advance Ratio of .6, $C_{T/\sigma} = .09$, $V_T = 400$ FPS.	82
52	Blade Element Airloads at an Advance Ratio of .6.....	83
53	Map of Stall Events - $\mu = .6$, $V_T = 250$ FPS...	84
54	Comparison of Angles of Attack With Blade Stall.....	86
55	Correlation of Theoretical and Experimental Normal Force Coefficients.....	87
56	Correlation of Theoretical and Experimental Normal Force Coefficients.....	90

LIST OF SYMBOLS

<u>Symbol</u>	<u>Description</u>	<u>Units</u>
α	Lift curve slope	Radians ⁻¹
b	Number of blades	N.D.
c	Blade chord	Feet
C_c	Blade element chord force coefficient $\frac{C}{q c}$	N.D.
C_d	Blade element drag coefficient $\frac{D}{q c}$	N.D.
C_{D_E}	Rotor equivalent drag coefficient $\left(\frac{P/V - X}{q d^2 \sigma}\right)$	N.D.
C_f	Skin friction coefficient	N.D.
C_l	Blade element lift coefficient $\frac{L}{q c}$	N.D.
C_m	Blade element pitching moment coefficient $\frac{M}{q c^2}$	N.D.
C_N	Blade element normal force coefficient $\frac{N}{q c}$	N.D.
C_p	Pressure coefficient P/q	N.D.
C_T/σ	Rotor thrust coefficient	N.D.
C'_T/σ	Rotor lift coefficient	N.D.
d	Rotor diameter	Feet
k	Reduced frequency parameter $\frac{C \Omega}{2V}$	N.D.
M	Mach number	N.D.
P	Rotor power	Ft.-lb/sec.
p	Measured pressure	lb/ft ²

<u>Symbol</u>	<u>Description</u>	<u>Units</u>
q	Dynamic pressure $\frac{1}{2} \rho V^2$	lb/ft ²
Q	Rate of convective heat transfer	
r	Blade radial station	Feet
R	Blade radius	Feet
Re	Reynolds number based on chord	N.D.
u_p	Total of velocity components perpendicular to rotor disc plane at a blade station	Feet/sec.
u_T	Total of velocity components parallel to rotor disc plane at a blade station	Feet/sec.
V	Free stream velocity	Feet/sec.
V_T	Rotor tip speed	Feet/sec.
x	Blade element chordwise location measured from leading edge	Feet
X	Rotor propulsive force	Pounds
y	Blade element surface location measured perpendicular to chord line	Feet
μ	Advance ratio	N.D.
α	Blade element angle of attack	Degrees
α_c	Calculated blade element angle of attack	Degrees
α_{CA}	Rotor control axis angle	Degrees
α_{M_1}	Measured blade element angle of attack	Degrees
α_{M_2}	Angle of attack determined from dynamic C_N	Degrees

<u>Symbol</u>	<u>Description</u>	<u>Unit</u>
$\alpha_{m,c}$	$\alpha_{m,}$ corrected for leading edge velocity due to blade feathering motion	Degrees
α_s	Rotor shaft angle	Degrees
β	Blade flapping angle	Degrees
θ_o	Blade collective pitch at centerline of rotation	Degrees
θ_{lc}	Lateral cyclic pitch	Degrees
θ_{ls}	Longitudinal cyclic pitch	Degrees
$\theta_{.75}$	Collective pitch at 75 percent radius	Degrees
θ_e	Pitch angle due to blade elasticity	Degrees
λ	Rotor inflow ratio	N.D.
ρ	Density	Slugs/Ft ³
σ	Rotor solidity $\frac{bc}{R}$	N.D.
ψ	Blade azimuth angle	Degrees
Ω	Rotor speed	Radians/sec.
Λ	Blade sweep angle	Degrees

INTRODUCTION

The application of quasistatic, two-dimensional airfoil data to describe the helicopter rotor blade environment has been shown by many researchers to be inadequate for prediction of rotor performance, rotor blade loads, and blade motion at the higher forward speeds and thrusts being experienced by the current generation of helicopters. With the advent of the more sophisticated digital and analog computers to aid in the solution of the rotor problem, effects characteristic of the three-dimensional dynamic environment (heretofore assumed small) can be included in rotor theoretical analyses. The nature of these effects, though, is not clearly understood.

Tests previously conducted on an oscillating airfoil, (Reference (1)), and on an airfoil undergoing a rapid transient change of angle of attack, (Reference 2), have provided instructive data on unsteady aerodynamic effects as well as considerable insight into the dynamic stall mechanism. Tests conducted on swept two-dimensional wings, (Reference 3), have shown that spanwise flow effects have a pronounced impact on the measured airloads.

Attempts at empirically modeling these unsteady and three-dimensional effects have been made. Utilizing the principal of superposition, Harris, et al (Reference 4), took into account both the airload characteristics exhibited by a wing when swept and those characteristics associated with an airfoil undergoing pitching motion and generated an improved rotor theory (Figure 1). These effects, when integrated over the rotor disc area, improved the correlation of rotor performance with test data. However, it was not established in that study that the predicted blade element airload characteristics were indeed representative of those in the rotor environment. Also, it was apparent that knowledge about the detailed behavior of the flow in the boundary layer was needed.

Therefore, the present investigation was undertaken to answer three questions:

1. How do measured blade element airloads compare with current rotor blade load empirical methods which account for the three-dimensional unsteady environment?
2. How realistically do the oscillating airfoil stall effects and swept-wing effects represent the actual mechanisms of

the rotor blade element stall?

3. Have any basic factors been overlooked in the formulation of the rotor blade environment?

To this end, an experimental program was designed to:

1. Obtain measured blade element airload trends and representative measured boundary layer flow characteristics in the rotor stall regime.
2. Compare theory to test measurements of rotor blade airloads and blade element angle of attack.
3. Enhance the understanding of the mechanisms of blade stall.

The experimental program consisted of testing an extensively instrumented three-bladed model rotor in both hover and forward flight regimes. Absolute pressure transducers, located at the 75-percent radial station, were used to measure blade element airloads. Skin friction gauges, located near the 75-percent radial station on another blade, were used to measure boundary layer flow characteristics. Blade element angle of attack was also measured, using a differential pressure transducer. Blade root torsion and flap angle were also recorded.

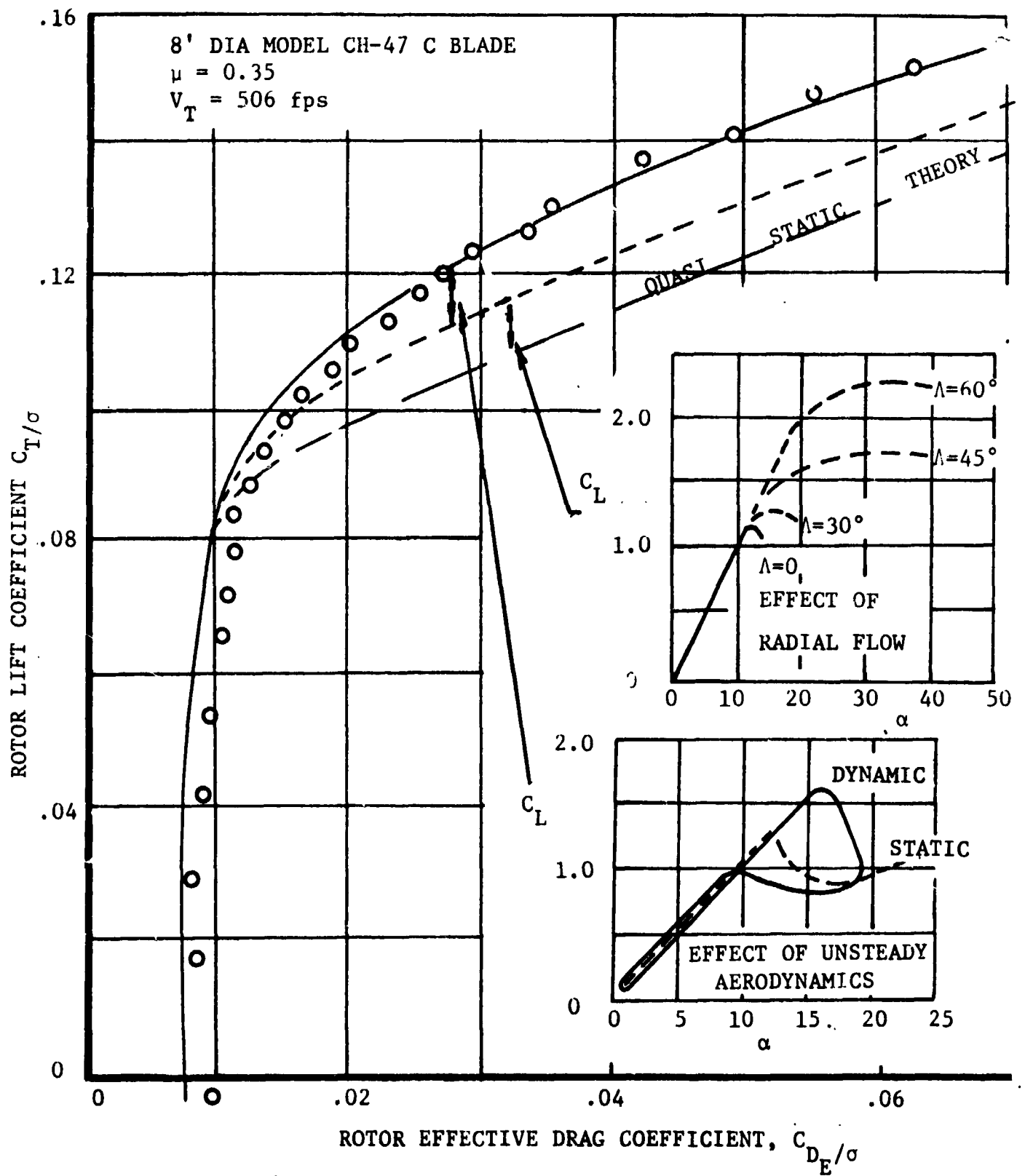


FIGURE 1 EFFECTS OF EMPIRICAL RADIAL FLOW AND UNSTEADY CORRECTIONS ON ROTOR PERFORMANCE

TEST EQUIPMENT

Wind Tunnel

The test program was conducted in the Boeing V/STOL Wind Tunnel in Ridley Township, Pennsylvania. The tunnel, a closed-circuit, single-return type with a rectangular test section (20 x 20 feet), can be operated in three basic configurations: solid, slotted, or open-jet. A maximum test section speed of approximately 260 knots is attainable in the solid-wall configuration. The circuit is cooled by an exchange system with exhaust doors located upstream of the bell mouth and intake doors located downstream of the test section. Power to drive the tunnel fan is supplied by a 13,700-horsepower AC motor and a 1,500-horsepower DC motor.

Dynamic Rotor Test Stand

The dynamic rotor test stand (DRTS) used during this model test was designed at the Vertol Division for use in testing single rotor configurations with blades up to 16 feet in diameter. The DRTS is sting-mounted for both hover and forward flight testing. The stand housing is pivoted such that the rotor shaft angle can be pitched forward 30 degrees and aft 20 degrees by a remotely controlled actuator. Rotor system collective pitch can be remotely controlled in the range 0 to 30 degrees, and the longitudinal and lateral cyclic pitch have maximum ranges of control of +10 to -6 degrees and ± 7 degrees respectively. A six-component strain gauge balance is incorporated into the DRTS to measure steady and vibratory rotor loads. Power is supplied to the DRTS by either a 120-horsepower or a 400-horsepower motor with six gearbox reduction ratios available. A photograph of the model rotor, mounted on the DRTS in the Boeing V/STOL Wind Tunnel is shown in Figure 2.

Rotor Blades

The rotor blades used in the test program are geometrically scaled models of the production CH-47B blades. The blades were tested in a three-bladed rotor system configuration with constant chord and linear twist variation along the span. The airfoil section used was the Vertol 23010-1.58 shown in Figure 3.

BOEING VERTOL WIND TUNNEL TEST 054

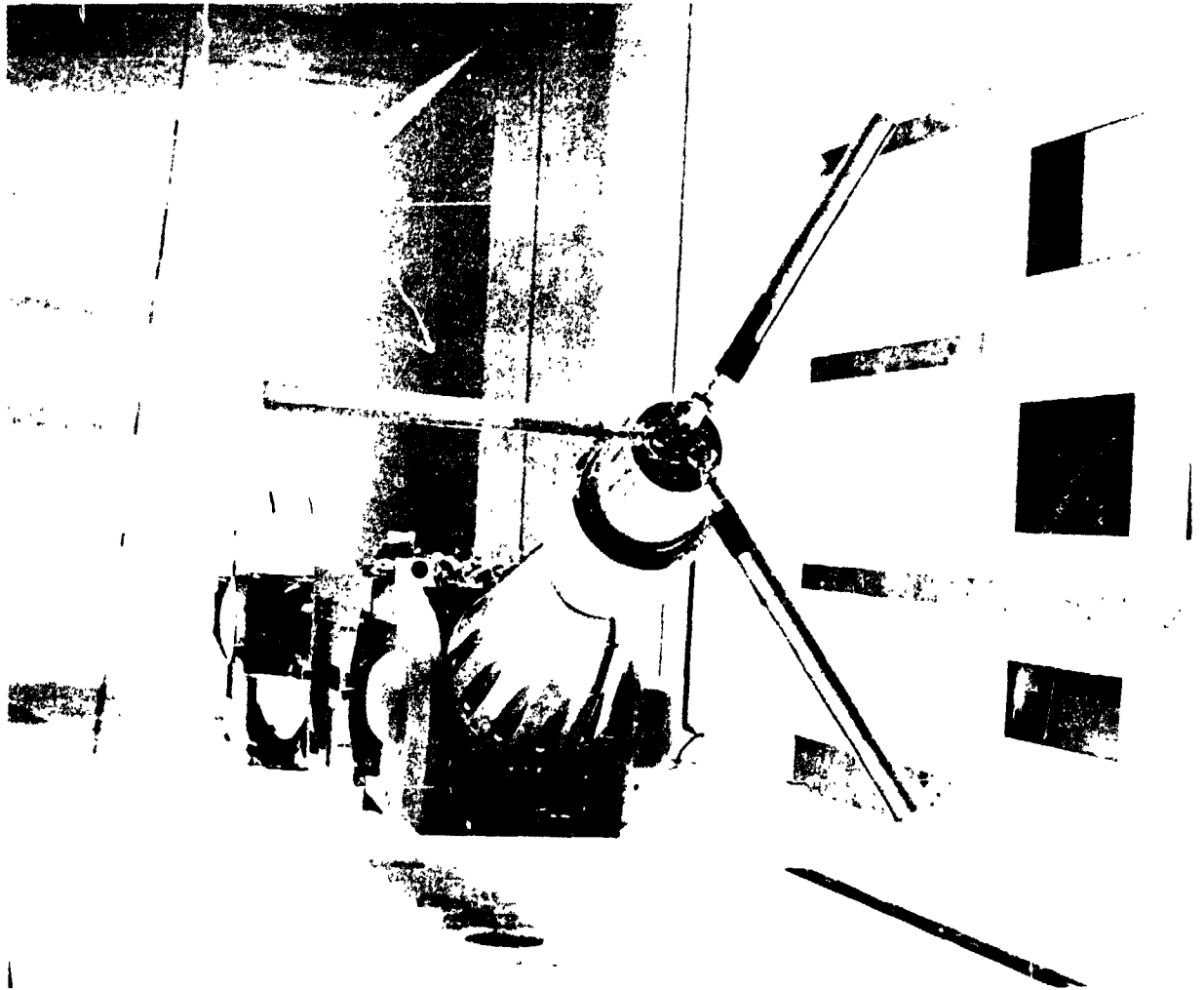
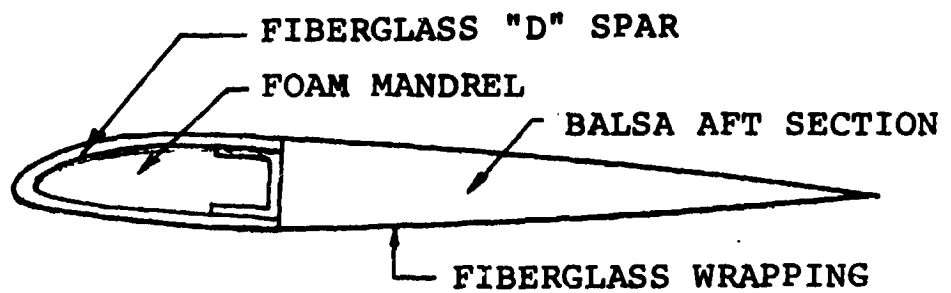
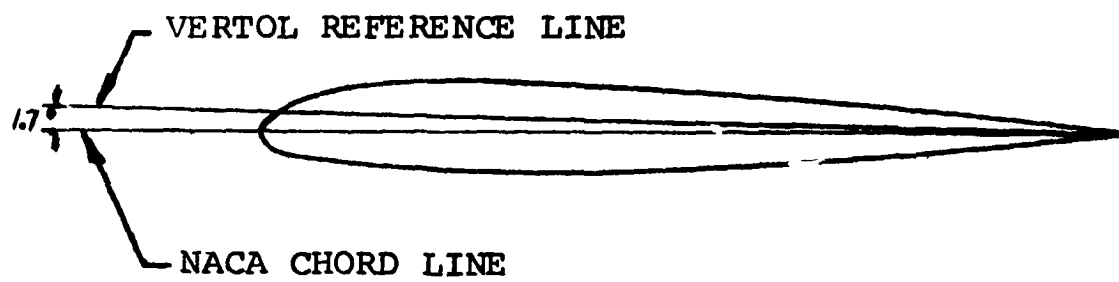


FIGURE 2 PRESSURE BLADES MOUNTED ON DYNAMIC ROTOR TEST STAND

AIRFOIL CONTOUR



BLADE CONSTRUCTION

FIGURE 3

VERTOL 23010-1.58 AIRFOIL

The blades are constructed in two basic subassemblies; the spar and the aft section. Figure 3 provides a sketch of a typical blade cross-section. The spar is a "D" section of Scotch uniply fiberglass built up around a formed mandrel of foamed plastic which then becomes an integral nonstructural part of the blade. This subassembly is then cured under pressure at high temperature. The aft portion of the blade is comprised of balsa, which is joined to the aft section of the spar by a fiberglass wrapping around the entire assembly and bonded in a final assembly mold.

Since chordwise pressure distributions were required in this program, certain structural modifications were incorporated to accommodate pressure sensing instrumentation. Depressions of .040 inch depth into the spar and .030 inch depth into the balsa aft section were formed at the 75-percent radial station to accommodate the extensive instrumentation to be located there. These modifications permitted the transducers to be mounted below the airfoil surface and hence, a smooth, properly contoured airfoil surface could be maintained at this radial station.

Basic data for the blades are as follows:

Airfoil designation	- Vertol 23010-1.58
Chord	- 3.336 inches
Diameter	- 8.0 feet
Twist	- -10.8 degrees
Root cutout	- .192R
Solidity	- .067

Pressure Transducers

The transducers used for this test were Kulite LPL-125-5 semiconductor diaphragm sensors, .125 inches in diameter with a pressure range of 0 to 25 psia, a frequency response in excess of 20,000 Hz, and a linear response to pressure throughout the range of interest. These transducers were extensively tested to determine their durability and acceleration and strain sensitivity. All transducers were calibrated at the same time in a pressure vessel. Figure 4 illustrates a calibration curve for a typical transducer showing the response of the transducer through the test data reduction system. Even at very low pressure, the transducer accuracy is very good.

Figure 5 provides a cutaway view of the transducer

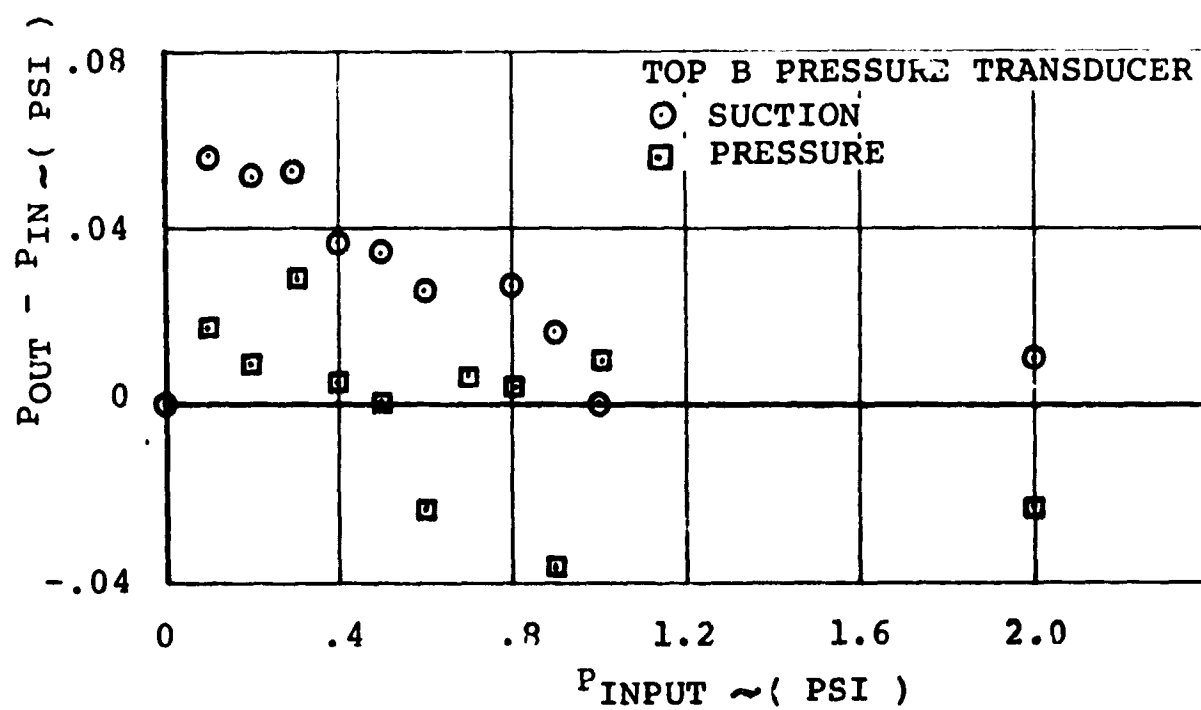


FIGURE 4

END TO END SYSTEM CALIBRATION CHECK
THROUGH DATA ACQUISITION SYSTEM

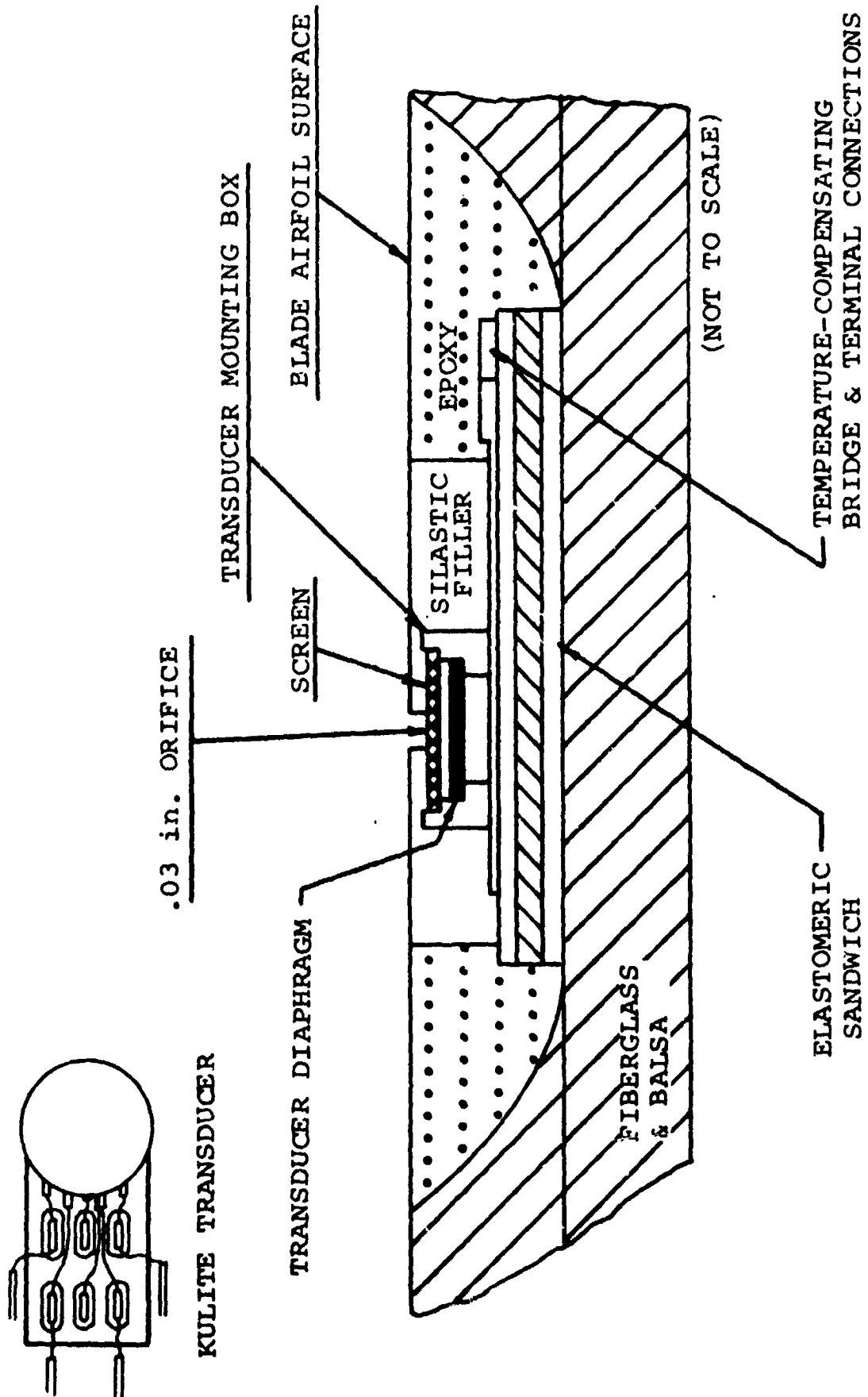


FIGURE 5

PRESSURE TRANSDUCER INSTALLATION
IN THE ROTOR BLADE

installation, and a sketch of a pressure transducer. Table 1 provides a listing of the transducer radial and chordwise positions on the blade and a listing of the data runs for which each transducer was operational.

Initially, strain and acceleration effects were found to be present, so design changes to the transducer mounting and diaphragm were incorporated to minimize these effects.

To alleviate the strain effects on the pressure sensing diaphragm, the transducer, located in a depression on the blade at the 75 percent radial station, was mounted on an elastomeric sandwich. To protect the diaphragm from foreign object damage, a screen was placed over the diaphragm. The area adjacent to the transducer was filled with a silastic rubber compound which covered the protective screen with the exception of a .030 inch diameter hole through which air pressure could be sensed. This small part between the transducer and the airstream was desired so as to obtain a better approximation to a point pressure measurement. To minimize the acceleration effects on the transducer, a design change was made which moved the wire connections of the electronic load bridge on the transducer diaphragm from the center to the edge so their weight would not affect the diaphragm deflection. Wiring from the transducers to the slipring assembly on the rotor shaft was routed internally to maintain a smooth airfoil surface along the span and the depression around the transducer assembly was filled with an epoxy compound to maintain the airfoil contour.

Skin Friction Gages

Boundary layer measurements were taken on one of the blades using the heated-film skin-friction gage technique developed by Dr. W. J. McCroskey of the U. S. Army Air Mobility R&D Laboratory. This technique makes use of dual-filament gages that are photo-etched from thin nickel foil and bonded onto the surface of the blade in a manner similar to strain gages. In this test program, these gages were used to measure the skin friction coefficient and surface flow direction throughout the blade stall regime. This was to aid in understanding the nature of the boundary layer flow, to determine transition and separation, and to help identify the stall boundaries that were encountered.

Heated-film skin-friction gages were mounted on both the

TABLE 1
BLADE INSTRUMENTATION SUMMARY

BLADE INSTRUMENTATION PRESSURE RUNS			r/R	RUNS OPERATIONAL		
				BLADE SERIAL NO.		
PRESSURE TRANSDUCERS	Absolute Pressure			S/N 21	S/N 22	S/N 24
	Top A	x/c = .041	.754			933+035
	Top B	x/c = .058	.750			933+035
	Top C	x/c = .102	.750			933+035
	Top D	x/c = .158	.750			933+035
	Top E	x/c = .206	.750			933+035
	Top F	x/c = .303	.750			933+035
	Top G	x/c = .513	.750			933+035
	Top H	x/c = .617	.750			933+035
	Top I	x/c = .702	.750			933+962
	Top J	x/c = .561	.750			933+962
	Top K	x/c = .970	.750			933+962
	Bottom A	x/c = .033	.754			933+035
	Bottom B	x/c = .054	.750			933+035
	Bottom C	x/c = .104	.750			933+035
	Bottom D	x/c = .165	.750			933+035
	Bottom F	x/c = .303	.750			933+035
	Bottom G	x/c = .483	.750			933+962
	Bottom I	x/c = .701	.750			933+962
	Bottom K	x/c = .955	.750			933+035
		Differential Pressure	.78			933+035
ADDITIONAL INSTRUMENTATION	Skin Friction Mag x/c = .1		.723			Random
	Root Flap Angle		.045			000+035
	Root Torsion		.2			000+035

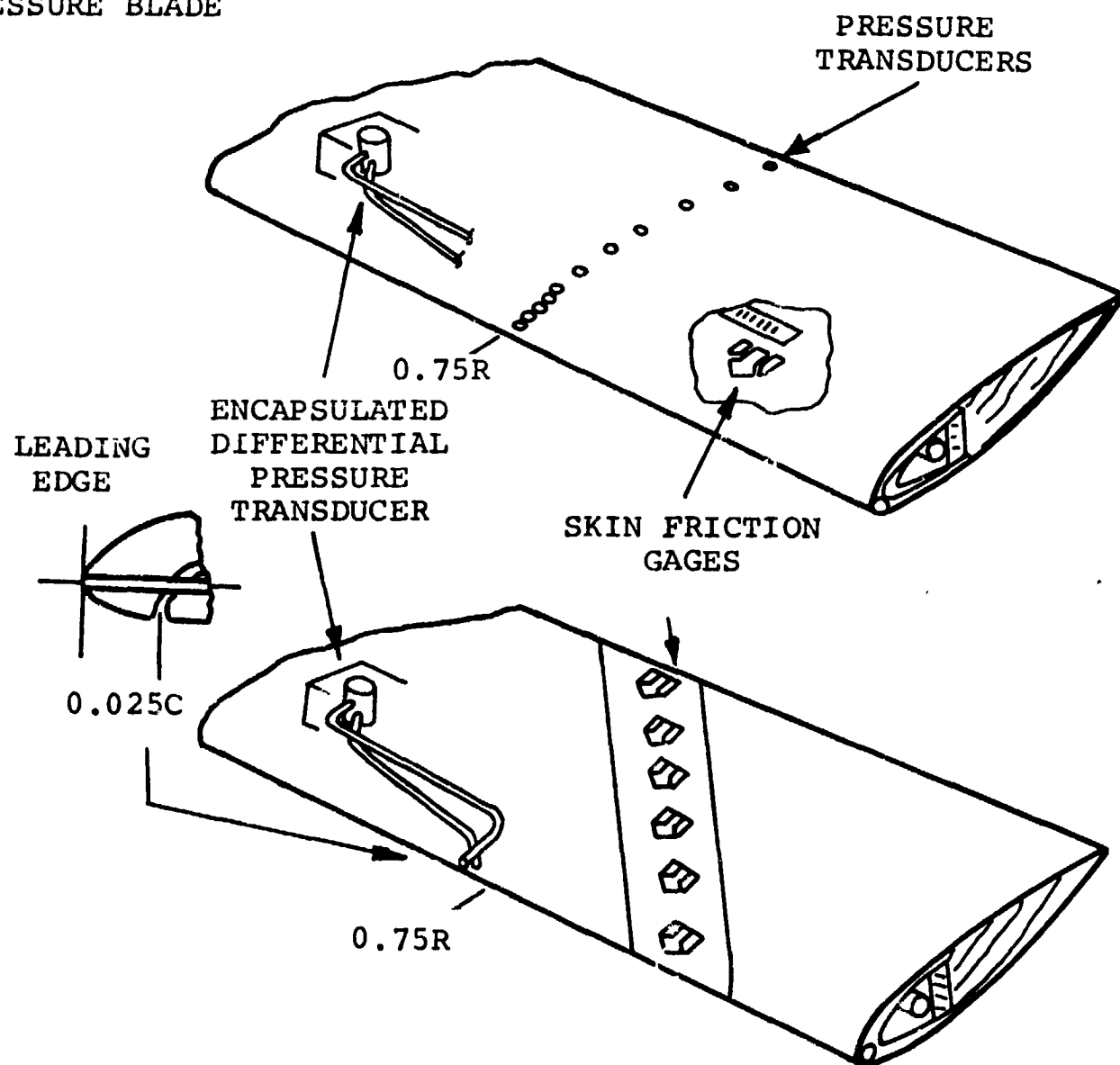
upper and lower surfaces of one blade at approximately the 75 percent radial station (Figure 6). Refer to Table 2 for the measured radial and chordwise locations.

In addition, a V-probe hot wire sensor was mounted approximately 0.1 inches above the upper surface on another blade. A film gage was mounted directly on the blade surface beneath the hot wire sensor. This instrumentation was utilized to help distinguish between fluctuations and dynamic disturbances originating within the boundary layer and those in the inviscid flow. These two sensors would, for example, help to distinguish between an abrupt flow change due to a blade-vortex interaction and the passage of a localized separation bubble lying completely within the boundary layer.

The heated-film skin-friction gages operate on the basic principle that the local skin friction coefficient, C_f , and the local streamline direction at the surface of the blade are proportional to the rates of convective heat transfer from the heated films to the airstream. The technique is analogous to conventional hot wire anemometry, except that special circuitry was utilized to provide the accuracy required. The complete system had sufficient dynamic response to measure and distinguish between periodic signals due to the various harmonics of blade motion and random fluctuations due to turbulence and separation in the boundary layer.

Since the gages were permanently bonded to the surface of the rotor blade, it was not possible to perform individual calibration experiments on the sensors. Therefore, the calibration constants for the magnitude of the skin friction were obtained with the aid of numerical laminar calculations of the boundary layer at low angles of attack in the nonrotating and hover portions of the test program. For these calculations, the flow was assumed to behave in a conventional two-dimensional manner. The calibration constants for the flow angle determination were obtained by assuming that the measurements at low collective pitch in forward flight should follow approximately the theoretical inviscid flow angle in the absence of any local disturbances. A detailed discussion of the skin friction results obtained during this test will be published at a later date.

PRESSURE BLADE



SKIN FRICTION BLADE

FIGURE 6

Rotor Blade Instrumentation

TABLE 2
BLADE INSTRUMENTATION SUMMARY

BLADE INSTRUMENTATION SKIN FRICTION RUNS			r/R	RUNS OPERATIONAL		
				S/N 21	S/N 22	S/N 23
SKIN FRICTION TRANSDUCERS	Top A Mag	x/c = .1	.723			036-055
	Top B Dir	x/c = .2	.729			036-055
	Top B Mag	x/c = .2	.729			036-055
	Top C Mag	x/c = .3	.736			036-055
	Top D Dir	x/c = .5	.750			036-055
	Top D Mag	x/c = .5	.750			036-055
	Top E Mag	x/c = .6	.757			036-055
	Top F Dir	x/c = .85	.774			036-055
	Top F Mag	x/c = .85	.774			036-055
	Bottom A Mag	x/c = .10	.723			036-055
	Bottom C Mag	x/c = .3	.736			036-055
	Bottom E Mag	x/c = .6	.757			036-055
	Bottom F Mag	x/c = .85	.774			036-055
	Bottom F Dir	x/c = .85	.774			036-055
	Elevated Dir	x/c = .50	.75	Random		
	Elevated Mag	x/c = .50	.75	Random		
	Surface Dir	x/c = .50	.74	036-055		
	Surface Mag	x/c = .50	.74	036-055		
ADDITIONAL INSTRUMENTATION	Differential Pressure		.78			036-055
	Root Flap Angle		.045			049-055
	Root Torsion		.2			049-055

Differential Pressure Transducer and Angle of Attack Measurement Technique

Angle of attack measurements were made through a differential pressure transducer located at the leading edge of the airfoil at $r/R = .78$. The differential pressure was measured between an $x/c = 0$ and an $x/c = .020$ chordwise position on the lower surface of the airfoil. The method of determining the angle of attack from the differential pressure, proposed by the U.S. Army Air Mobility R&D Laboratory, was based on two observations.

A unique relationship exists between the pressure distribution, the aerodynamic angle of attack and the local Mach number at a point on an airfoil for two-dimensional, steady, inviscid flow. The flow in the plane of a rotor blade cross-section generally resembles the two-dimensional quasistatic flow past that airfoil section if the blade is unstalled and the spanwise gradients are small. These idealized conditions are more nearly realized in practice near the leading edge of a blade than elsewhere, and at the leading edge, the pressure gradients are large. Therefore, the relationship between the differential static pressure at two neighboring points near the leading edge, the local dynamic pressure in the chordwise direction, and the local aerodynamic angle of attack in the plane of the cross-section of the blade can be expressed in some functional form

$$\Delta C_p = \frac{p_1 - p_2}{\frac{1}{2} \rho V^2 \cos^2 \Lambda} = f(\alpha, \dot{\alpha}, M)$$

or

$$\alpha = f(\Delta C_p, \dot{\alpha}, M)$$

where p_1 and p_2 are the static pressures at points 1 and 2, ρ is the density, V is the magnitude of the local total velocity, Λ is the local sweep angle, α is the angle between the chord line and the normal component of velocity, $\dot{\alpha}$ is the time rate of change of α , and M is the normal component of the local Mach number; that is, M based on $V \cos \Lambda$.

Differential pressure transducers for angle of attack measurement were used on both the pressure blade and the skin friction blade. Calibration of the differential pressure transducer was accomplished during the nonrotating portion of the test program. The airfoil was pitched through a series of angles of attack. During this pitch sweep, the differential

pressure and pressure distribution about the airfoil at .75R were recorded and the blade element angle at this station was measured using an inclinometer mounted on an airfoil template. Due to the inaccuracies involved in locating the leading edge point of angle of attack reference line with the template, a check of this calibration was made.

Such a check could be made by comparing angle of zero normal force points between present test results and standard V23010-1.58 airfoil characteristics. By integrating the measured pressures around the airfoil, a curve of normal force coefficient versus measured blade element angle was made. Figure 10 presents such a curve compared to test results of the same V23010-1.58 airfoil at full scale Reynolds numbers. The difference in the angle of zero normal force, 1.7 degrees, is attributed to the difficulty in obtaining an accurate reference line with the template. Since the full scale data is referenced to the NACA chord line, a correction of 1.7 degrees was made to the measured angle of attack data to adjust it to the standard NACA reference. All angle of attack measurements presented in this report have been corrected to the NACA reference line (Figure 3). The correction to the measured angle of attack is included in the calibration of the differential pressure transducers shown in Figure 11. The data obtained from the differential pressure transducer yielded angles of attack only up to where stall occurred on the airfoil ($\alpha = 14$ degrees). There, a rapid decrease in differential pressure was noted (Figure 11) and the angle of attack obtained from the transducer was invalid until re-attachment of the flow occurred.

Trends observed below stall were used to extrapolate the calibration to higher differential pressures; for when the transducer was flown in forward flight, much higher differential pressures were observed than those obtained statically. These higher differential pressures were expected and can be associated with the dynamic extension of C_n observed on oscillating airfoils.

The effects of sweep, Mach number, and rate of change of angle of attack were neglected for the data analysis of this test. The sweep effect is illustrated in Figure 7 by results obtained on a NACA 0012 in the U.S. Army Air Mobility R&D Laboratory (7 x 10-foot) subsonic wind tunnel. The pressure p_1 was measured at the $x/c = .022$ location on the lower surface, and the pressure p_2 was measured at the leading edge. These

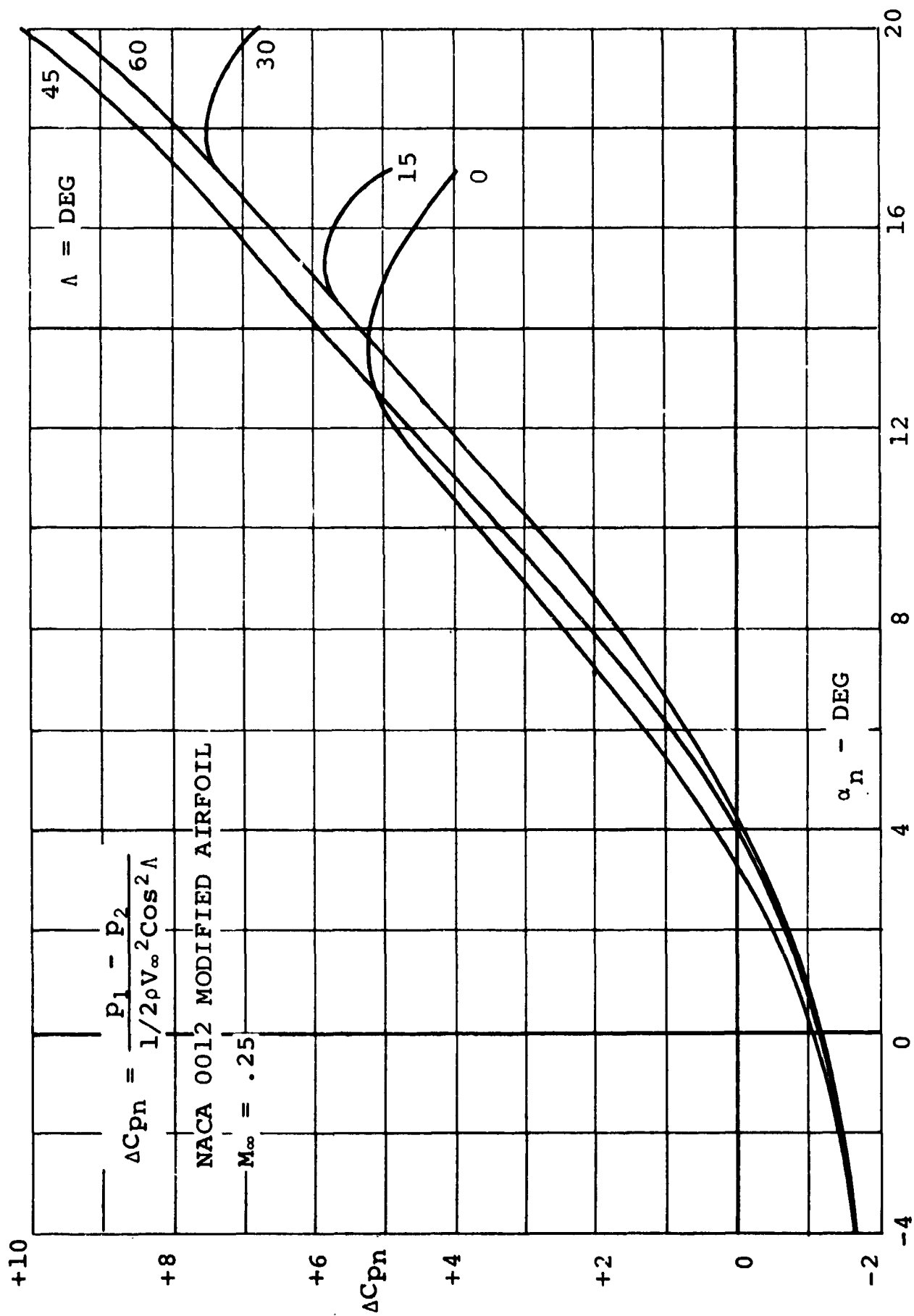


FIGURE 7

EFFECT OF SWEEP ANGLE ON LEADING EDGE
DIFFERENTIAL PRESSURE

results show that ΔC_p is sensitive to angle of attack and is mildly dependent on sweep angle below the onset of stall.

The Mach number effect is illustrated in Figure 8 by results obtained from measurements by Lizak (Reference 5). The results indicate a strong Mach number dependence, but because of the angle of attack and the Mach number environment of a rotor, the effect on α determined by ΔC_p would be small (i.e., when Mach number is large at $\psi = 90$, α is small; when Mach number is small at $\psi = 270$, α is large). Mach number effects were, therefore, neglected. The rate of change of angle of attack ($\dot{\alpha}$) effect is illustrated by Figure 9 from results obtained by Liiva (Reference 1) during an oscillating airfoil test. The effect is similar to what would be expected based on potential flow theory for oscillating airfoils (Reference 6). The effect of $\dot{\alpha}$ on the angle of attack measurements is not well defined. However, the static and hover angles of attack determined by the differential pressure method do agree well with measured angles as shown in Figure 17.

Blade Loads and Motion Gages

Due to the limited number of available data recording channels, only root torsion and root flap angle data for the pressure blade were recorded during the test program. These data, along with the cyclic input and knowledge of the test condition, were used to reconstruct the blade element environment.

Data Acquisition System

The Boeing-Vertol wind tunnel data system is capable of accepting 120 channels of model and tunnel data. It samples and conditions the desired data channels, converts the data to digital form, and then operates on the data with an IBM 1800 data processor. The data are then stored on tape and then transferred to the IBM 360 for further processing. On-line data in final form are available through use of the IBM 1800 data processor. A block diagram of the data flow is given in Figure 12.

The signal conditioners accept data signals from the model and tunnel sensors and provide power adjustment, amplification, zero setting, and filtering for each channel. The conditioned data are then supplied to one of the two multiplexers, depending upon the nature of the data.

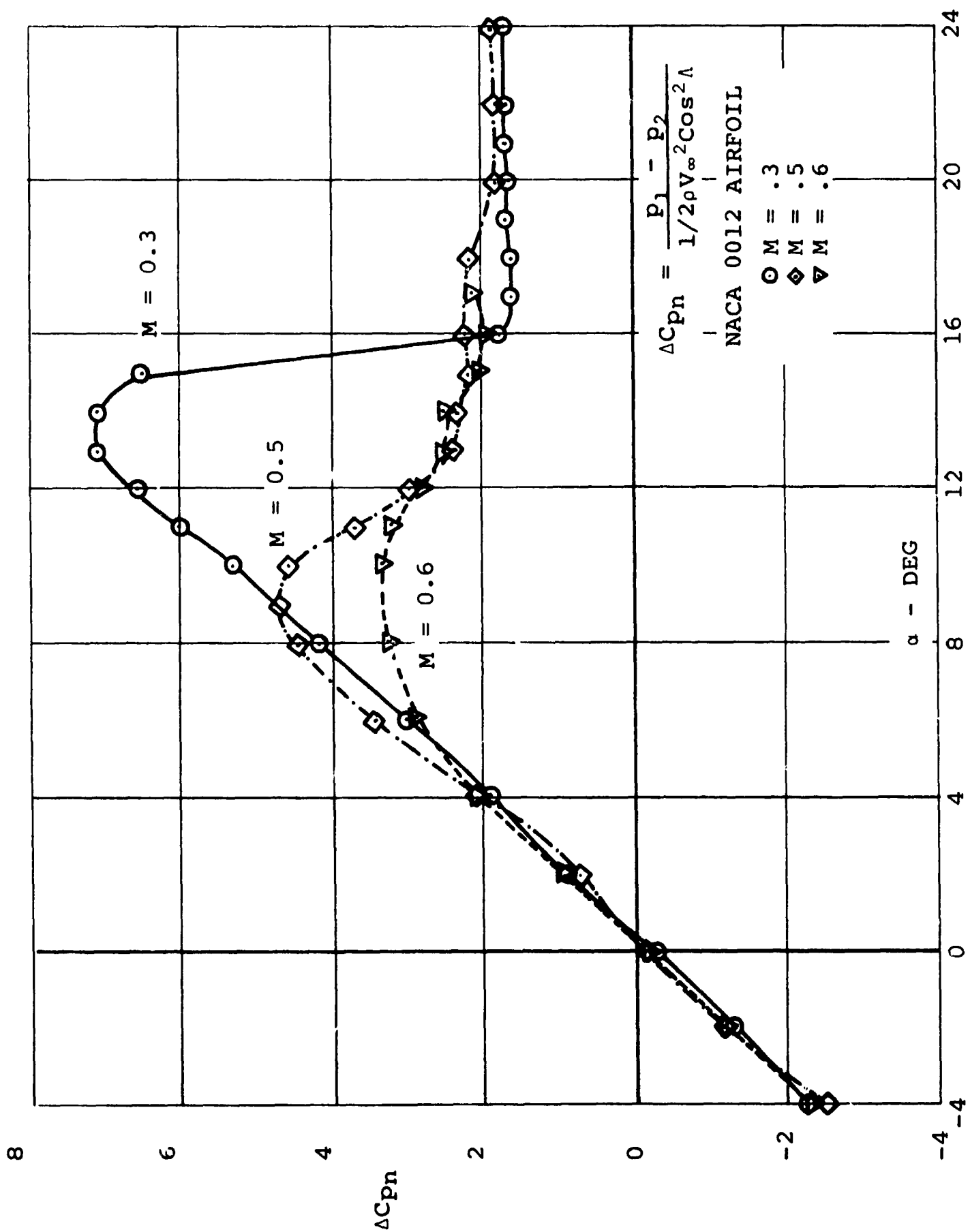


FIGURE 8

EFFECT OF MACH NUMBER ON LEADING
EDGE DIFFERENTIAL PRESSURE

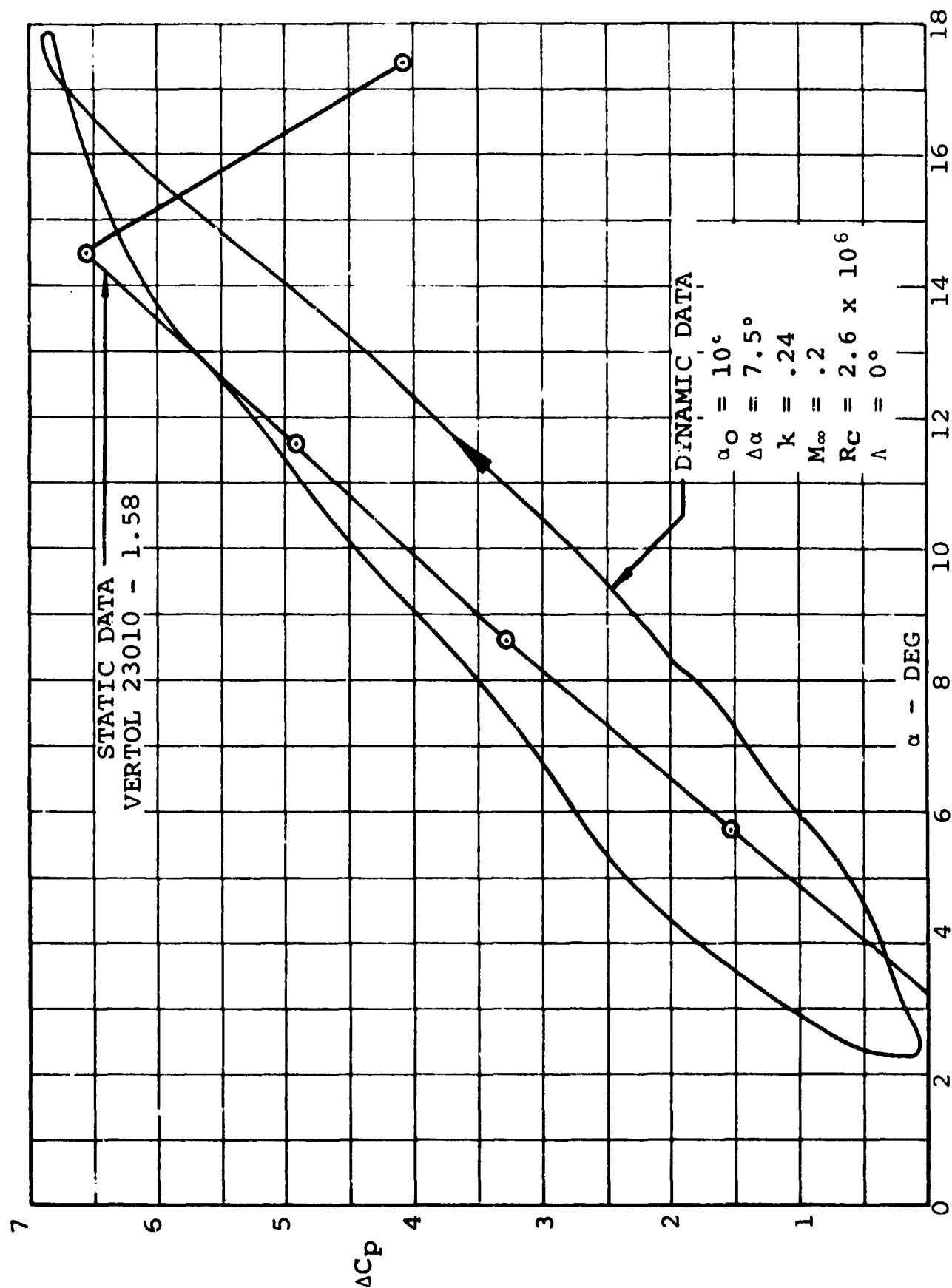


FIGURE 9

EFFECT OF $\dot{\alpha}$ ON LEADING EDGE
DIFFERENTIAL PRESSURE

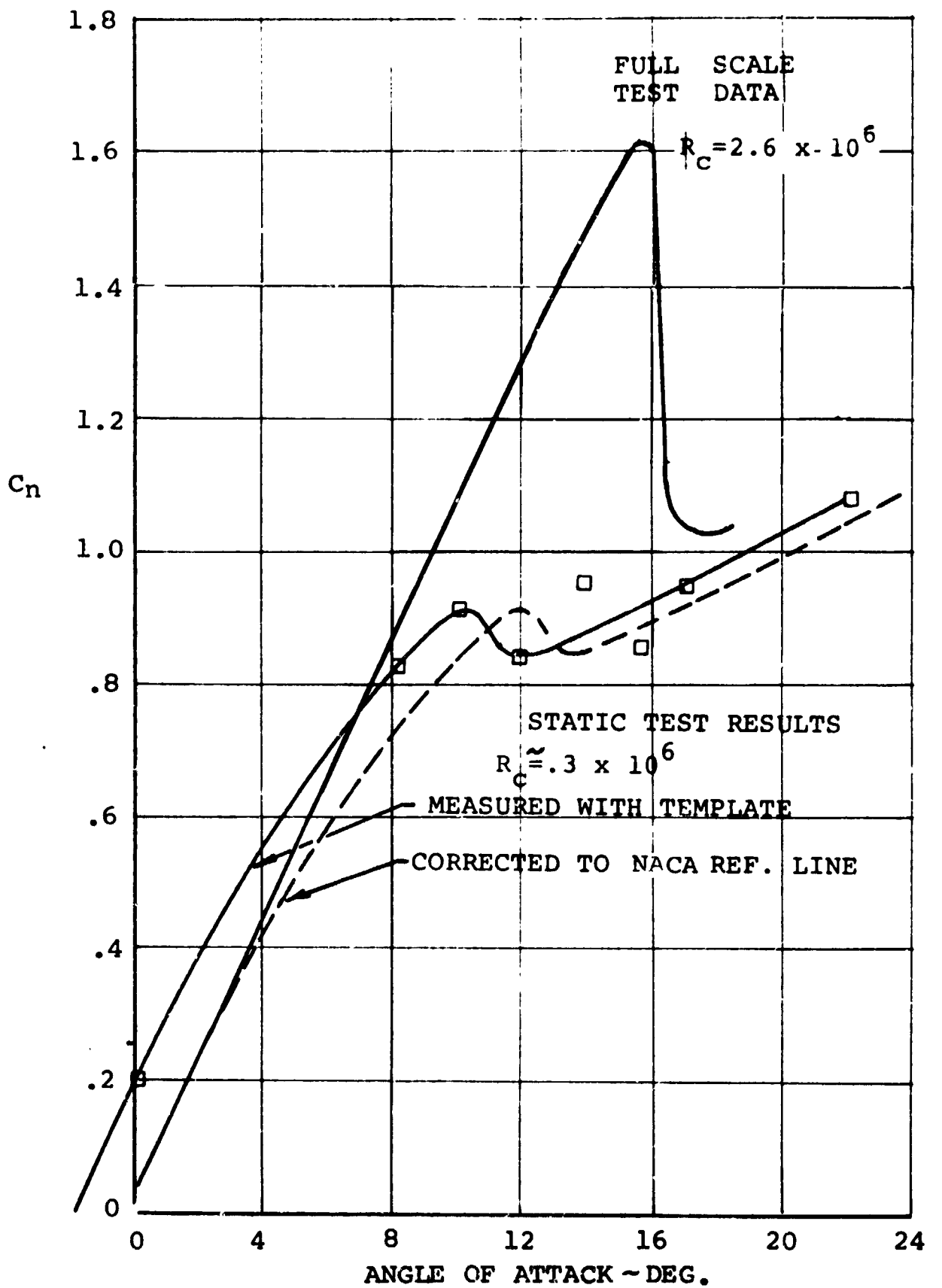


FIGURE 10

COMPARISON OF MODEL SCALE AND FULL SCALE
ANGLE OF ATTACK MEASUREMENTS

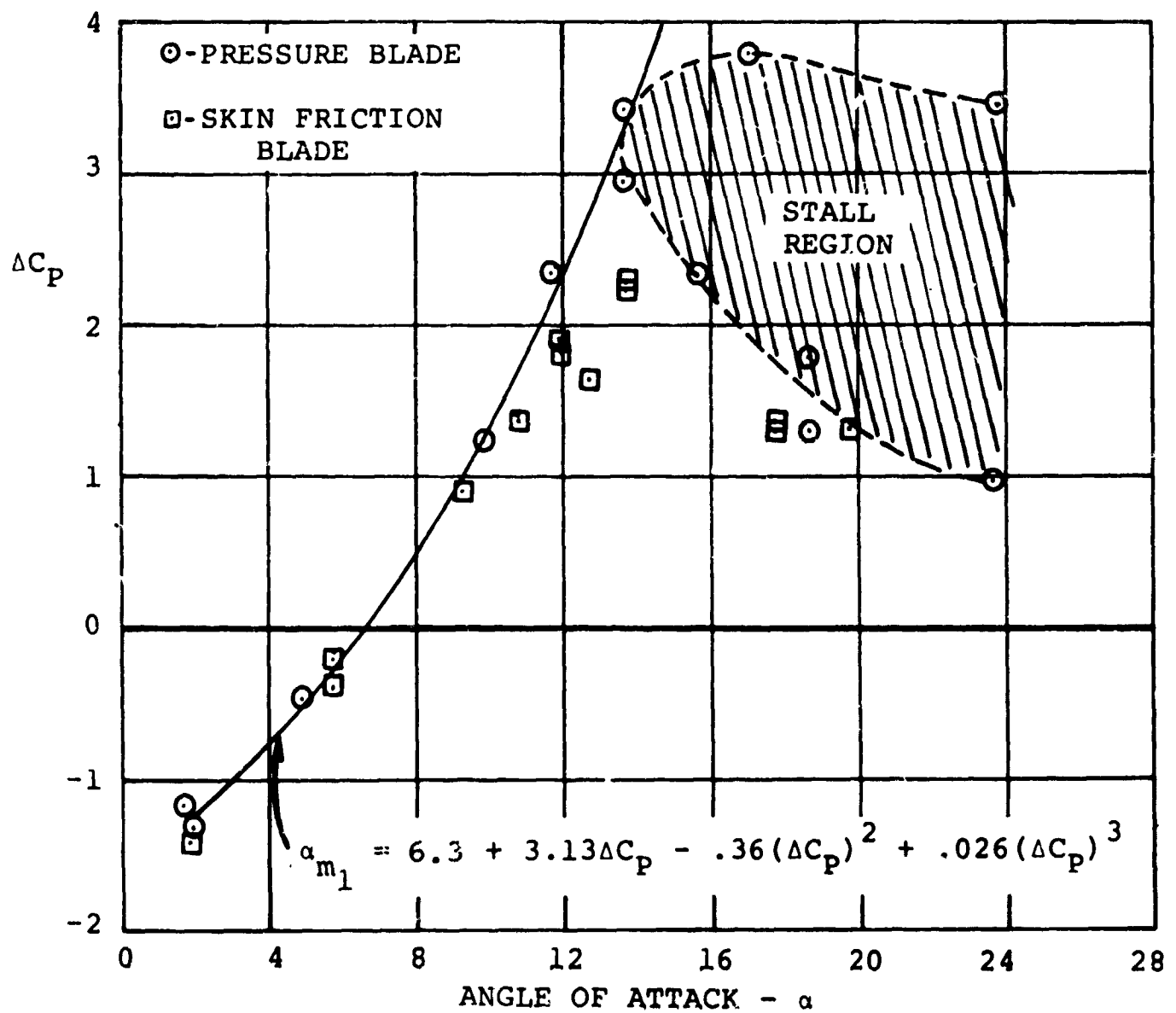
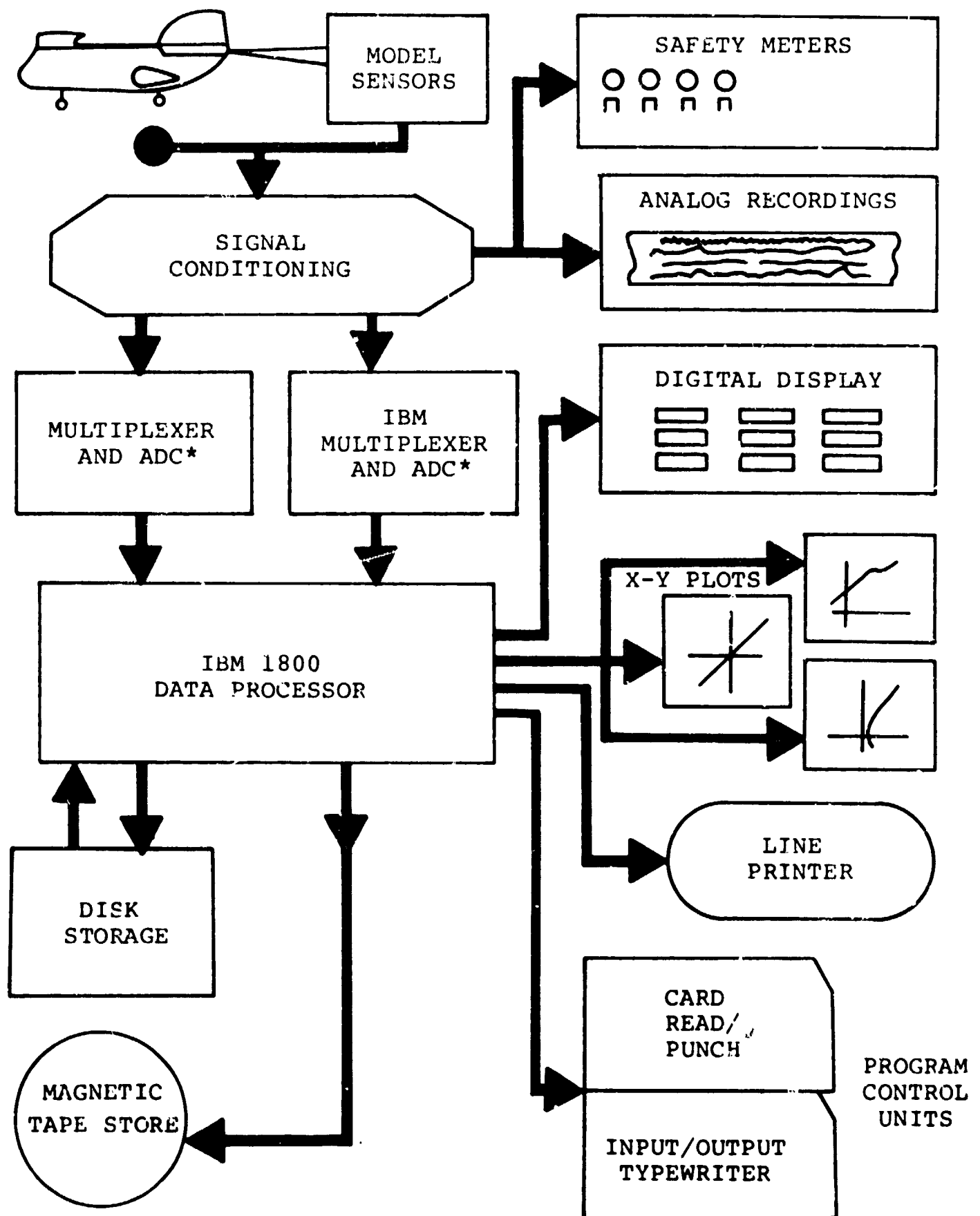


FIGURE 11 CALIBRATION RESULTS OF LEADING EDGE DIFFERENTIAL PRESSURE ANGLE OF ATTACK TRANSDUCER

DATA ACQUISITION SYSTEM



* ANALOG TO DIGITAL CONVERTER

FIGURE 12

The low-speed multiplexer is capable of accepting a maximum of 48 data channels. It is used to sample data at rates from 100 Hz to 10,000 Hz and is intended for use with steady-state data where harmonic content is not of primary concern. The remaining 64 channels are connected to a high-speed multiplexer which is capable of sampling dynamic data on line without loss of its harmonic content. Both multiplexers contain analog-to-digital converts which transform the data to digital form.

The IBM 1800 data processor is a combination of general purpose computer and special input/output features. The activity of the 1800 is under the control of a series of operating programs. These programs will, among other functions, calibrate and check the calibration of the instrumentation, take wind off zeros, monitor and display selected data, and acquire and process the data for final output.

For each data point, a record of approximately two seconds was made. From this record, the data were processed through the system described above and then input into the various manipulative and analytic programs, where the data were converted to engineering units, harmonically analyzed, corrected, and presented in a convenient form (Figure 13).

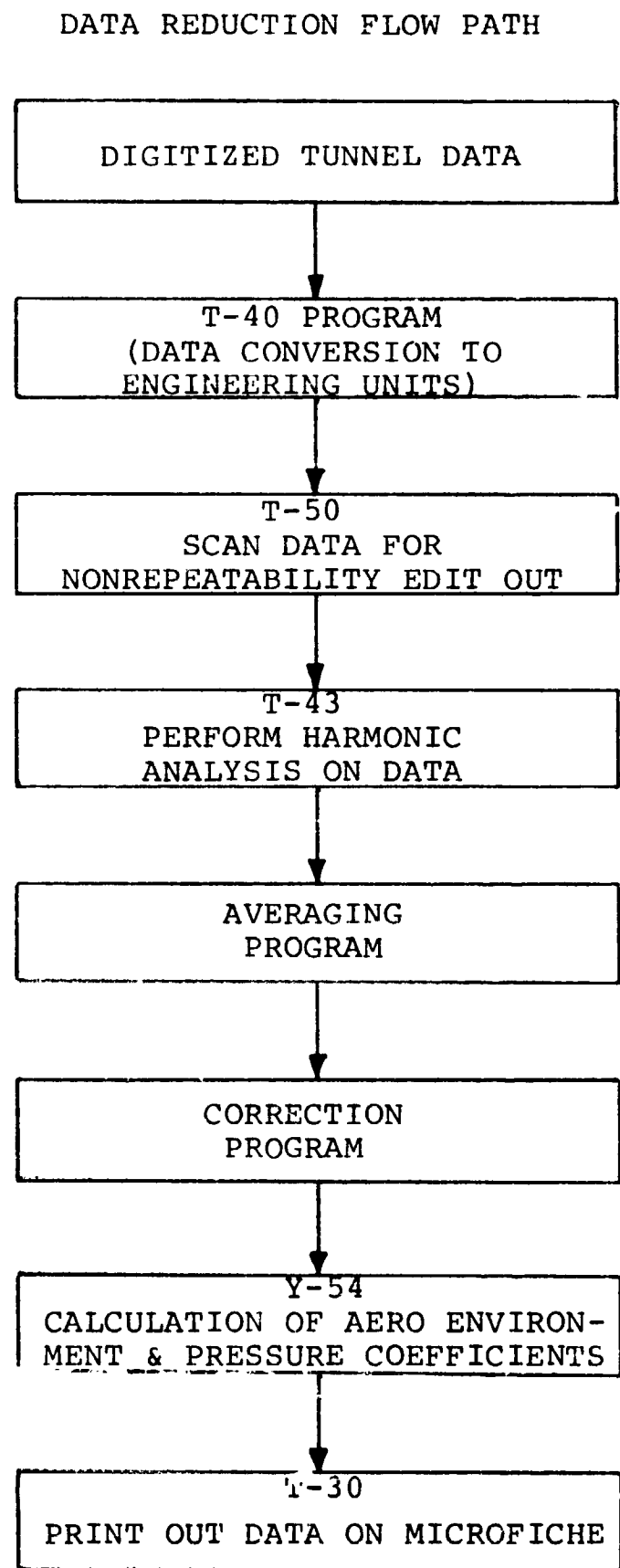


FIGURE 13

TEST PROGRAM

Test Procedure

Data during the test program were acquired during two separate test portions because of the extensive instrumentation used. During the first portion, the rotor was configured to include the pressure instrumented rotor blade along with two non-instrumented blades. Pressure data, as well as limited data on blade loads, blade motion, and skin friction, were obtained. During the second portion of the test program, the pressure blade was replaced by the skin friction blade and the skin friction data were acquired at the same test conditions as the pressure blade. Instrumentation for differential pressure and skin friction at $x/c = .1$ on the upper surface were included on both blades to evaluate the repeatability of the two sets of test runs.

Each of the test portions was further subdivided into three phases: nonrotating testing, hover, and forward flight. The nonrotating phase of the test program, accomplished first, served to calibrate the differential pressure transducers as a function of angle of attack and to determine the static aerodynamic characteristics of the airfoil section. These static characteristics were to be used in theory versus test correlation and for comparisons of pressure distributions at the same angle of attack in the nonrotating and rotating regimes. During this nonrotating testing, the blade was positioned at right angles to the wind and supported at its tip and mid-span by a fixture. Runs in which the nonrotating pressure data were acquired are numbered from 930 to 960.

The hover phase of the test program, conducted initially at a tip speed of 250 feet/second, acquired data through a collective pitch sweep. Increments between each collective setting were approximately two degrees. Later in the test program, when skin friction data were being acquired, a hover run was also conducted at a tip speed of 500 feet/second.

Testing during the forward flight phase consisted of setting a collective pitch and varying the rotor shaft angle. The shaft angle was increased until some blade or test stand limiting condition was reached. Testing was conducted at advance ratios of 0.15, 0.35, and 0.60 at tip speeds of 250, 400 and 500 feet/second. Refer to Table 3 for a listing of test runs and the rotor operating conditions.

TABLE 3
MATRIX OF TEST RUNS

	V _T	TEST *	CUFF	RUN NO		TYPE OF RUN
$\mu = 0$	250	Pr	Off	2, 26		Hover Runs
		Pr	On	3, 27		
		SF		50		Collective Pitch Sweep
	500	SF		55		
$\mu = .15$	250	Pr	Off	16, 18		Forward Flt Shaft Angle Sweep
		Pr	On	17, 19		
$\mu = .35$	250	Pr	Off	12, 22, 24		Forward Flight
		Pr	On	13, 23, 25		
		SF		51		Shaft Angle Sweep
	500	Pr	Off	28, 29, 30		
		Pr	On			
		SF		54		
$\mu = .60$	250	Pr	Off	14, 20		Forward Flight
		Pr	On	15, 21		
		SF		52		Shaft Angle Sweep
	400	Pr	Off	31, 33		
		Pr	On	32, 34		
		SF		53		
$\mu = .8$	0	Pr	Off	933→960		Nonrotating Angle of Attack Sweep
		Pr	On	933→960		
		SF		36→48		

* Pr = Pressure Measurement Portion of the Test
SF = Skin Friction Measurement Portion of the Test

It is well to note that prior to acquiring data at each test run, a tunnel "blowdown" was conducted. The blowdown allowed sufficient time for the temperatures throughout the model and tunnel to stabilize. This technique is standard tunnel operating procedure and is done to prevent any instrumentation zero shift difficulties.

Instrumentation problems

Early in the testing of the pressure blade, it became apparent that the extensive efforts made prior to the test to eliminate strain effects on the pressure transducers had not been completely successful. Strain effects, though not large, were significant during the nonrotating testing because of the low pressures being experienced by the transducers. A technique was then developed through which the strain effects could be eliminated. For each run that was made with the pressure blade, a corresponding run was made in which the dynamic pressures were kept from the transducers by a cuff which was wrapped around the blade. The cuff was hollow so that all the transducers could experience a common pressure. The cuff was vented at the trailing edge so that flexing of the cuff due to the change in airloads experienced around the azimuth would not affect the pressure inside the cuff. These "cuff-on" data, then, were data including the strain effects, the acceleration effects, and any pressure existing in the cuff. The pressure in the cuff would not affect the integrated pressures, though, for the pressure would be the same for all transducers. The cuff-on data, obtained at identical conditions to the cuff-off data, could then be subtracted from the cuff-off data to account for the effects of strain and acceleration.

An additional problem arose because of the "cuff correction" technique. As mentioned previously, a blowdown of the tunnel was conducted to stabilize all temperatures and minimize any instrumentation problems associated with a temperature change. When the cuff was placed over the transducer, it kept the air from moving across the blade and a change in temperature occurred at the transducer due to the resistance heating in the transducer load bridge. This caused a steady shift to occur in the pressures measured and the steady shift was different for each transducer. Because this would affect the pressure distribution, it had to be removed. This shift in the steady pressure values was isolated by observing the transducer steady readings prior to starting a given run, and then immediately following the startup. The steady readings

recorded by the transducers could then be attributed to blade strain effects, as the short time between startup and the first data point precluded much zero shift due to temperature. This was done for each "cuff on" run, and the results were averaged to produce a set of probable steady pressure readings associated with rotation. These steady pressures along with a correction for the static pressure in the tunnel then replaced the measured "cuff on" steady pressures which included the large temperature induced zero shift.

A far more serious problem arose when the pressure blade was rotated for the first time. As the tip speed passed 300 ft./sec. during an rpm sweep in hover, transducers on the aft portion of the airfoil began to fail. In all, six transducers were lost ($x/c = .70, .86, .97$ on top; $.48, .70, .96$ on bottom). Detailed examination of the blade and the transducers indicated that the failure occurred in the wiring internal to the blade. No repairs were attempted due to the time required and the test was continued. No additional pressure instrumentation was lost during the remainder of the program.

Data Reduction

The digitized data that were acquired on line and stored on tape were input to the data reduction path shown in Figure 13 after the test was complete. The data was converted to engineering units, scrutinized for bad data samples, harmonically analyzed (24 harmonics), and averaged over a number of rotor cycles. The pressure data were then corrected and processed through the Y-54 data computation package (Appendix). Modified "cuff on" corrections, described in the previous section, were applied to all hover and forward flight pressure runs except those at high tip speed (500 ft./sec., $\mu = .35$); at high tip speeds, the cuff could not be kept on the blade. Because the trade off of bending moment and centrifugal effects tend to keep the strain effects constant with increasing tip speed, and the measured pressures increase approximately as the square of tip speed, strain corrections at these higher tip speeds do not significantly impact final results.

The Y-54 data reduction program (see the Appendix for a detailed discussion of its calculations) reconstituted the pressure harmonics for each transducer, integrated the results, calculated the characteristics of the blade element environment, and plotted the results.

The skin friction data were provided to the U. S. Army Air Mobility R&D Laboratory in harmonic form for further data reduction.

Data Analysis

A total of six absolute pressure transducers, three on the upper airfoil surface at $x/c = 0.70, 0.86,$ and 0.97 , and three on the lower airfoil surface at $x/c = 0.48, 0.70,$ and 0.96 , failed early in the test program. In order to obtain aerodynamic coefficients based on the integration of the pressure data around the total blade element surface, an engineering approximation was applied to those portions of the airfoil where pressure data were lacking. After viewing many pressure distributions from previous test programs and assessing a theoretical prediction of the pressure distribution, it was decided to approximate the pressure distribution over the aft of the airfoil with a parabola. This parabolic distribution was applied to both the aft upper and aft lower surfaces in the following manner: The parabola passed through the most aft measured pressure data point and had an infinite slope ($dC_p/dx/c = \infty$) at $x/c = 1.0$ where C_p was defined as zero. The equations for these curves are as follows:

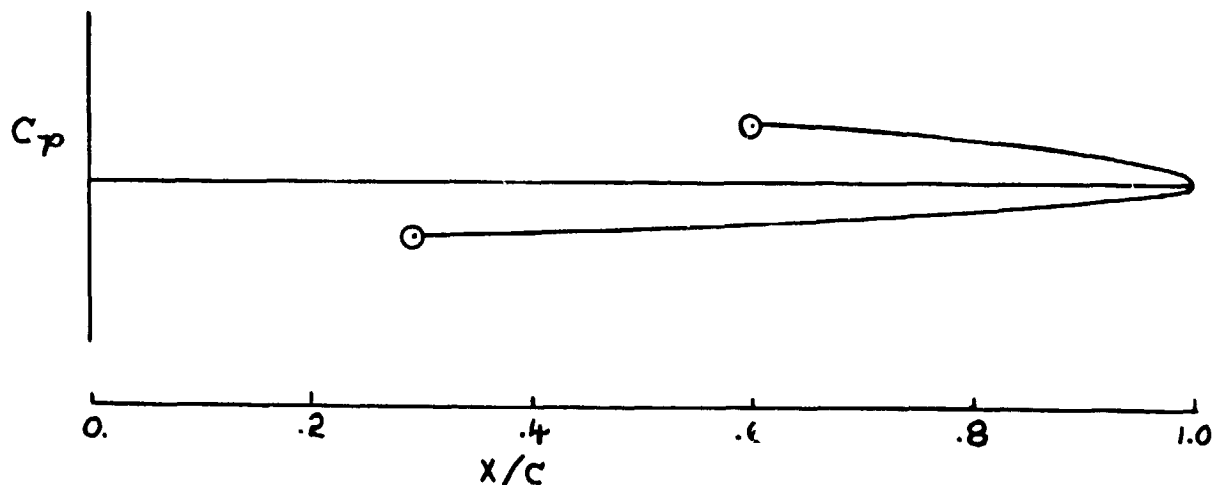
For the upper surface,

$$C_{p(x/c > .617)} = C_{p(.617)} \sqrt{\frac{1 - x/c}{.383}}$$

For the lower surface,

$$C_{p(x/c > .303)} = C_{p(.303)} \sqrt{\frac{1 - x/c}{.697}}$$

The sketch below illustrates the shape of these curves. An evaluation of this approximation is presented during the discussion of the nonrotating data.



Pressure data were reconstituted at 10-degree increments of azimuth from the harmonic data. Blade element aerodynamic coefficients (C_n , C_c , C_m) were then computed. The computations were made two different ways. The first involved integration of only actual measured test data on the forward portions of the blade element; i.e., zero pressure was assumed aft of $x/c = .617$ on the upper surface and aft of $x/c = .303$ on the lower surface. The second utilized the engineering approximation described above to account for the absence of test data on the aft portions of the airfoil. The trapezoidal technique was employed for the integration of the measured test data. For all aerodynamic coefficients presented and discussed in the body of this report, the approximation has been used. A complete listing, in microfiche form, of the blade element aerodynamic coefficients per ten degrees of azimuth position, for each run and test point (with and without the approximation applied), can be obtained by contacting Dr. W. J. McCroskey of the U. S. Army Air Mobility R&D Laboratory at Moffett Field, California.

Calculations based on classical rotor theory, Reference 7, using the measured blade flapping were made to determine the blade velocity environment and the local dynamic pressure (q_{Loc}). This quantity was then used to nondimensionalize the measured pressures and the integrated blade forces and moments and produce the aerodynamic coefficients.

Blade root torsional load data were utilized to construct the blade elastic twist at the 75-percent radial station. Because blade elastic twist occurs predominantly in the first elastic torsional mode, knowledge of the torsional load at the root is sufficient to approximate the blade elastic motion at the 75-percent radius. This motion, along with a knowledge of the rotor cyclic and collective pitch, was used to calculate the blade total feathering motion.

A theoretical angle of attack as a function of azimuth was computed from the expression

$$\alpha_c = \theta + \tan^{-1} \left(\frac{u_p}{u_r} \right)$$

using the blade feathering motion and the blade element calculated velocity environment.

A second measure of the angle of attack was made based on knowledge of the blade element static airfoil characteristics and the dynamic C_n . It was calculated as

$$\alpha_{m_2} = \frac{C_{n \text{ DYNAMIC}} - C_{n(\alpha=0) \text{ STATIC}}}{(dC_n/d\alpha)_{\text{STATIC}}}$$

An angle of attack was also calculated based on the differential pressure measured at the leading edge of the airfoil (see Instrumentation section for background discussion). This angle of attack, designated α_{m_1} , was then corrected for the velocity at the leading edge of the airfoil due to blade feathering motion. When this correction is applied, the angle of attack is designated as α_{m_1c} .

Other blade element environment quantities were also calculated. A complete listing of these quantities, as well as the details of their calculations, is enclosed in the Appendix.

TEST RESULTS AND DISCUSSION

Nonrotating (Static) Testing

Airfoil characteristics up to an angle of attack of 22 degrees were obtained during static testing of the blade instrumented with the absolute pressure transducers. The testing was performed at a Reynolds number based on chord of $.36 \times 10^6$ and a Mach number of .17. The angle of attack was referenced to the NASA reference line.

The curves of Figure 14 provide a comparison of static airfoil characteristics for the present test results at a Reynolds number of $.36 \times 10^6$ and two dimensional airfoil test data at a similar Reynolds number of $.3 \times 10^6$ and a full scale Reynolds number of 2.6×10^6 . The comparison of the two normal force coefficient curves at nearly equal Reynolds numbers indicate that a stall type different from that expected of the V23010-1.58 airfoil was evident in the pressure blade data. The installation of pressure measuring instrumentation at the three-quarter radius could have changed the airfoil contour, resulting in a change in measured stall characteristics. The gradual change in lift curve slope and the reduction in maximum C_n indicate that the pressure blade was stalling from the trailing edge. Leading edge stall is characteristic of static V23010-1.58 airfoil data. From the integrated pressure data, lift stall is indicated at $\alpha = 12$ degrees and a maximum C_n of 1.0 is achieved. At an angle of attack of 14 degrees, characteristics of moment stall begin to appear. This difference in the angles for lift stall and moment stall again point out the possibility of a difference in airfoil contour, for the two-dimensional test data indicates that these stall angles nearly coincide for the V23010-1.58 airfoil.

Pressure distributions accompanying the integrated data look two-dimensional below stall (Figure 15). However, once stall occurs, as evidenced by no further increase in C_n with α , the pressure distributions differ from those one might expect knowing the characteristics of the airfoil at full-scale Reynolds number (Figure 16). There is a rise in suction on the aft portion of the airfoil, but the collapse of the suction peak near the leading edge of the upper surface of the airfoil never clearly occurs. Both the pressure distribution and the integrated results suggest that stall is occurring from the trailing edge at this low Reynolds number. This is contrary to previous experience with the V23010-1.58 airfoil

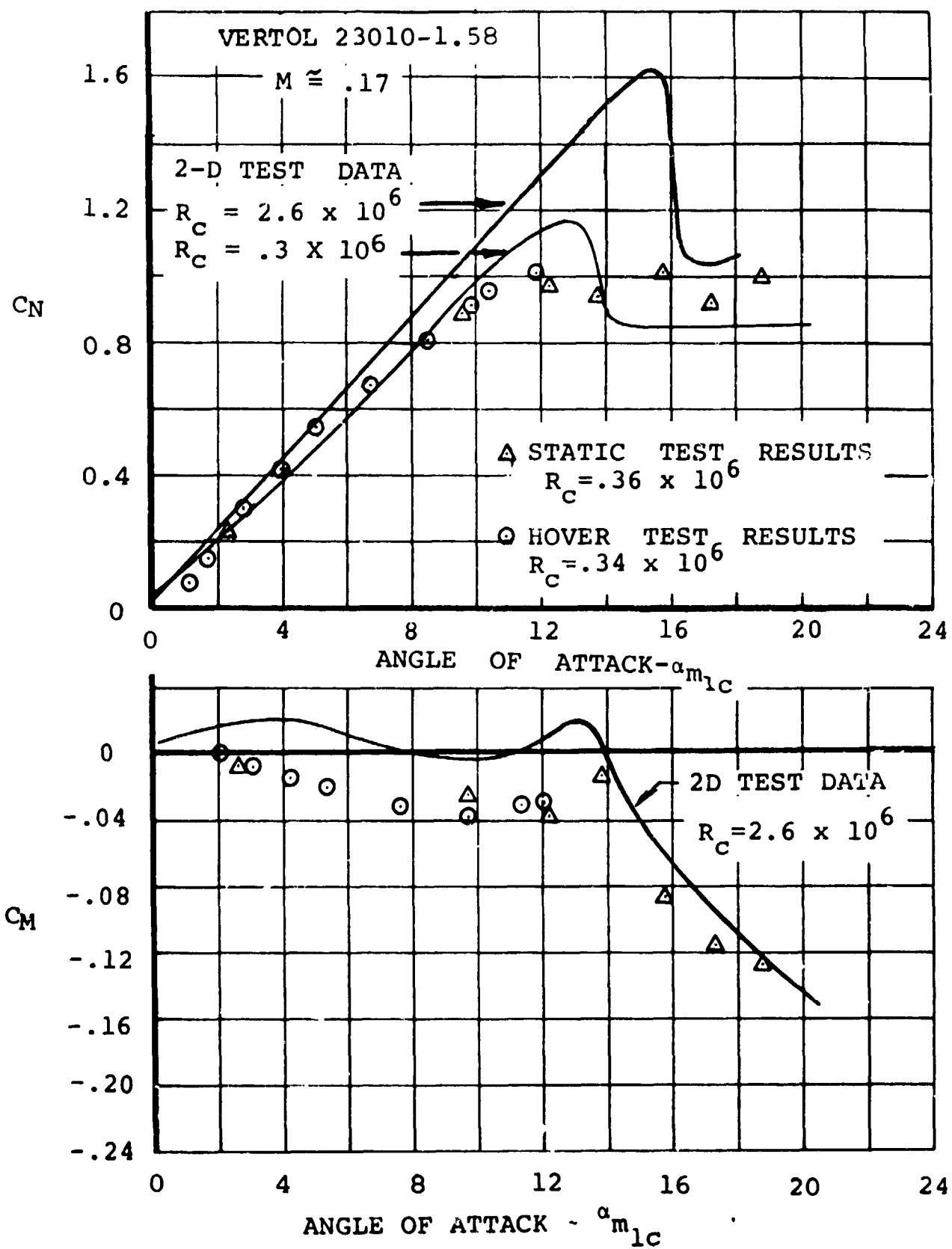
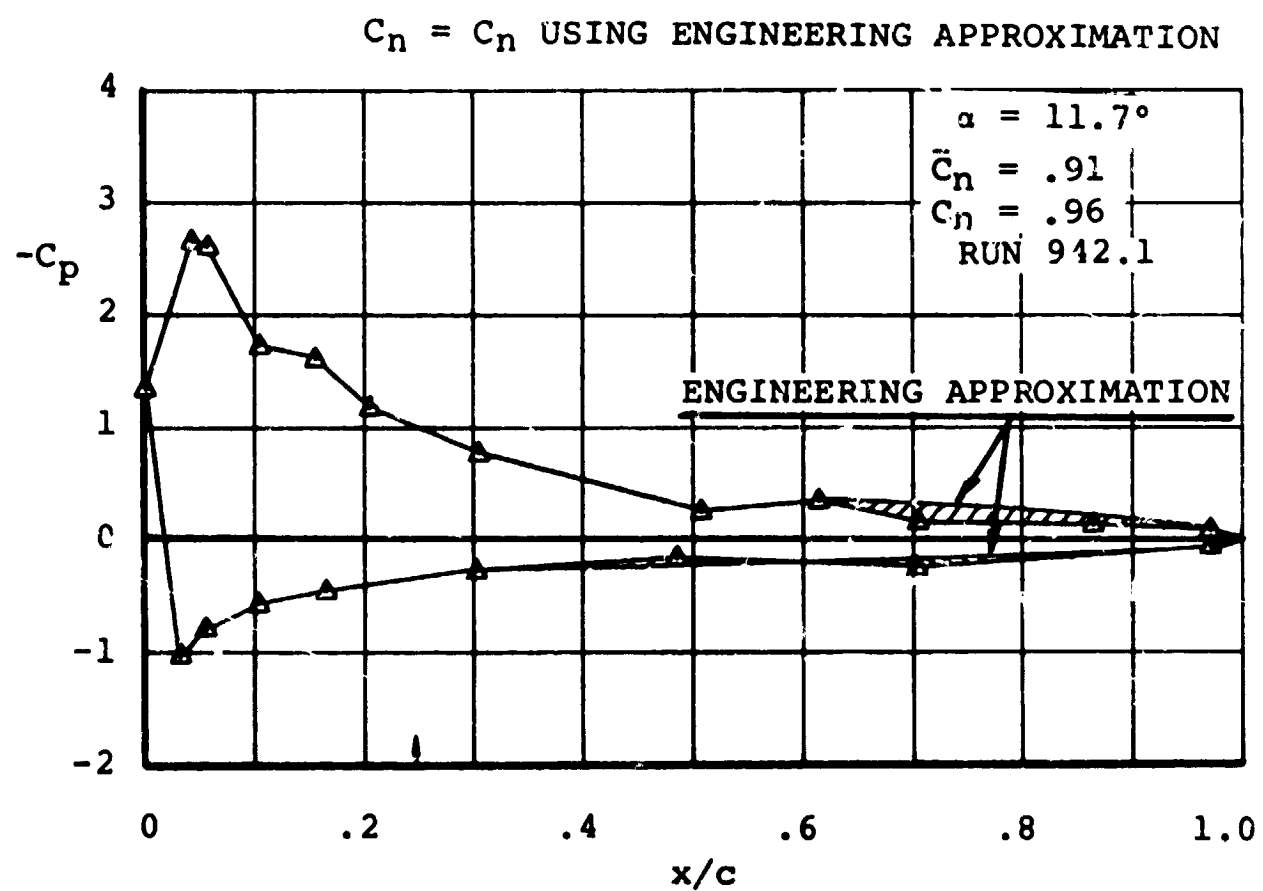
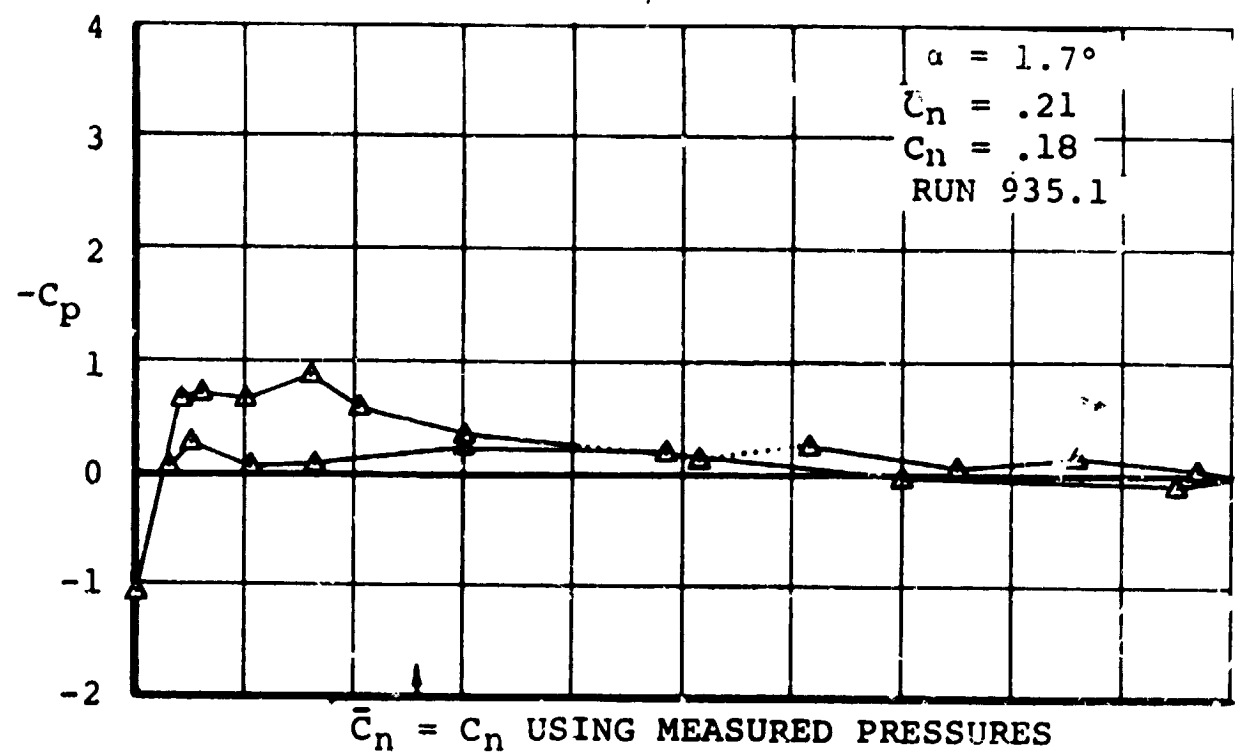


FIGURE 14

COMPARISON OF FULL-SCALE AND MODEL
SECTION AIRLOAD CHARACTERISTICS

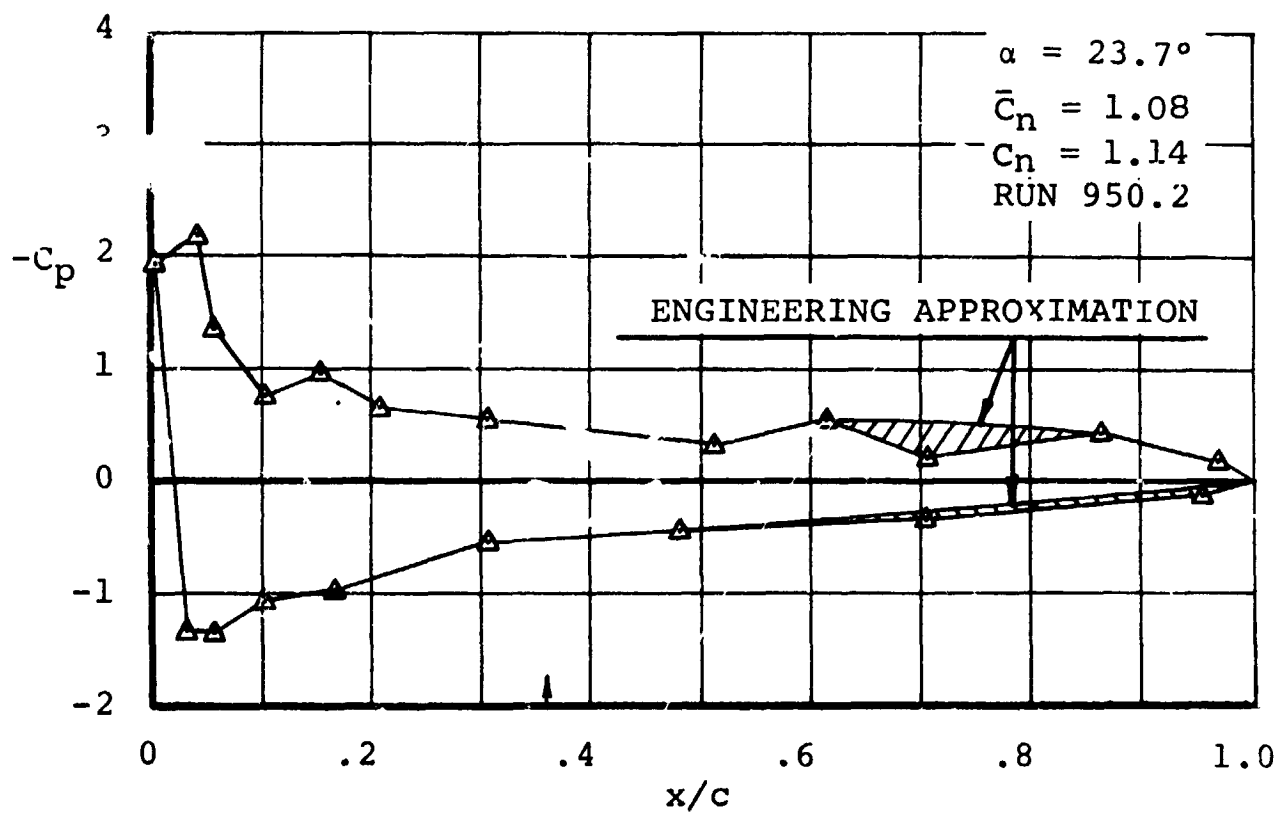
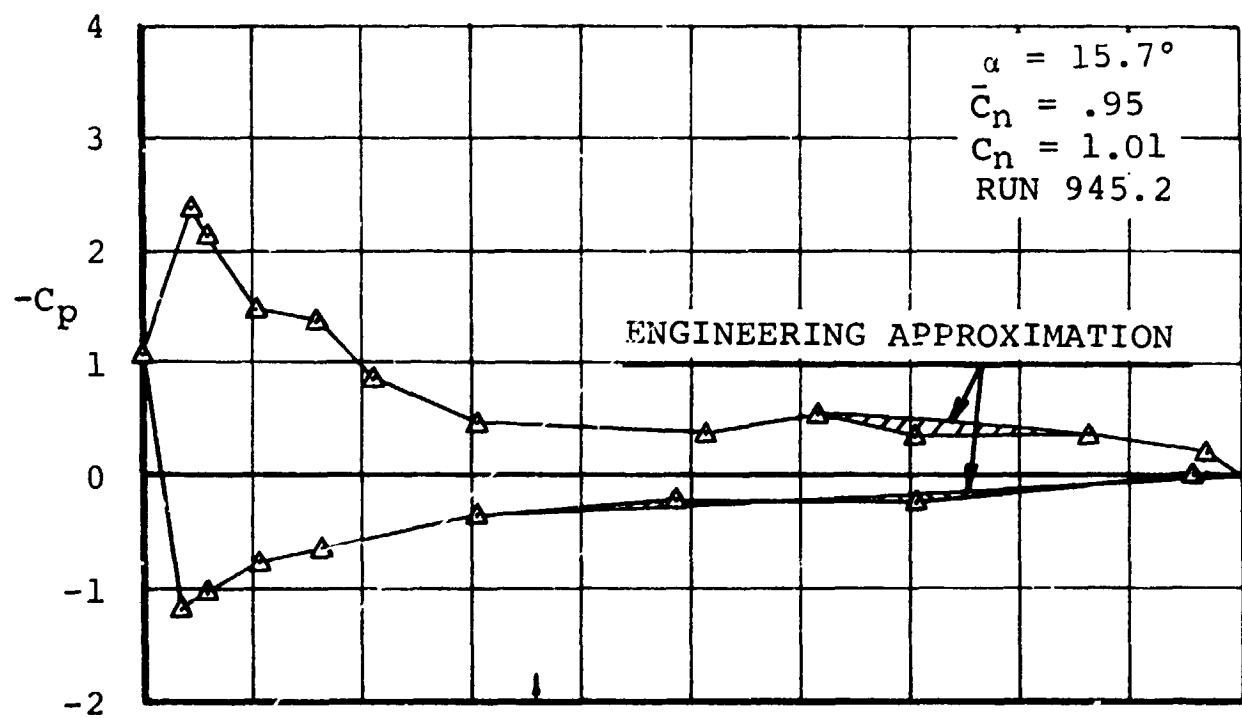


↑-INDICATES CENTER OF PRESSURE

$$R_c = .36 \times 10^6, M = .27$$

FIGURE 15

STATICALLY OBTAINED PRESSURE DISTRIBUTIONS



$$R_c = .36 \times 10^6, M = .17$$

FIGURE 16 STATICALLY OBTAINED PRESSURE DISTRIBUTIONS

which indicates leading edge stall even at this low Reynolds number and again suggests the possibility of a change in airfoil contour on the blades. The significance of this change cannot be evaluated from available data.

Because the nonrotating data were the only data obtained during this test where all transducers were operational, it was utilized to check the accuracy of the engineering approximation for the missing data. Analysis of the nonrotating data was made with the approximation replacing pressures on the aft portion of the airfoil where the transducers had failed during the rotating tests. Figures 15 and 16 illustrate a comparison of pressure distributions with and without the engineering approximation that was discussed in the Data Analysis section. Figure 17 illustrates the effect of the approximation on the blade element force and moment coefficients throughout the measured angle of attack range. The use of the approximation causes C_n to be underpredicted below angles of attack of 5 degrees. Above 5 degrees, the C_n is overpredicted. At an angle of attack of 10 degrees, C_n is overpredicted by .04 and at higher angles, C_n is overpredicted by .06. The blade element pitching moment coefficient, C_m , is slightly overpredicted at angles of attack below 5 degrees and is underpredicted (more negative) by approximately .025 at higher angles of attack.

While the engineering approximation causes a shifting of the values of these coefficients, the trends based on the approximation essentially parallel those established by the measured data. The similarity of trends provides a great deal of confidence in the use of the approximation. All such coefficients computed in the hover and forward flight regimes and used for discussion in this report make use of this approximation.

Hover Testing

Hover testing was conducted during the test program to determine whether the rotating environment affected the pressure distributions and boundary layer flow characteristics that were observed during the nonrotating phase of the test program. The testing was initially conducted at a tip speed of 250 ft/sec where the 75-percent radius blade element velocity environment was the same as in the nonrotating test. A collective

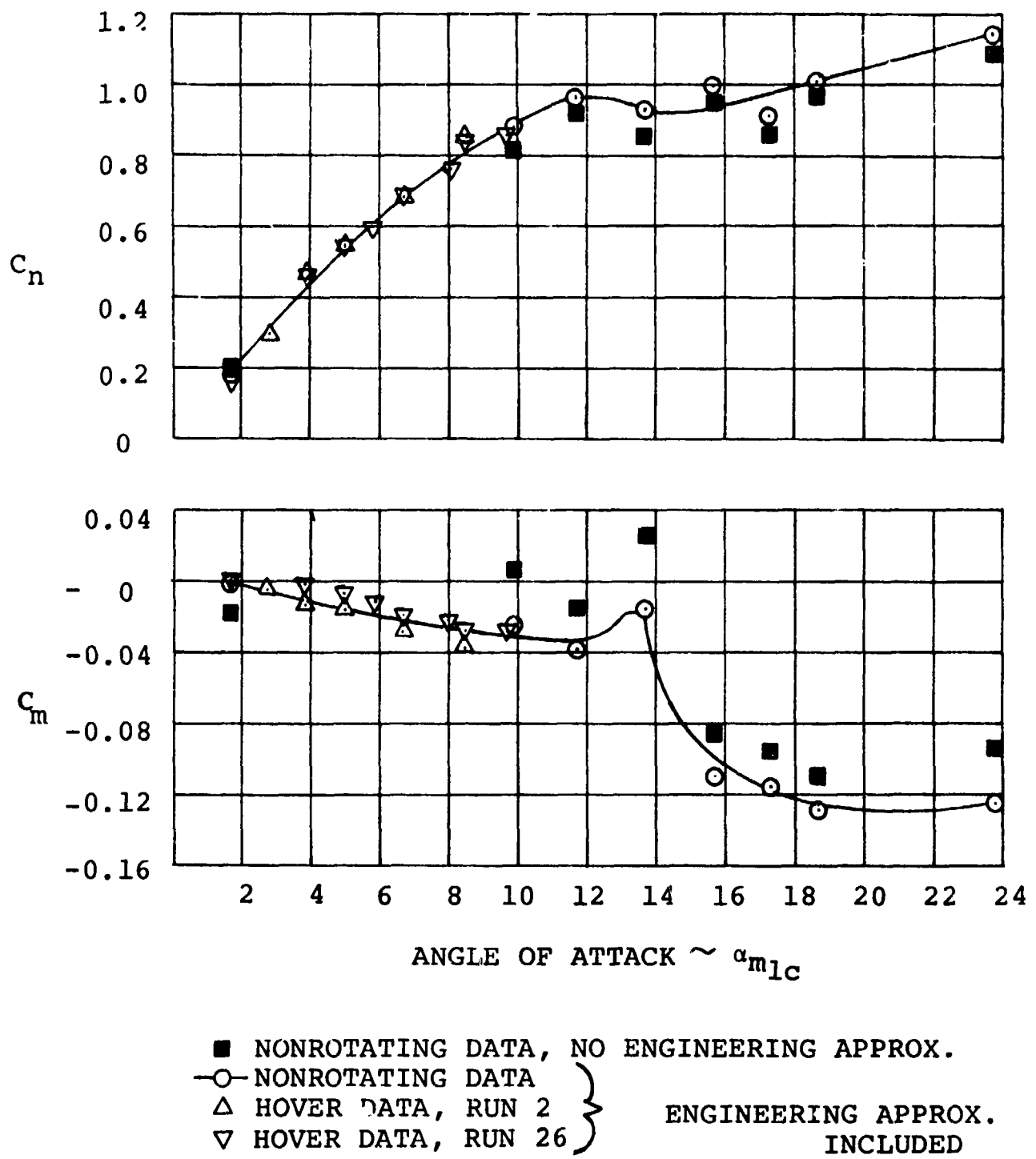


FIGURE 17 EFFECT OF ENGINEERING APPROXIMATIONS ON
BLADE ELEMENT AERODYNAMIC COEFFICIENTS

pitch sweep was conducted from $\theta_{.75} = 0$ to $\theta_{.75} = 26$ degrees in increments of two degrees. Figure 18 illustrates some typical hover performance results.

Two independent sets of hover runs were made at identical conditions on separate days to ascertain data repeatability. Not only did the data from the two hover runs agree (Figure 17), but it also exhibited excellent correlation with the integrated nonrotating pressure data. This correlation also verified that the angle of attack measurement technique was working, for the correlation was obtained only through comparing the pressure distribution at the same indicated angle of attack.

Figures 19 and 20 illustrate the correlation of the rotating and static pressure distributions. Only at the leading edge on the upper surface can any difference between the rotating and nonrotating data be seen.

Figure 17 illustrates the integrated pressure/aerodynamic force coefficient data correlation between the hover and nonrotating runs. The data correlation is good, and the large number of angle of attack points obtained during the hover run provide a very dense calibration of the airfoil characteristics.

Forward Flight

In the forward flight regime, data were obtained at advance ratios of .15, .35, and .60. This was done initially at a tip speed of 250 feet/second because of an early experience with pressure transducer failure at the higher tip speeds. As the test progressed, however, and no further failures were encountered, the tip speeds were increased and data were obtained at a tip speed of 400 feet/second at the advance ratio of .6, and 500 feet/second at the advance ratio of .35. Data runs were made with shaft angle sweeps at a constant collective pitch up into the rotor stall regime.

Rotor Performance

Rotor performance data, although presenting a doubly integrated picture of the rotor environment,

$$\text{Performance} = \int_0^{2\pi} \int_0^R f(x, \psi) dx d\psi$$

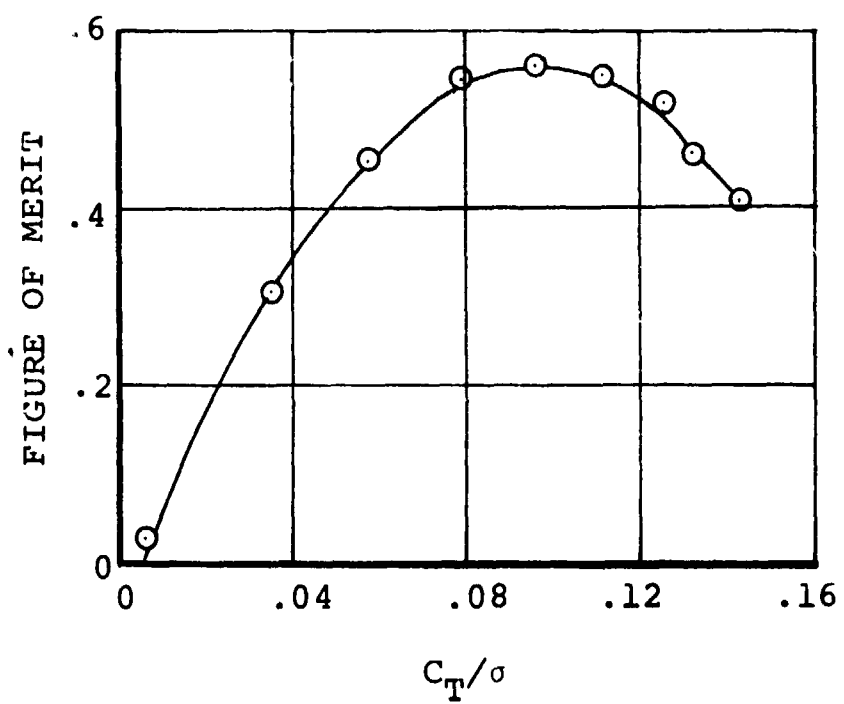
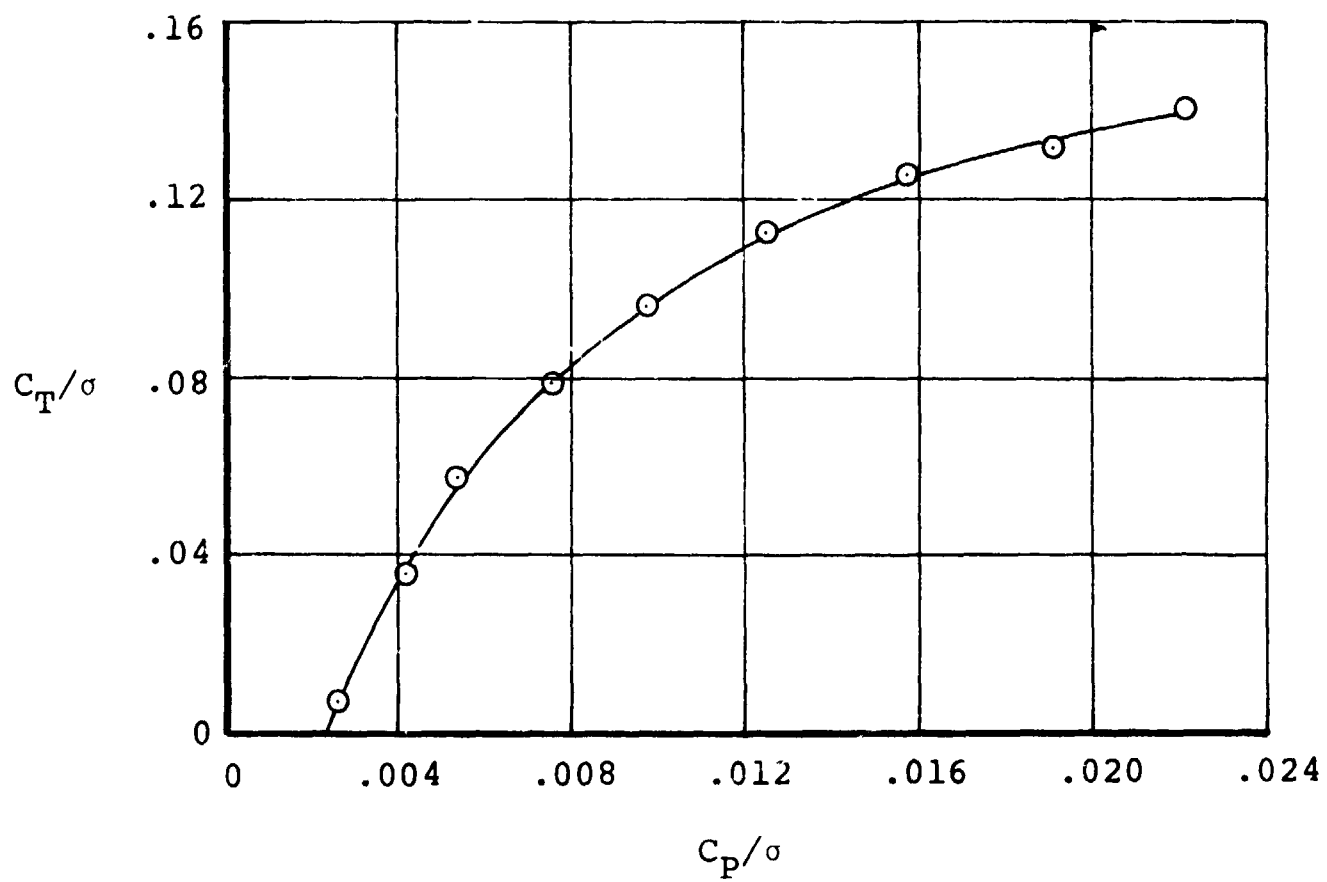


FIGURE 18

HOVER PERFORMANCE, $V_T = 250$ FT/SEC

$$Re \cong 0.3 \times 10^6 \quad M = 0.17,$$

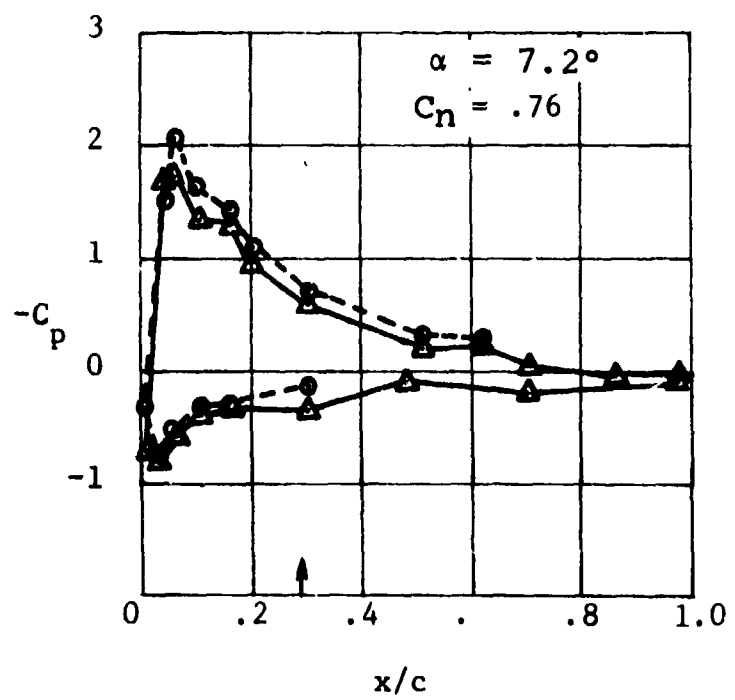
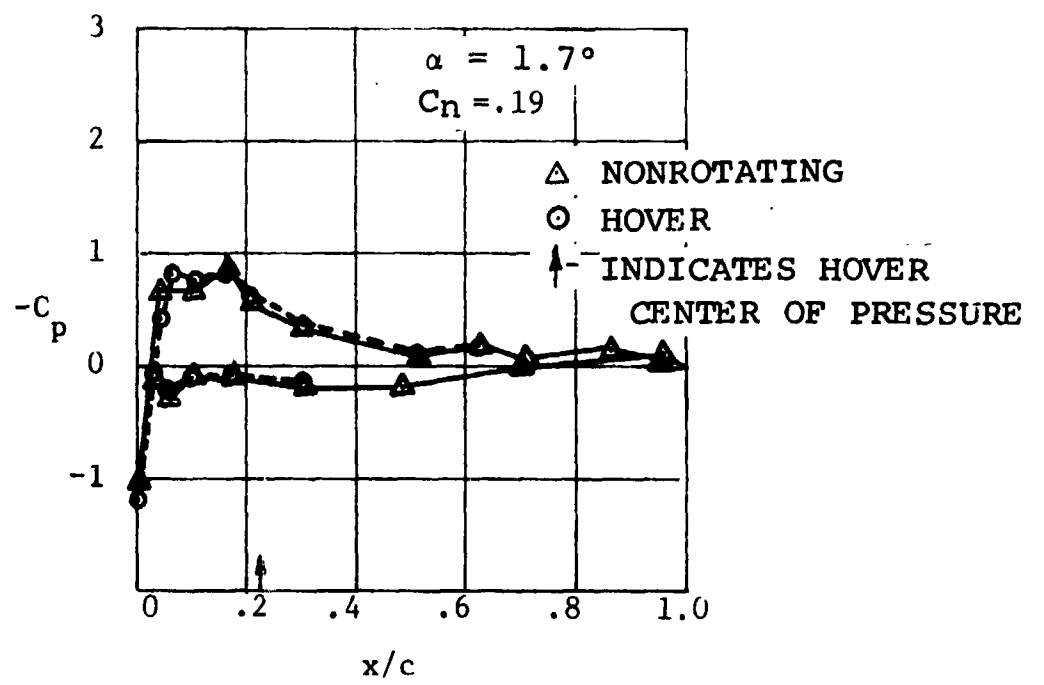
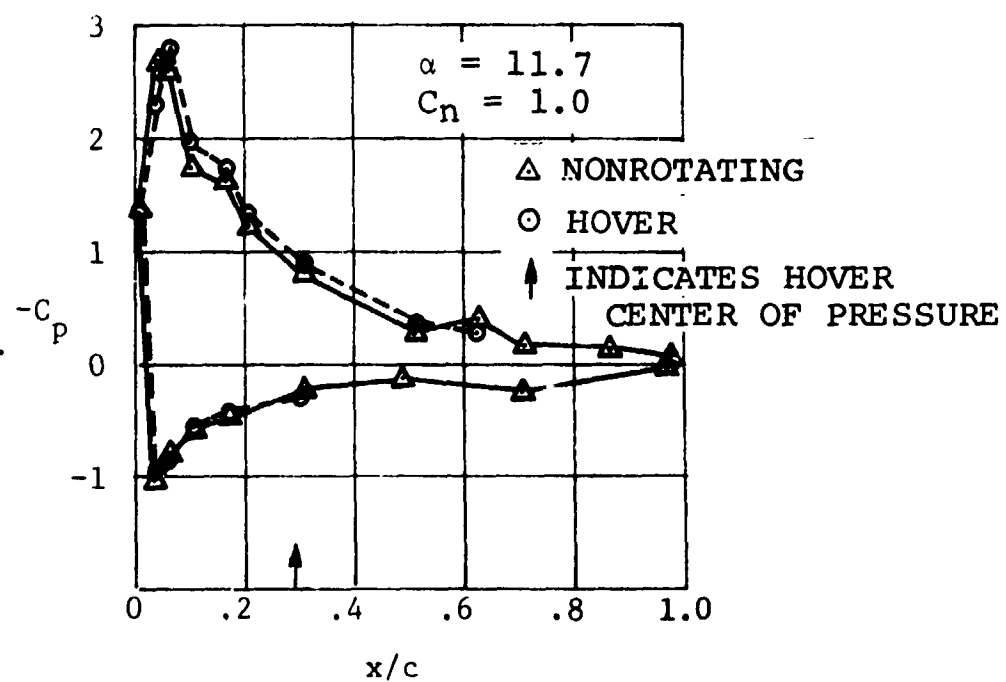


FIGURE 19

COMPARISON OF HOVER AND STATIC PRESSURE DISTRIBUTION

$$Re \approx 0.3 \times 10^6$$

$$M = 0.17,$$



SOLID SYMBOLS DENOTE OBSERVED STALL CHARACTERISTICS

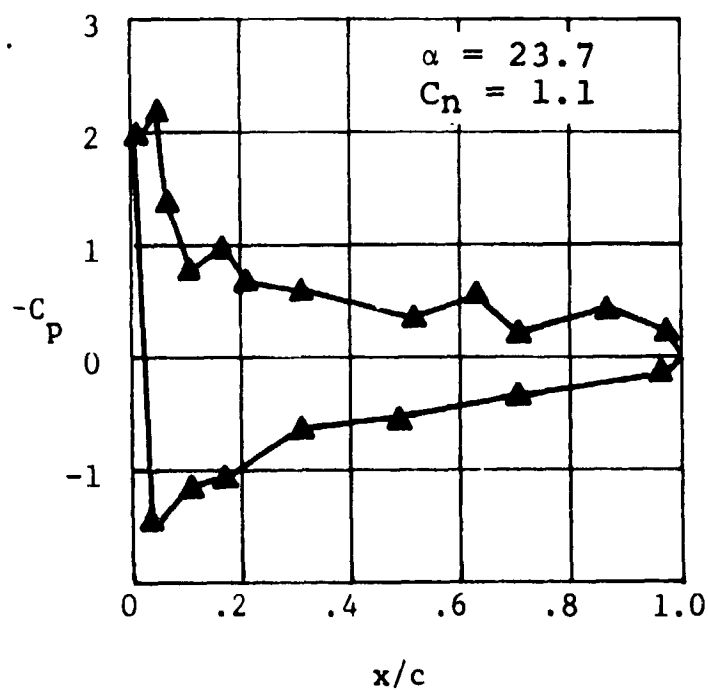


FIGURE 20

COMPARISON OF HOVER AND STATIC
PRESSURE DISTRIBUTIONS

is symptomatic of what is happening at the local blade element. Rotor problems like the decrease in control sensitivity to collective pitch at high rotor thrusts, drop off of propulsive capability as advance ratio increases and rapid increases in power required as thrust increases are symptomatic of local blade element stall. The rotor performance measurements from this test are discussed, therefore, as indicators of the type of blade element events that can be expected on the rotor.

From observation of the forward flight performance data obtained at advance ratios of $\mu = .15$, $\mu = .35$, and $\mu = .6$ at tip speeds of 250 feet/second, a decrease in the rotor lift curve slope ($d(C_T/\sigma)/d\alpha_s$) signaling the onset of both lift and moment stall is apparent. This decrease in slope (Figure 21) affects the rotor sensitivity to control inputs at high gross weights and adversely affects the helicopter flying qualities. The lower graph of Figure 21 illustrates that as the advance ratio increases, the onset of rotor lift curve slope deterioration occurs at progressively lower values of thrust. Once stall is present, a large rise in the rotor equivalent drag takes place ($D_e = P/V - X$). Figures 22, 23, and 24 illustrate the lift-drag polars at advance ratios of .15, .35, and .6 obtained during this test. The rapid rise in equivalent drag can be clearly seen at a $C_T/\sigma = .075$, $\mu = .35$, and also at a $C_T/\sigma = .06$, $\mu = .6$. The thrust coefficients where a large rise in equivalent drag is noted also correlate with the thrust coefficients where a decrease in the rotor lift curve slope occurs.

The propulsive efficiency of the rotor $dX/d(P/V)$ is also symptomatic of stall on the rotor disc (Figure 25). At an advance ratio of .15 and a C_T/σ of .08, the propulsive efficiency of the rotor is nearly 100 percent, indicating little increase in drag at a constant thrust as propulsive force is increased. At a $\mu = .35$, the propulsive efficiency has dropped to around 88 percent at a $C_T/\sigma = .08$, but the rotor can still propel effectively. However, at a $\mu = .6$, the rotor is unable to propel itself at all. There, the propulsive efficiency varies from nearly 100 percent to negative values but at no time is the rotor propulsive force sufficient to overcome the rotor blade's own drag. At the high advance ratios, the drag on the advancing and retreating blades, where little lift is produced, creates a large force that the rotor must overcome to propel itself. As the power and shaft angle are increased at constant thrust to try to obtain more

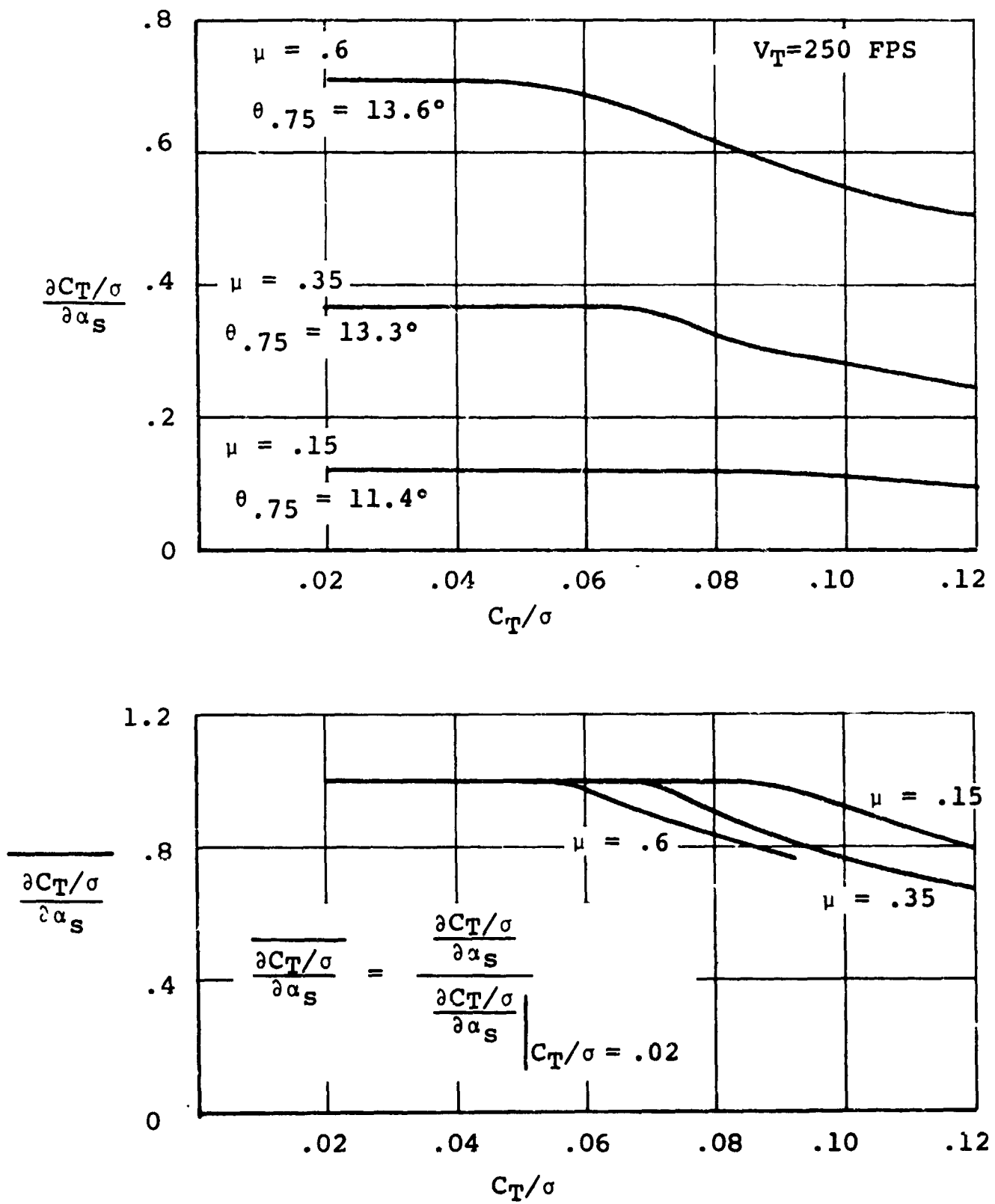


FIGURE 21

DECAY OF ROTOR SENSITIVITY TO α_s

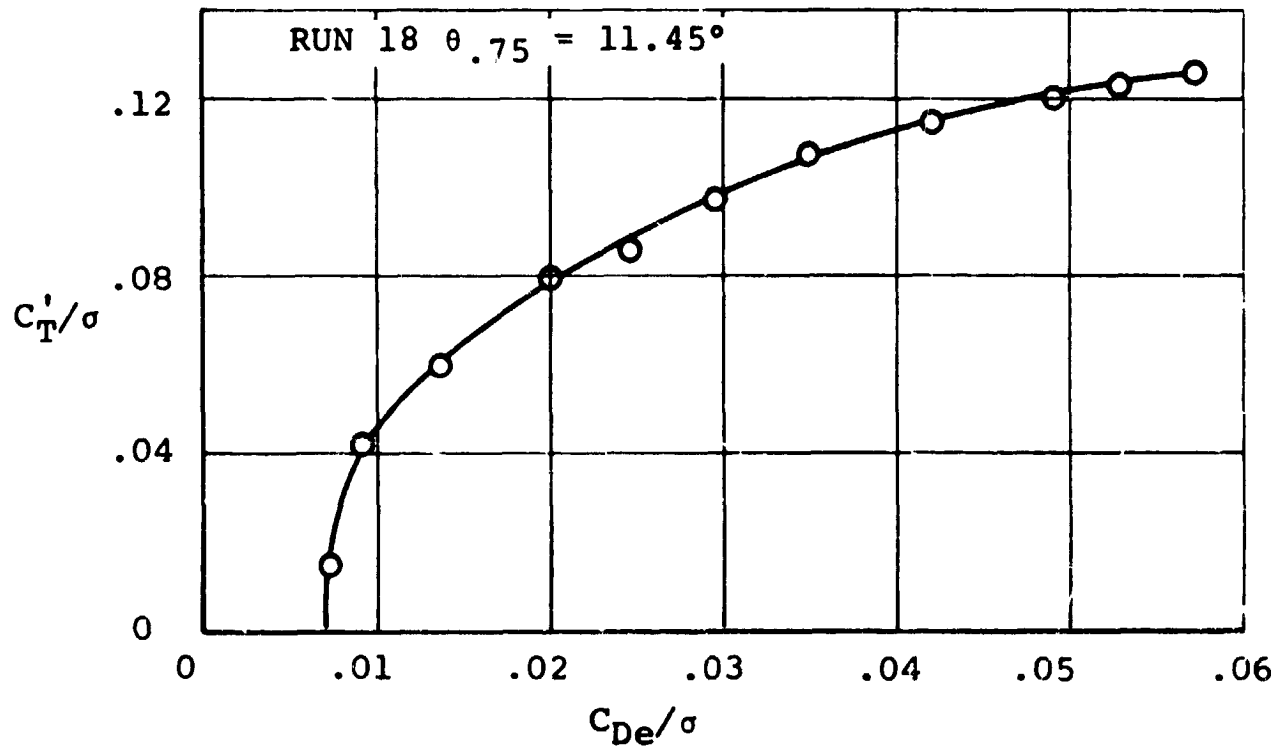
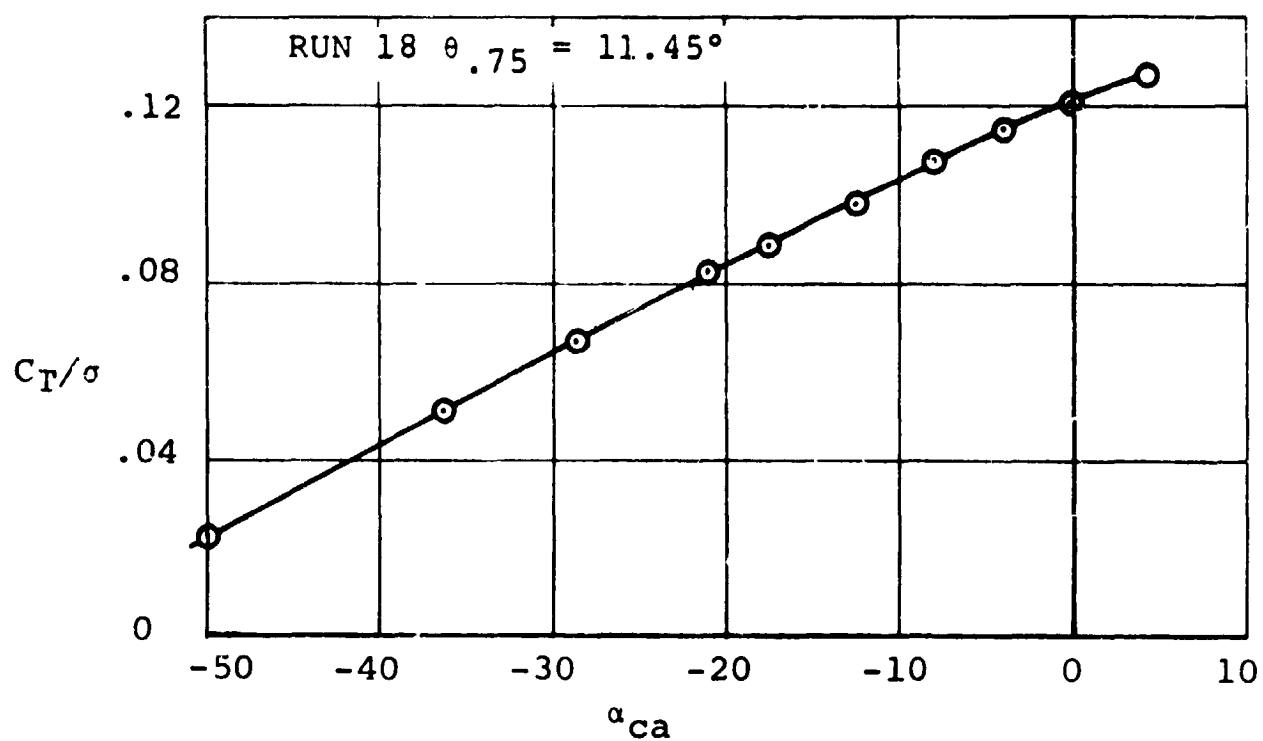


FIGURE 22

ROTOR PERFORMANCE AT $\mu = .15$, $V_T = 250$ FFS

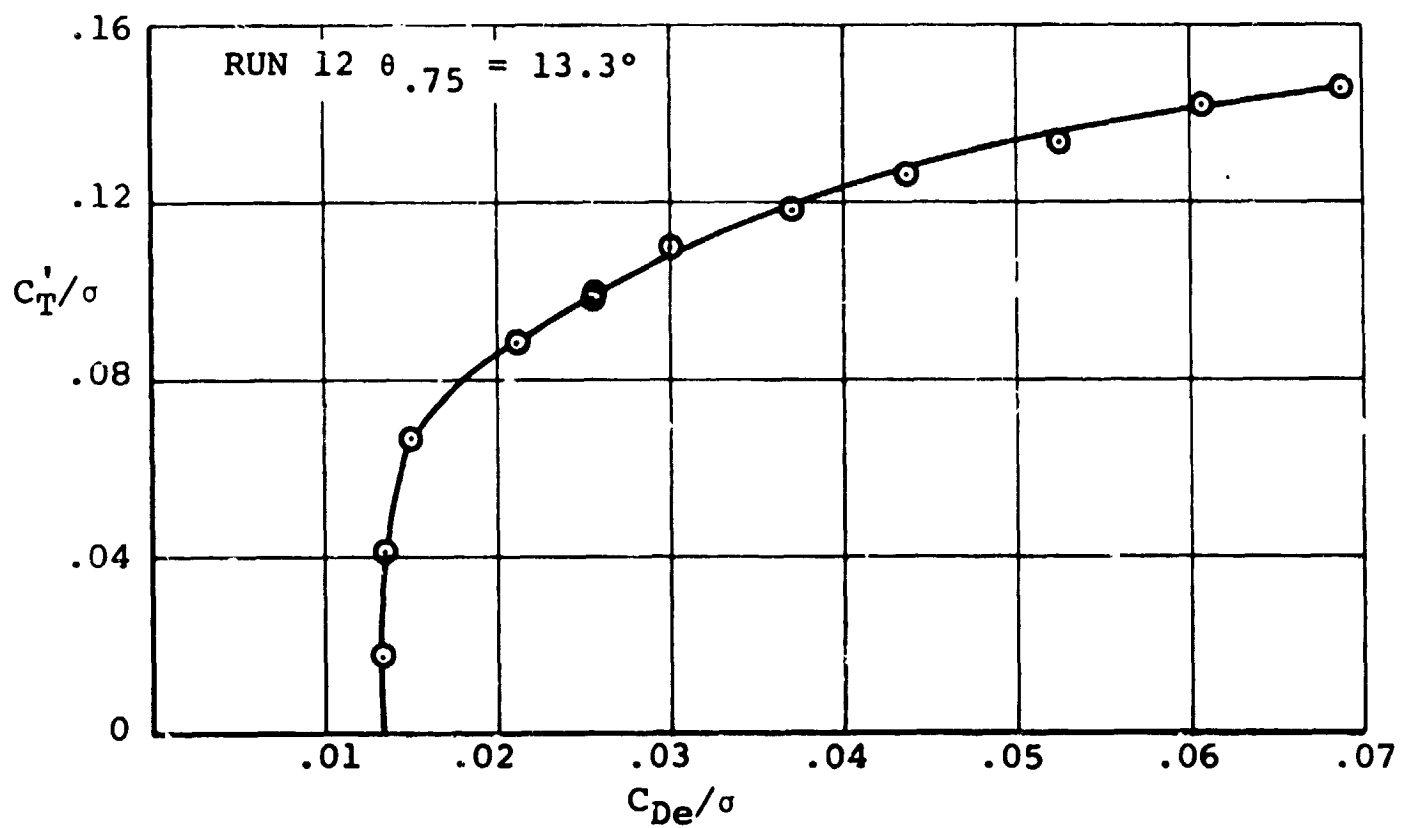
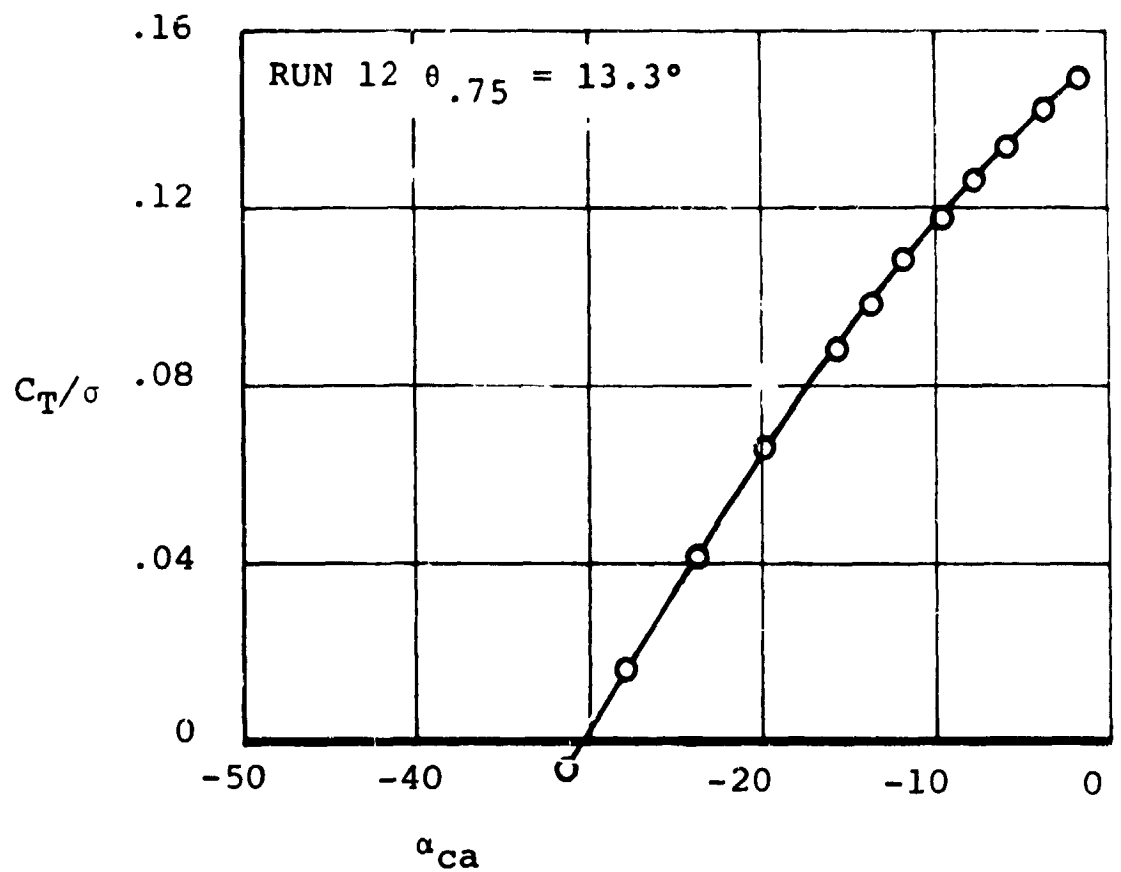


FIGURE 23 ROTOR PERFORMANCE AT $\nu = .35$, $V_T = 250$ FPS

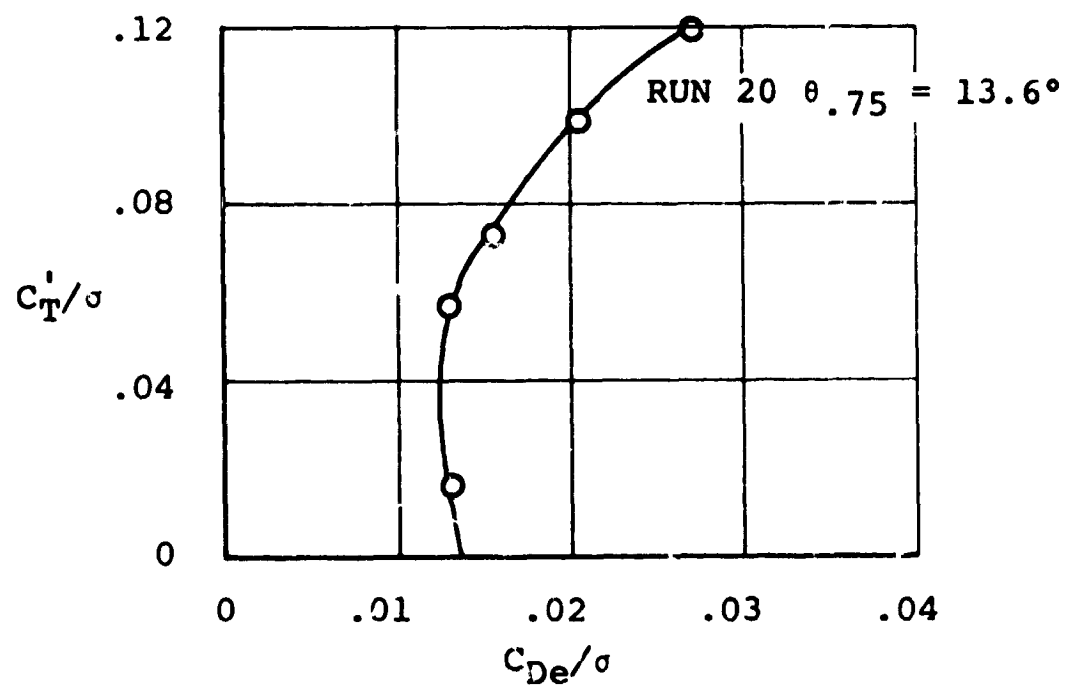
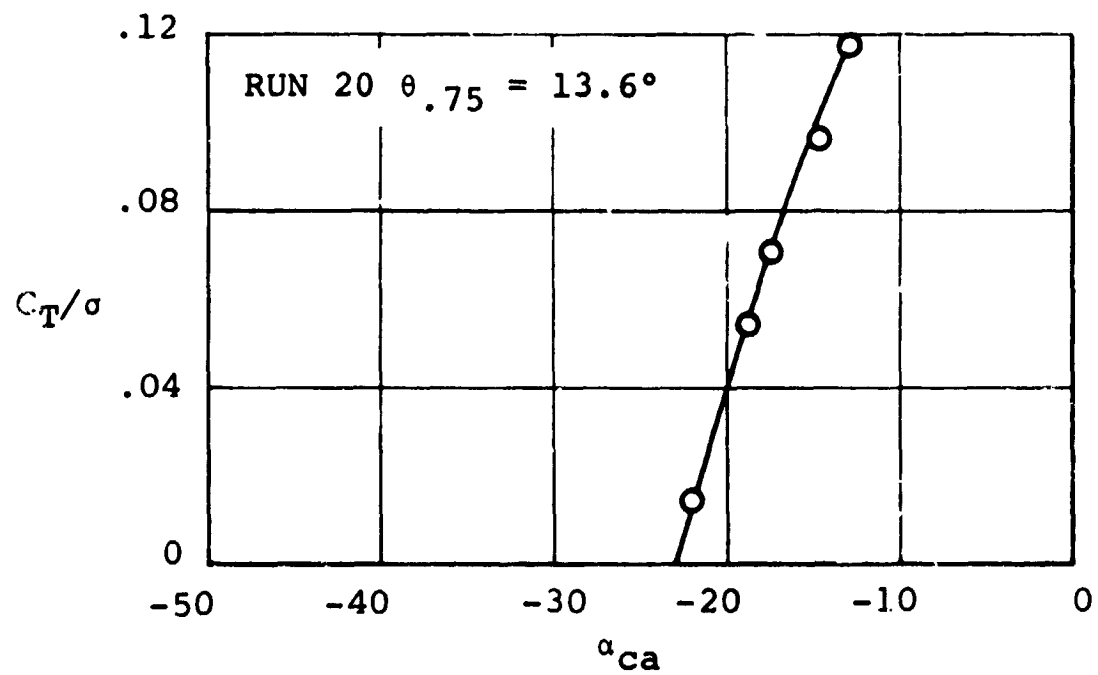


FIGURE 24 ROTOR PERFORMANCE AT $A = .6$, $V_T = 250$ FPS

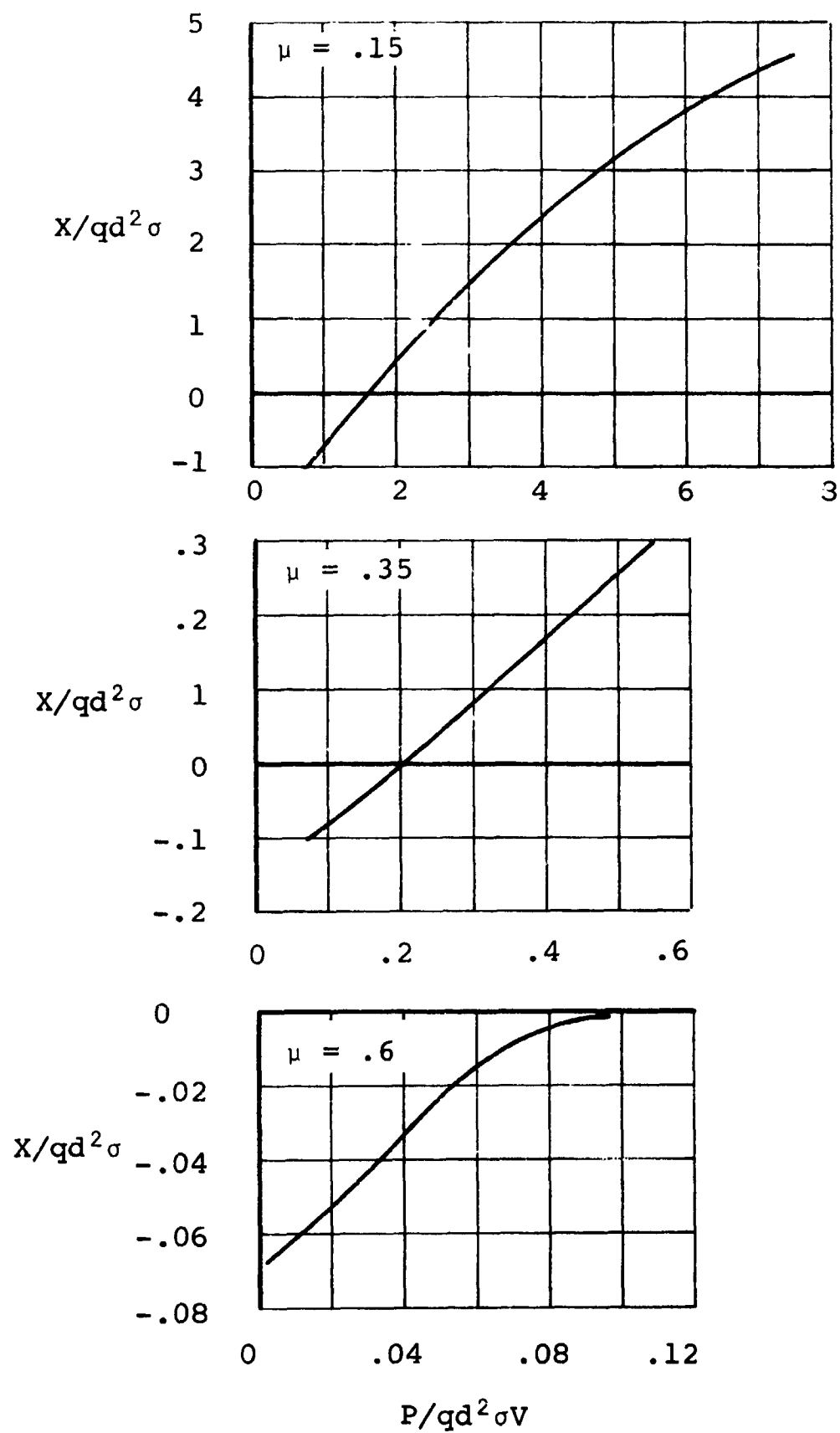


FIGURE 25

ROTOR PROPULSIVE EFFICIENCY AT

$$C_T'/\sigma = .08, V_T = 250 \text{ FPS}$$

propulsion, stall occurs on the retreating blade portion of the rotor disc. The loss of lift there, due to the stall, occurs where the rotor would use it more effectively for propulsion. This stall is not only responsible for reduced propulsion, but it also contributes largely to the rotor power required. It is interesting to note that large down flapping, and in some instances droop stop pounding, occurred at $\psi = 50$ to 60 degrees for these high advance ratio high thrust test runs, a direct result of the stall on the rotor disc.

Stall Events at an Advance Ratio of .35. - A particularly informative set of data for discussion of the stall mechanisms observed during the forward flight segment of this test was obtained at an advance ratio of .35 and a tip speed of 500 ft/sec. The run consisted of a series of test points obtained during a shaft angle sweep from $\alpha_s = -27$ degrees, $C_T/\sigma = 0$ to a shaft angle of -1 degree, $C_T/\sigma = .15$. Collective pitch was held constant at $\theta_{.75} = 13.5$ degrees and the tunnel speed was 105 knots. Figure 26 illustrates key performance trends obtained during the run. From these performance plots, the stall onset on the rotor disc occurs after a $C_T/\sigma = .08$.

Figure 27 illustrates the angle of attack obtained from the differential pressure transducers on both the pressure blade and the skin friction blade for three of the test points. This degree of correlation ensures that the pressure results and skin friction results can be discussed at the same blade element and rotor environment. These points consist of data obtained just prior to stall onset, in moderate stall, and in deep stall and occur at C_T/σ 's of .073, .105, and .132, respectively. Figures 28, 29, and 30 show integrated pressure data for the three test points under discussion. All three points show trends characteristic of an articulated rotor with minimum C_n on the advancing side and maximum C_n on the retreating side of the rotor disc. Note that $C_{n_{max}}$ occurs around $\psi = 240$ degrees for all three points.

The C_m versus ψ plot associated with the test point at a $C_T/\sigma = .073$ indicates C_m (on the retreating side of the rotor disc) values that, when compared with levels from static data (Figure 14), would be statically characteristic of moderate moment stall at an angle of attack of 17 degrees. However, the usual sharp drops in C_m associated with moment stall are not seen. Although the performance curves of Figure 23 show no evidence of stall, the maximum normal force on the retreating side of the blade exceeds the static $C_{n_{max}}$ at the model scale Reynolds number. This value of normal force, however, does not exceed the static $C_{n_{max}}$ value at the full scale Reynolds number. The state of the rotor, therefore, is not clear, but it is interpreted that this point is unstalled in lift and showing signs of moment stall onset.

The variation in static $C_{n_{max}}$ with azimuth at model scale

$\mu = .35, \theta_{.75} = 13.5^\circ, V_T = 500 \text{ Ft/Sec}$

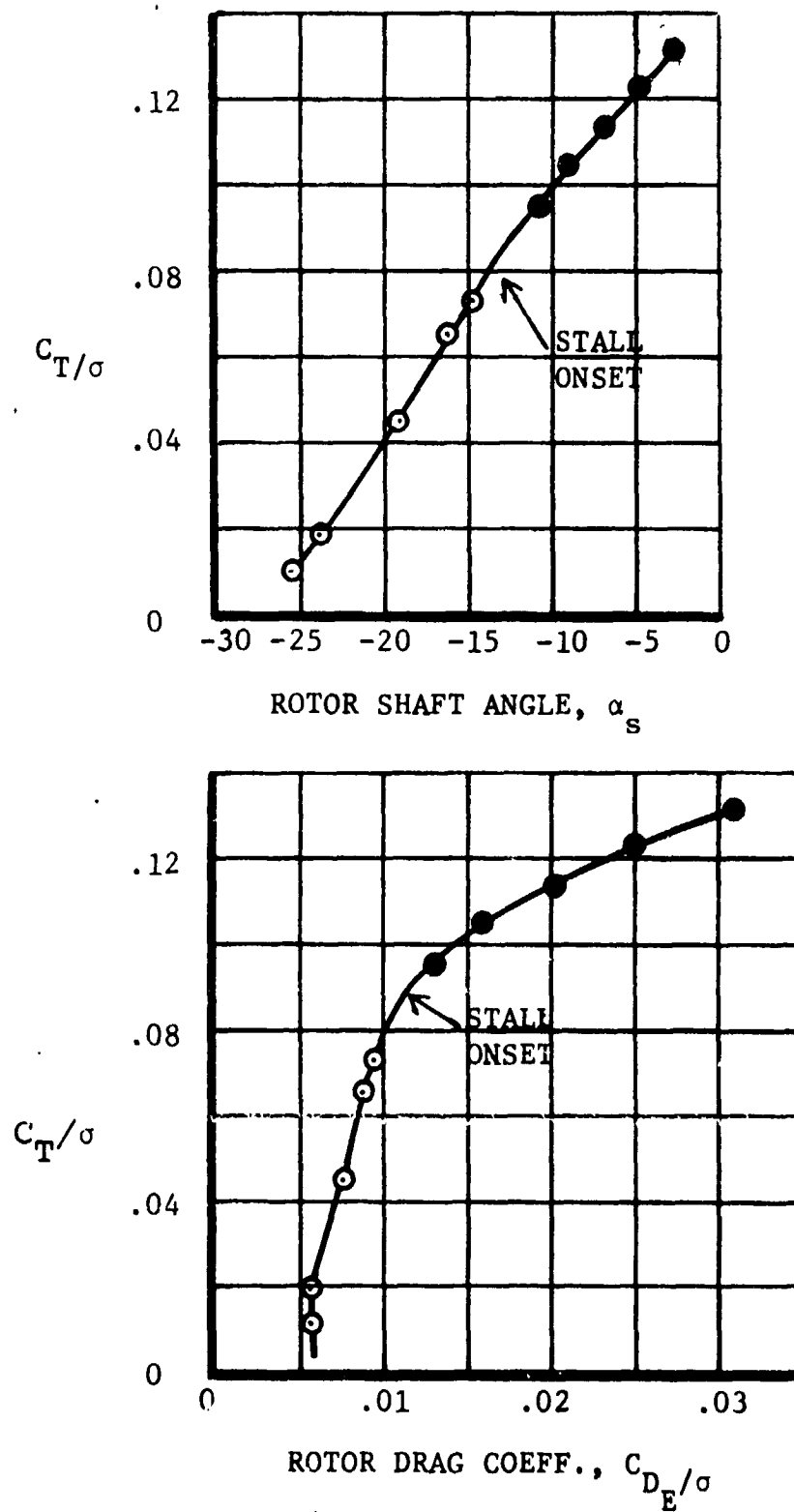


FIGURE 26

MODEL ROTOR PERFORMANCE DATA
IN FORWARD FLIGHT

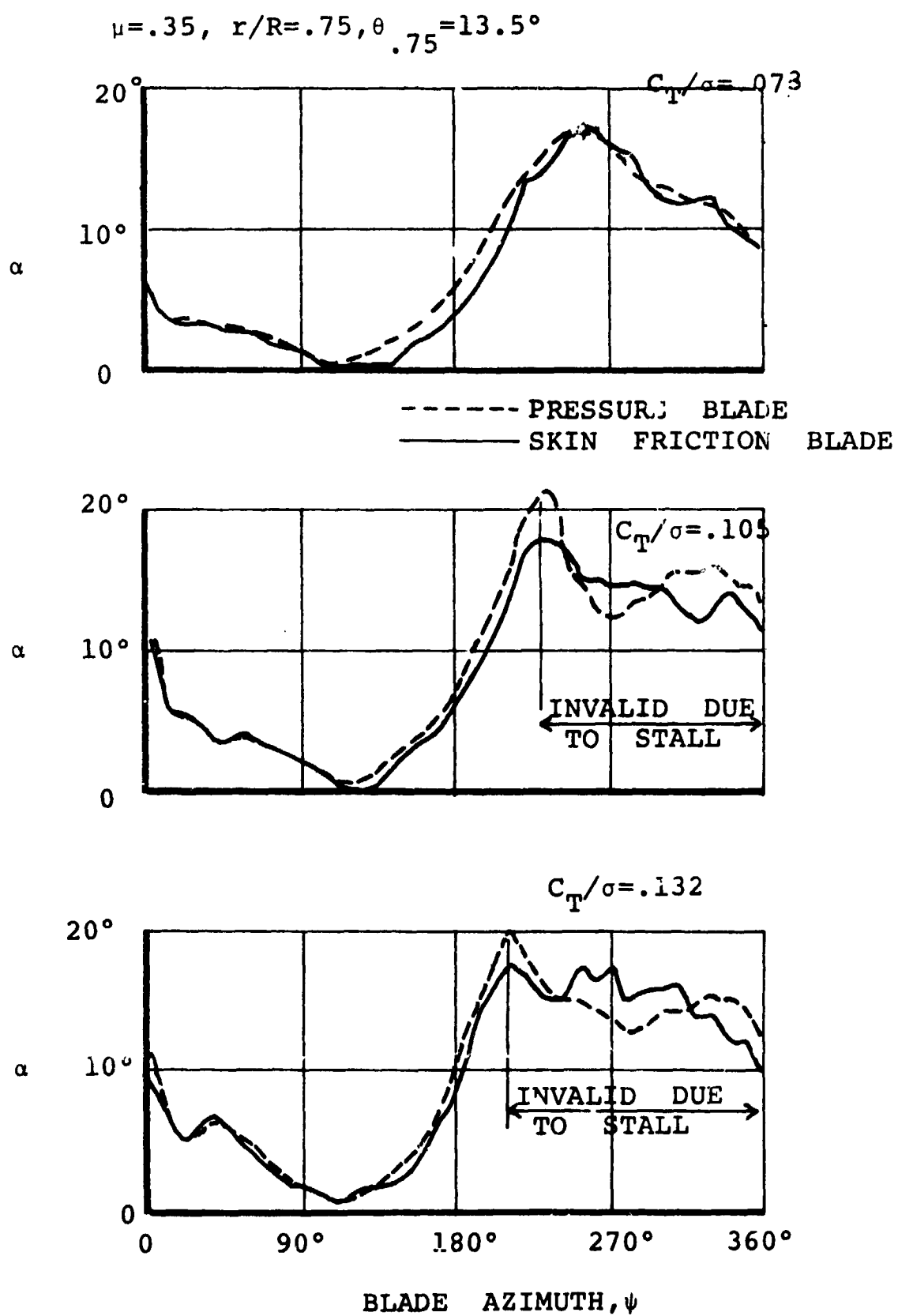


FIGURE 2'7

MEASURED ANGLES OF ATTACK ON THE
PRESSURE AND SKIN FRICTION BLADES

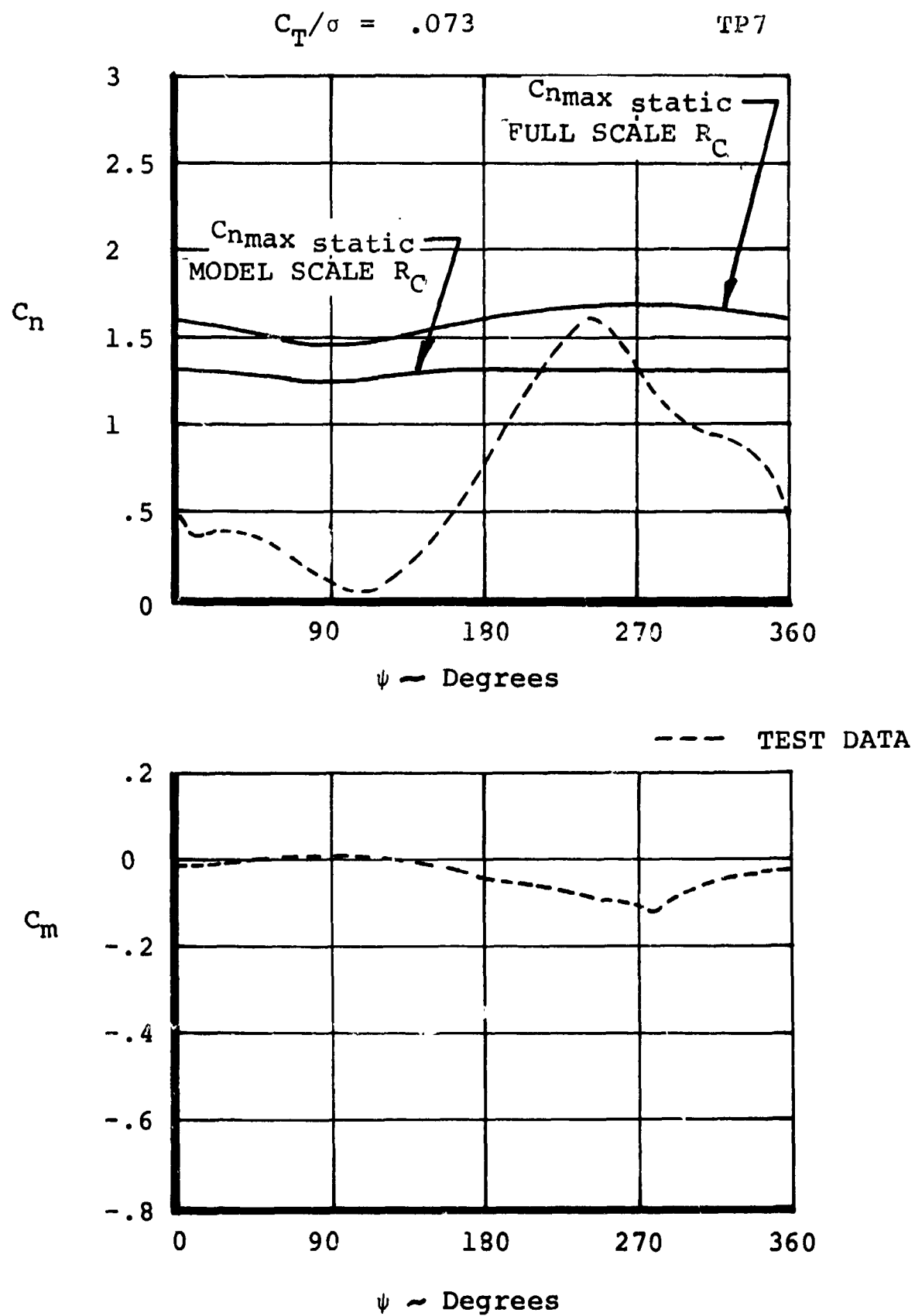


FIGURE 28

AERODYNAMIC COEFFICIENTS OBTAINED
FROM INTEGRATED PRESSURES @ $r/R = 0.75$
 $\mu = .35, 0.75 = 13.5, V_T = 500$ FPS

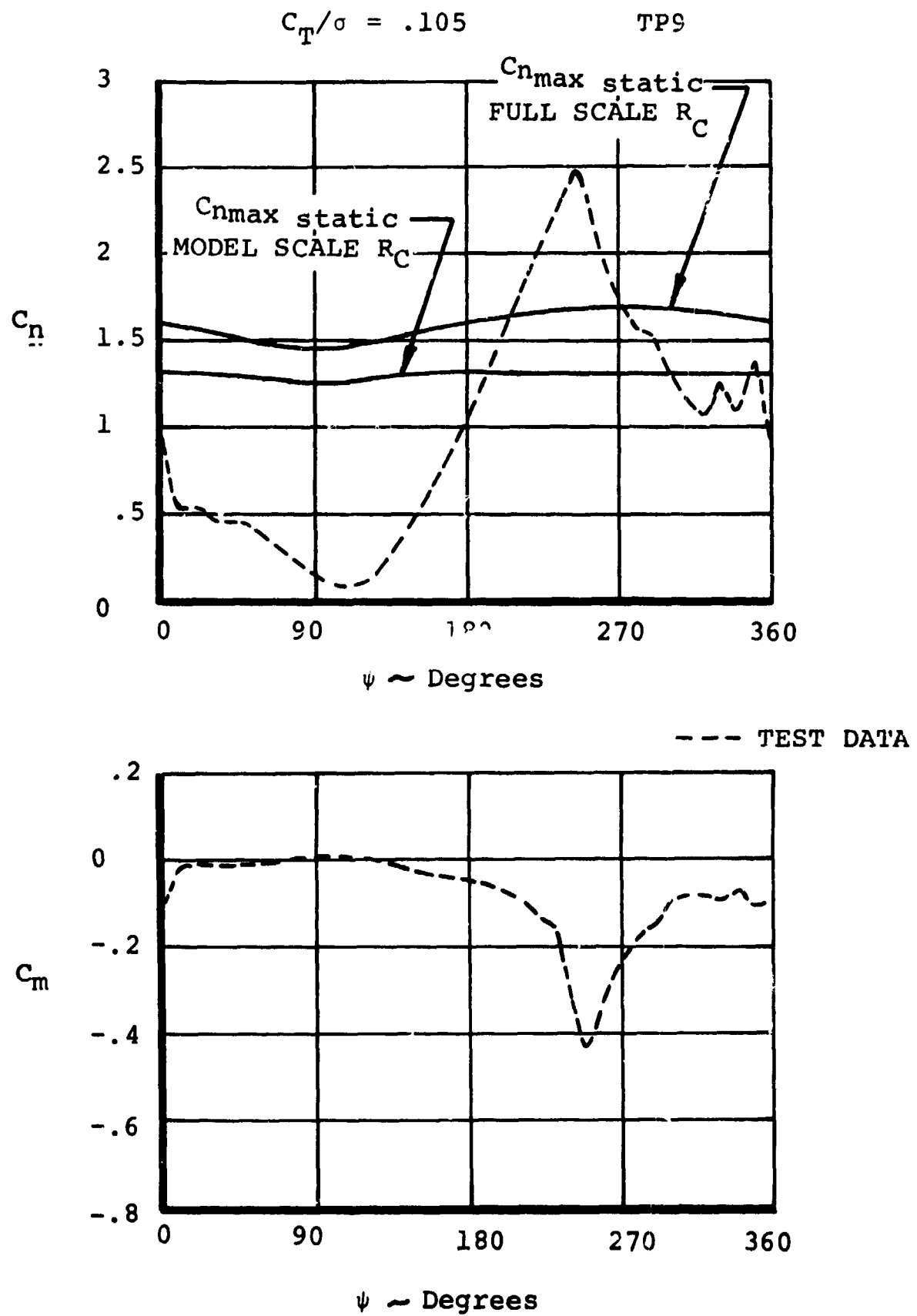


FIGURE 29

AERODYNAMIC COEFFICIENTS OBTAINED
FROM INTEGRATED PRESSURES @ $r/R = 0.75$
 $\mu = .35$, $\theta_{.75} = 13.5$, $V_T = 500$ FPS

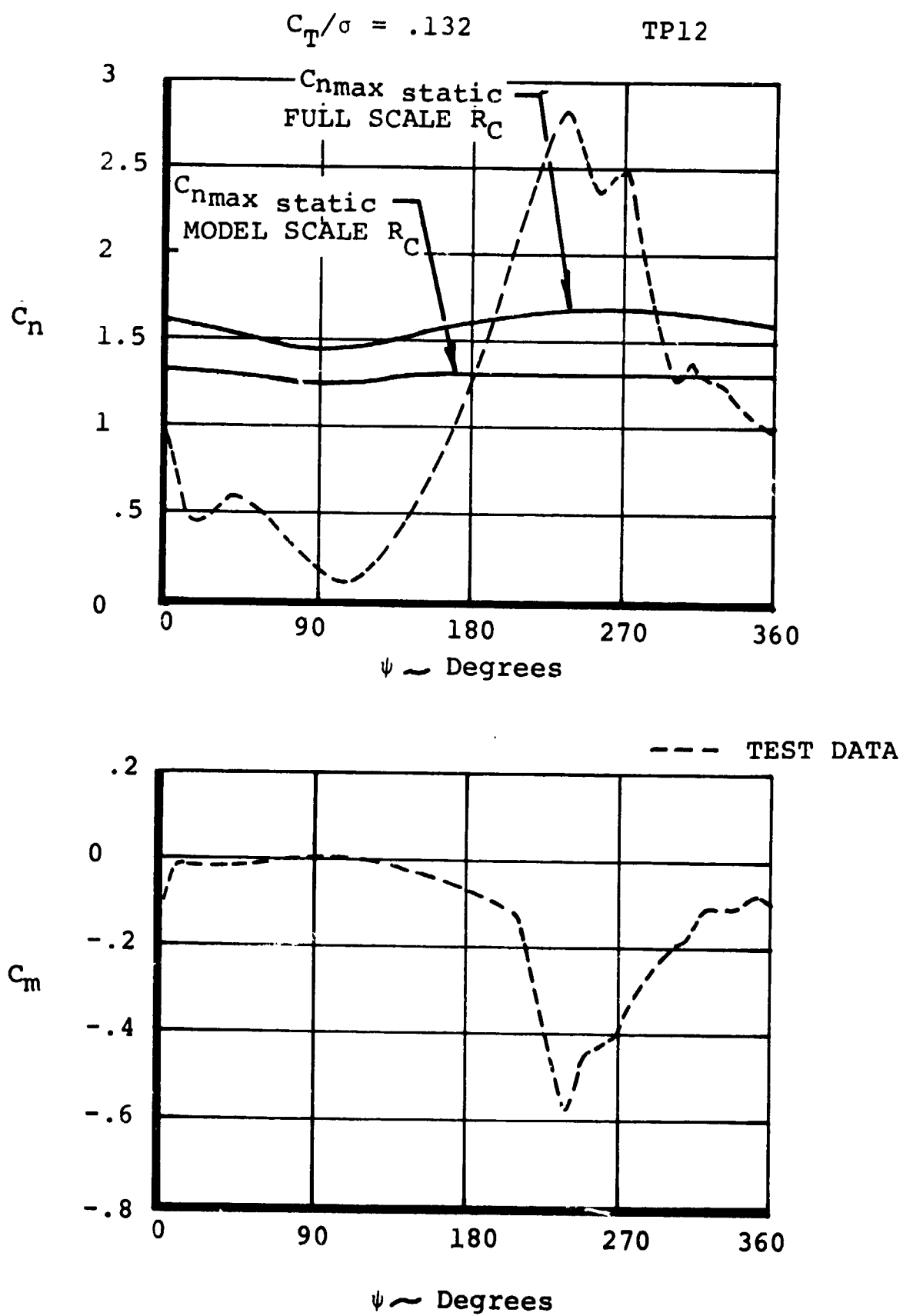


FIGURE 30

AERODYNAMIC COEFFICIENTS OBTAINED
FROM INTEGRATED PRESSURES @ $r/R = 0.75$
 $\mu = .35$, $\theta_{.75} = 13.5$, $V_T = 500$ FPS

Reynolds numbers (Figure 28 and throughout the remainder of the report) was obtained from Boeing Vertol Wind Tunnel Test 074-077 where the variation of C_{nmax} with Mach number was acquired.

At a C_T/σ of .105, Figure 29, the rotor is stalled on the retreating side of the disc. This is verified by investigation of the rotor performance curves of Figure 23. C_m is achieving values beyond those characteristic of the static stall, and the static stall values of C_n at full-scale Reynolds numbers have been significantly exceeded (dynamic lift overshoot). A rapid change in both pitching moment and lift is also apparent as the blade enters the stall region.

At a C_T/σ of .132, Figure 30, the stall is severe. C_m approaches values of $-.6$ and C_n is experiencing its maximum at values of 2.8 . The rotor performance shown in Figure 26 has deteriorated significantly from the prestall values.

These three test points reconfirm that on a rotor in forward flight, static values of C_{nmax} are greatly exceeded. They also illustrate that the static values of C_m are exceeded as well, and the higher the thrust, the more dynamic overshoot occurs. In stall, both C_{nmax} and C_{mmax} are being reached at nearly the same time. This disagrees with static results which indicate that the maximum C_n and C_m do not occur simultaneously and could indicate a further change in stall type due to dynamic characteristics.

Figure 31 shows the C_{nmax} that was achieved for each test point of the subject run and shows the stagnation pressure coefficients, C_p , that were measured at the same azimuth position. The measured values greater than 1.0 are not normally expected. They are, however, representative of the local q and indicate that it was somewhat higher than expected. The local velocities in the azimuth region where the data were obtained and q theory was calculated are in the order of 250 feet/second. They consist of inplane velocities due to rotation of the blades as well as velocities due to downwash and blade flapping. No significant velocities due to strong tip vortices are near the blade in the azimuth region where the maximum values are obtained.

Further review of the blade element airload characteristics can be achieved by looking at the integrated pressure results as shown in Figure 32. These plots of C_n and C_m versus azimuth indicate that the test point of $C_T/\sigma = .132$ is more severely stalled than that of $C_T/\sigma = .105$. The fact that the C_n and C_m values from the three test points collapse to form a single line in the range $10 \text{ degrees} \leq \psi \leq 210 \text{ degrees}$ indicates that nearly identical pressure distributions exist. The dynamic extension of the lift and moment coefficients is again obvious.

$$R_c \approx 0.3 \times 10^6$$

$$\mu = 0.35, V_T = 500 \text{ FT/SEC}$$

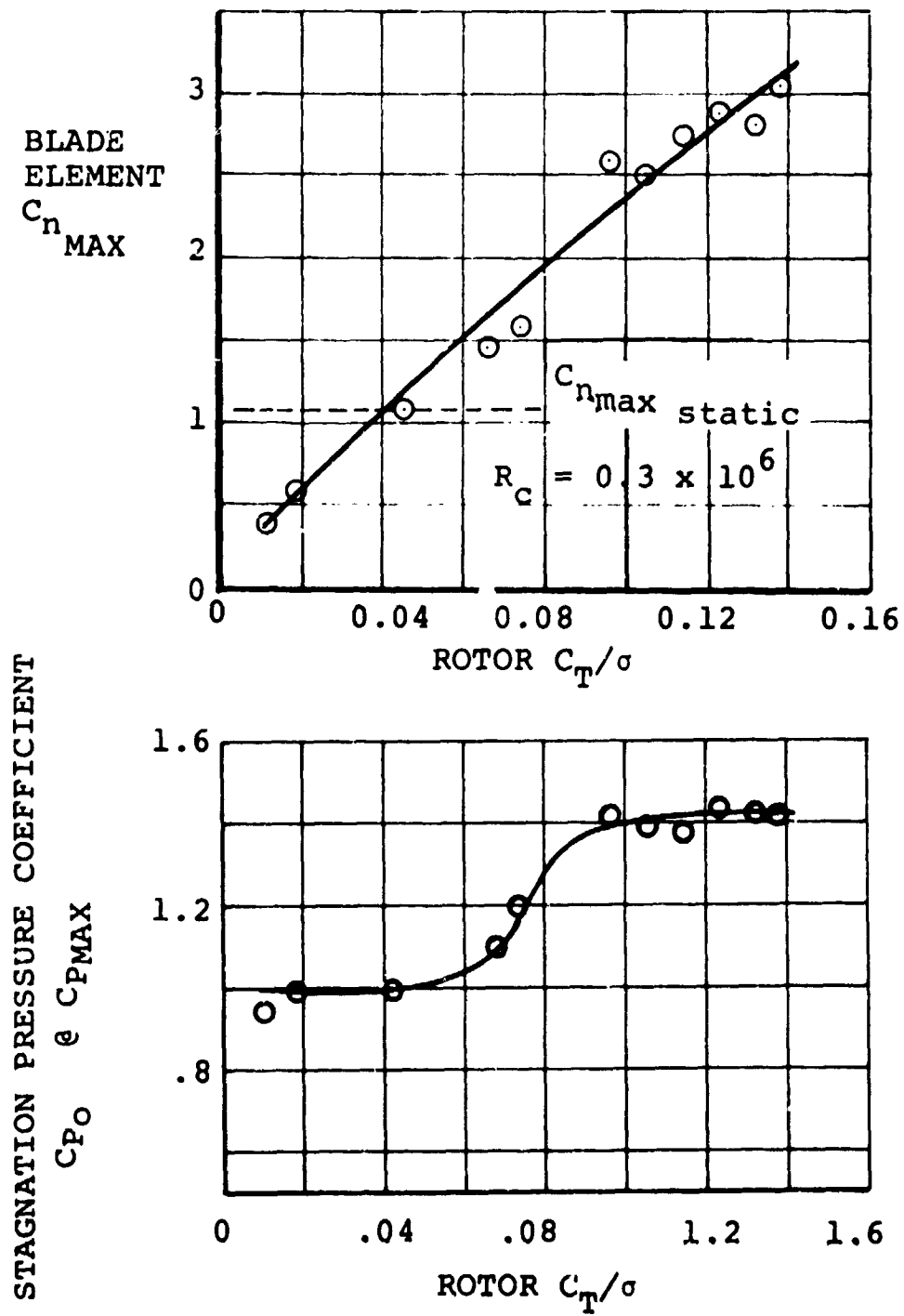


FIGURE 31

MAXIMUM BLADE LOADS

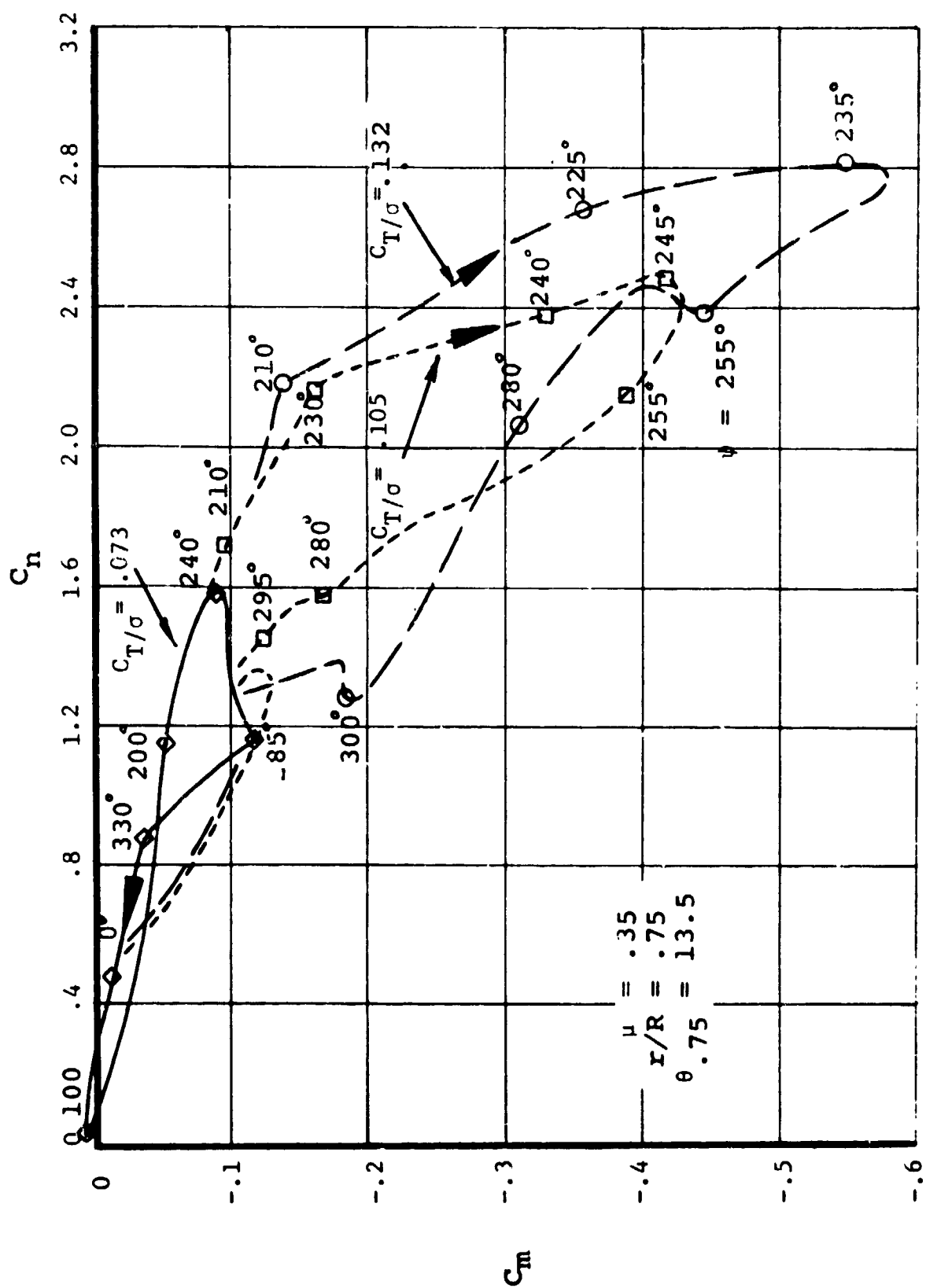


FIGURE 32

MEASURED AIRLOADS AT $V_T = 500$ fps AND VARIOUS THRUST LEVELS, $\mu = 0.35$

when C_n is plotted versus the angle of attack obtained from the differential pressure (Figure 33), hysteresis phenomena are observed. Similarly, the curve of Figure 34 represents the hysteresis effect in the stalled region. These curves exhibit the basic characteristics of the hysteresis loops seen during oscillating airfoil tests at higher Reynolds number (Reference 1) and are somewhat similar to the theoretically predicted unsteady 3-dimensional C_L versus α loops illustrated in Figure 35 for the test point at a $C_T/\sigma = .132$.

The C_n versus α loops illustrate the dynamic extension of lift over the statically measured values and indicate similar air-load trends for the blade element at all test points of the run when the angle of attack is increasing.

Stall Onset at an Advance Ratio of .35: A Series of Separate Events. - The integrated results discussed so far present a general view of the trends observed in the measured data. They have shown the similarity of the airloads in the first and second quadrants of the rotor disc and have also indicated that in the third quadrant of the rotor disc, dynamic extensions of both lift and moment exceed their static 2-D values. A more detailed look at the data is now in order, especially in the region of stall onset from $\psi = 200$ degrees to 240 degrees.

In the third quadrant of the rotor disc, as the blade sweeps around the azimuth past $\psi = 180$ degrees and toward $\psi = 270$ degrees, it experiences a sequence of several major identifiable events that occur prior to complete blade stall. In the present experiment, these events occurred over an azimuth region of 40 degrees and climax with the achievement of maximum C_n . Blade element pressure distributions, skin friction distributions, and the C_n versus C_m plot for the test point at $\mu' = .35$, $V_T = 500$ feet/second, $C_T/\sigma = .132$, $\alpha_s = -3.0$ degrees are used in the following discussion to illustrate the events.

As the blade traverses the advancing blade azimuth region from $\psi = 20$ degrees to $\psi = 180$ degrees, the measured surface streamlines essentially follow the theoretical local sweep angles constructed from U_t and $V_\infty \cos \psi$. In the second quadrant, the blade element circulation per unit span inferred from the integrated measured pressures, $\Gamma = 1/2 V_{Loc} C_L c$, increases rapidly. The measured pressure distributions remain similar to those measured statically as shown in Figure 36. As the blade passes $\psi = 200$ degrees, however, the similarity to static data is gone and subtle changes begin to take place while the stall onset region is entered. The skin friction instrumentation indicates a separation-like phenomenon, characterized by large-scale random flow oscillation in the boundary layer, and the surface streamlines on the upper surface suddenly start to turn radially outward with respect to the theoretical local sweep angle. The center of pressure, stable near the quarter

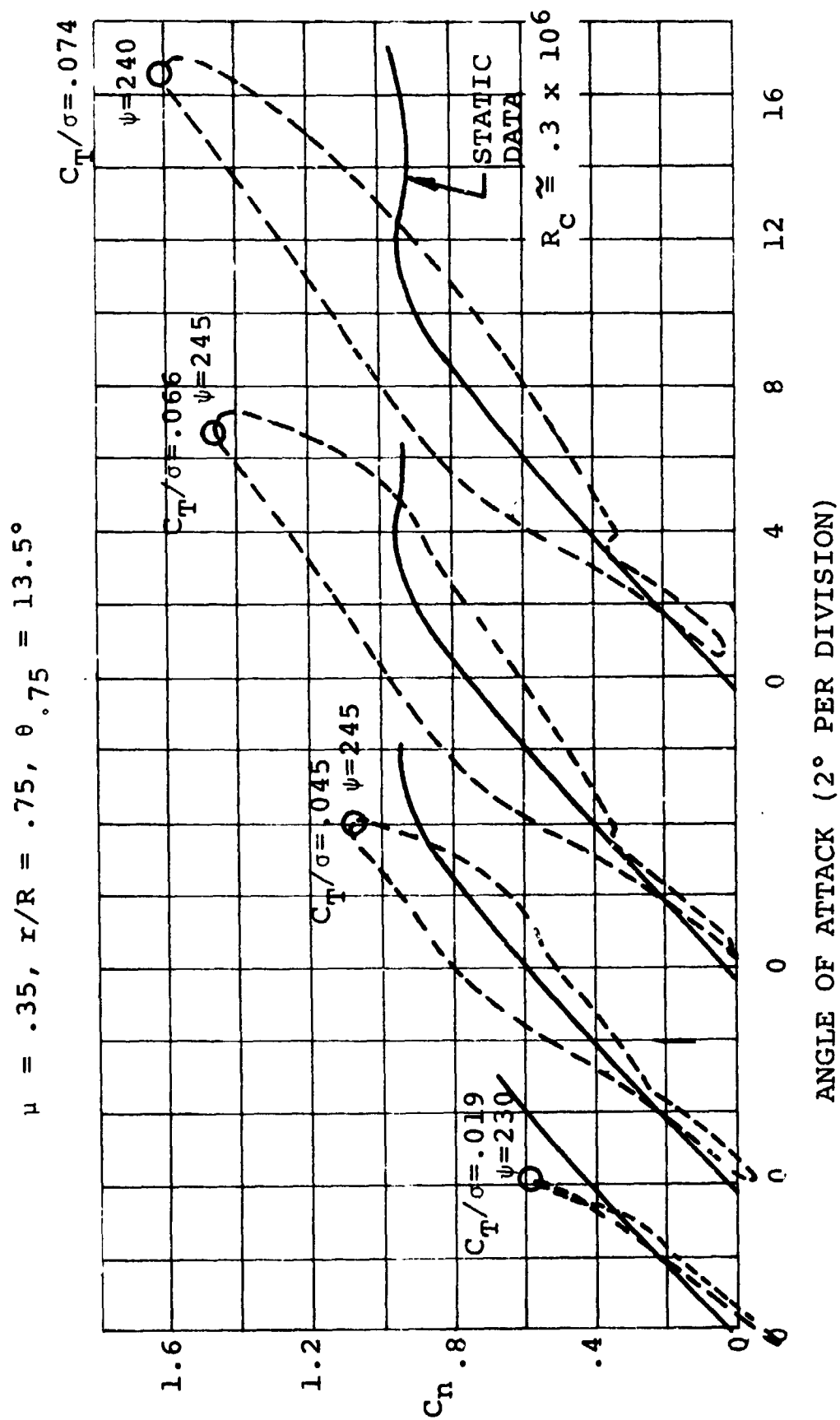


FIGURE 33 LIFT HYSTERESIS PRIOR TO SIGNS OF ROTOR STALL

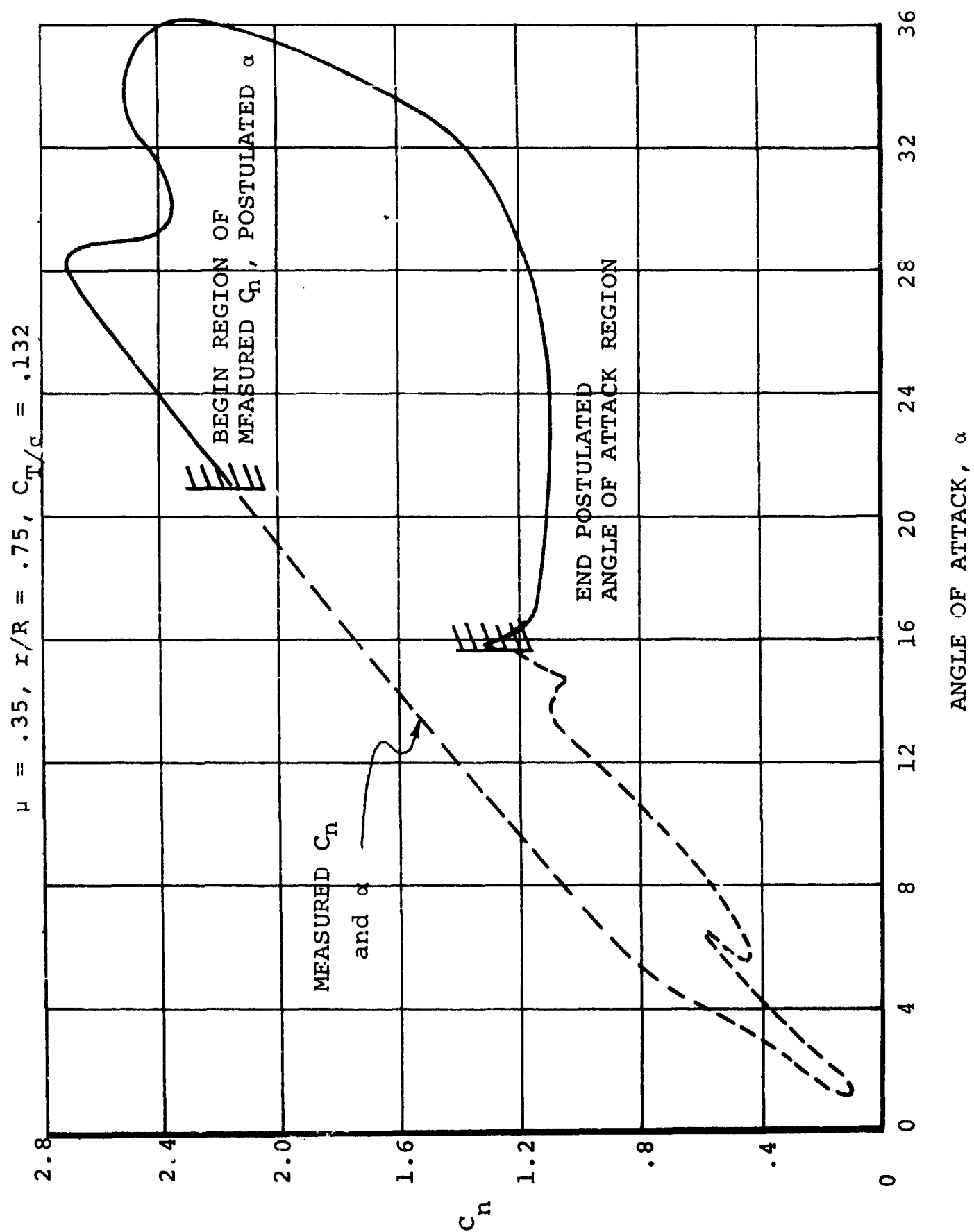


FIGURE 34

LIFT HYSTERESIS WITH BLADE STALL

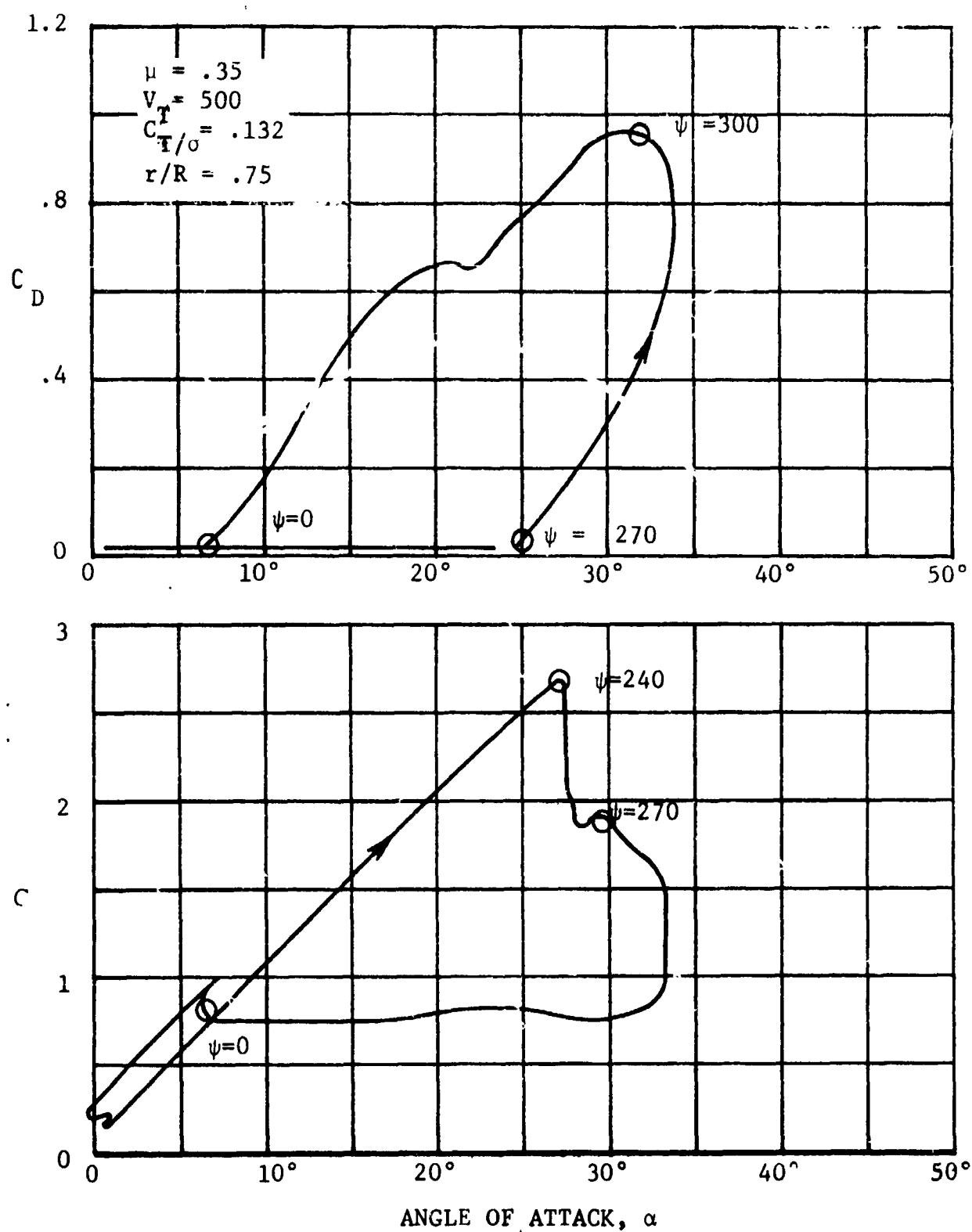


FIGURE 35 THEORETICAL ROTOR SECTION AIRFOIL CHARACTERISTICS USING EMPIRICAL RADIAL FLOW AND UNSTEADY CORRECTIONS

chord since $\psi = 120$ degrees, begins to shift aft. The pressure distribution, even though at a C_n of 2.0 and past the static stall value, is still exhibiting a very strong suction peak, and as the blade passes this azimuth, it experiences a slight increase in suction at mid-chord on the upper surface. This shows up on the C_n versus C_m plot of Figure 38 as a slight change in slope and the data depart from a trend they have been continuing since passing $\psi = 120$ degrees.

At the azimuth of 210 degrees, the lift, lift coefficient, and circulation are still increasing. The aft drift of the center of pressure accelerates and the onset of a rapid rise in nose-down pitching motion occurs (Figure 38). This event has been described as moment stall in Reference 8 and is definitely a separate event occurring during the stalling process. A further increase in suction is occurring at the mid-chord region and the leading edge suction peak is still clearly present as shown in Figure 37.

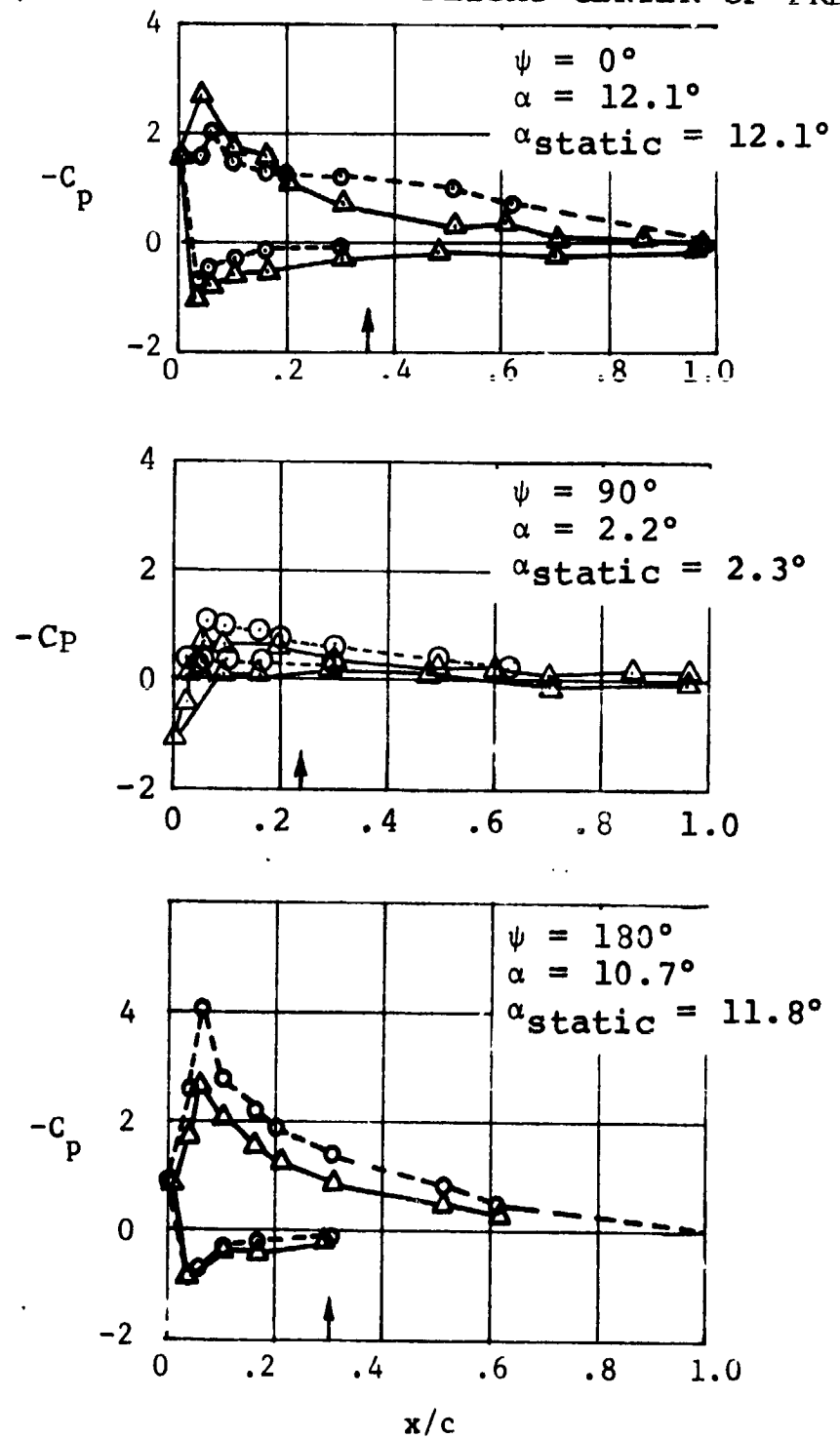
The suction peak at the leading edge starts to collapse at $\psi = 215$ degrees, but the mid-chord suction continues to grow. This keeps both the pitching moment and the normal force coefficients growing rapidly. The circulation continues to increase but at a slower rate than before, and Γ finally reaches a maximum value at $\psi = 225$ degrees.

Stall increases in severity as the blade progresses in azimuth. At a ψ of approximately 240 degrees, after a considerable overshoot of the static lift, the maximum C_n is achieved. The pressure coefficient at mid-chord on the upper surface has just passed its minimum value. The pitching moment coefficient is also near its maximum negative value, considerably higher than that achieved statically. A few more degrees further in azimuth and the lift stall occurs because of the reduction in the suction at mid-chord. As these events are occurring, the local circulation and lift force are decreasing at large rates.

The blade continues on its way, through a region of deep stall, past a ψ of 270 degrees and on to a ψ of 345 degrees. Variations of the pressure distribution occur throughout this region, but suction at the mid- and fore-chord on the upper surface remains a dominant feature. At $\psi = 345$ degrees, the blade passes in close proximity of a vortex shed by the preceding blade and then passes through the wake of the hub. At this time, the pressure distribution quickly changes to one similar to two-dimensional static data with an established leading edge suction. Stabilization of the center of pressure and re-establishment of the boundary layer unstalled flow characteristics soon follow as the blade begins another revolution.

When the pressure distributions are viewed as a continuous

Δ - NONROTATING DATA
 \circ - FORWARD FLIGHT DATA
 \uparrow - INDICATES FORWARD FLIGHT CENTER OF PRESSURE



$$\mu = .35, C_T/\sigma = 0.132, r/R = 0.75$$

FIGURE 36

PRESSURE DISTRIBUTION AT VARIOUS
AZIMUTH LOCATIONS

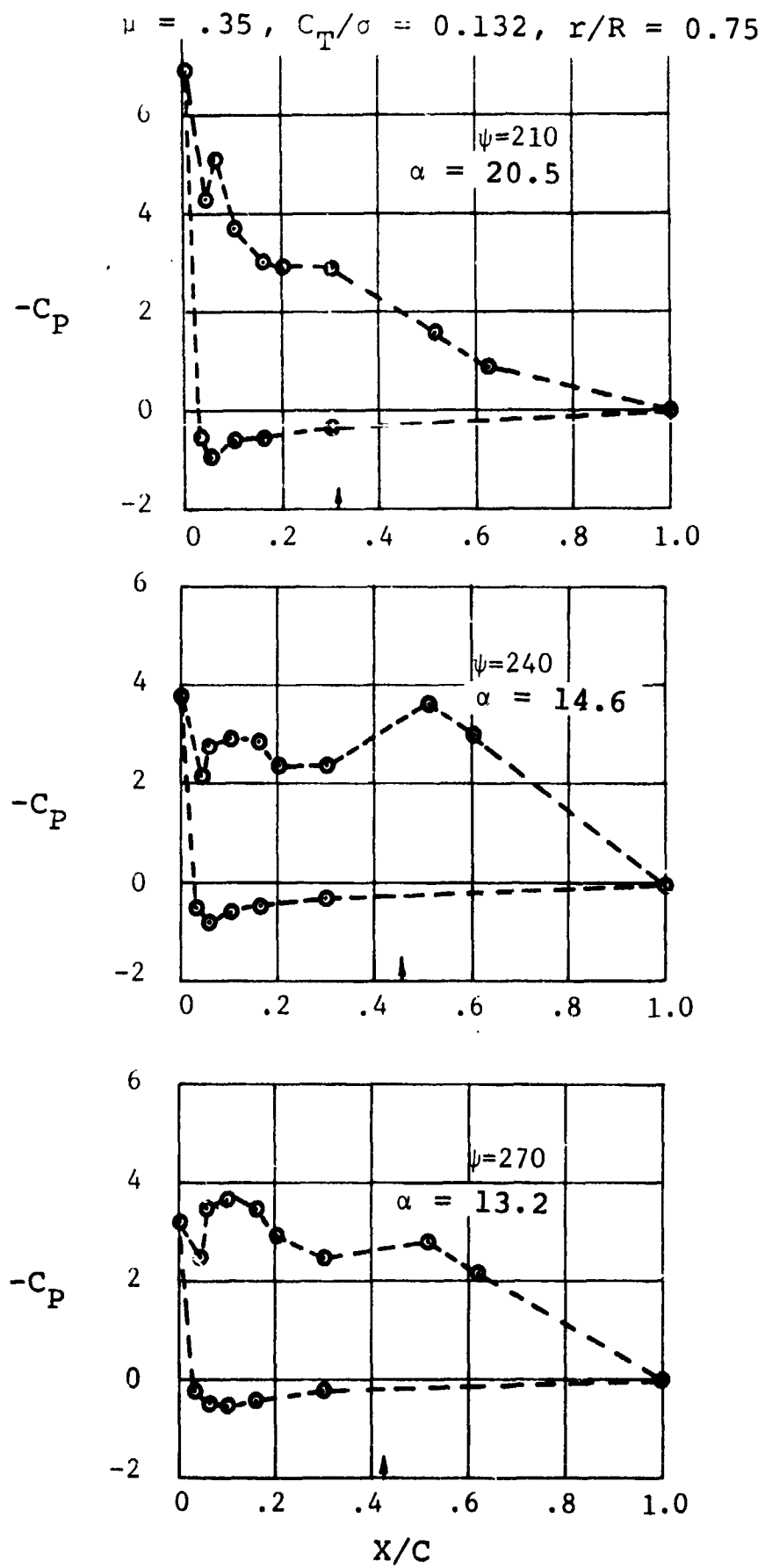


FIGURE 37 PRESSURE DISTRIBUTION AT VARIOUS AZIMUTH LOCATIONS

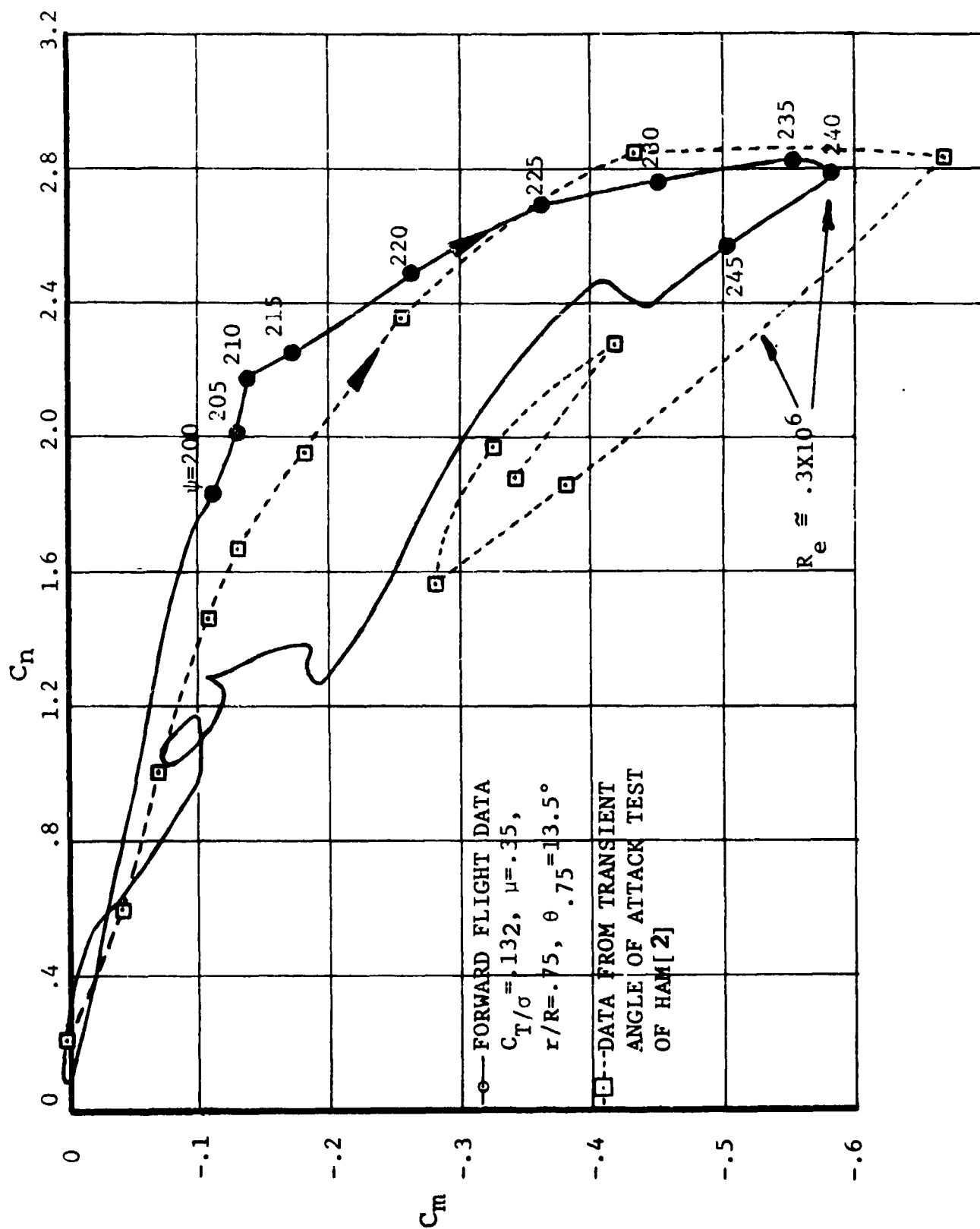


FIGURE 38

COMPARISON OF ROTATING AND NONROTATING
LIFT AND MOMENT DATA

occurrence, the events described during the stalling process can be associated with the shedding of circulation from the leading edge of the airfoil. The large adverse pressure gradients experienced by the airfoil at its leading edge are far above those obtainable statically and probably will exist only as long as the angle of attack is increasing at a large rate. Once the rate of increase of α becomes small, the flowfield becomes unstable and breakdown of the suction peak occurs. Details as to the nature of the circulation shed from the airfoil leading edge are not known at present. However, flow visualization of the process indicates that the shed circulation does not exhibit the properties of a shed vortex. Until further definition for this event can be made, all reference to it will be made as shed circulation. The change in flow characteristics measured in the boundary layer at $\psi = 200$ degrees signals the beginning of breakdown and, as the suction peak collapses, circulation is shed from the leading edge of the airfoil. This shed circulation then appears to sweep back across the airfoil at a velocity significantly less than the local freestream velocity, causing the various stall events as described above to occur. This circulation shedding phenomenon has been observed for some time in 2-dimensional airfoil tests of oscillating wings. It is described by Ham and Young in Reference 9 and further developed in Reference 10. In fact, data presented in Reference 2 arising from a rapid transient high angle of attack change from 0 to 30 degrees on a 2-dimensional wing are strikingly similar to the data being currently discussed and is illustrated in Figure 38 in a C_n versus C_m format.

The sequence of stall events made itself felt on the blade torsion loads and it is interesting to observe the blade torsion waveform shown in Figure 39 with the stall sequence in mind. In this figure, the blade elastic twist, $\Delta\theta_e$, is linearly proportional to the measured torsional moment at the blade root. At $\psi = 210$ degrees, the torsion load begins a rapid nose-down elastic motion in response to the large C_m 's being generated. The largest nose-down motion is reached at $\psi \approx 245$ degrees, coincident with the maximum C_m . With the following reduction in C_m , the blade begins a rapid pitch-up motion and stall flutter has begun. The fact that the blade torsion has followed the blade aerodynamic load at $r/R = .75$ indicates that a significant portion of the blade is experiencing this sequence at the same time as postulated by Tarzanin in Reference 11.

A summary of the series of events leading to complete stall can be obtained through Figure 40. This map, constructed from both pressure and boundary layer measurements, consists of a cross-plot of events from all the test points within the test runs at $\psi = .35$, $V_T = 500$ feet/second, and $\theta_{.75} = 13.5$ degrees. The shaded portion of the figure indicates regions where the airloads can be described as qualitatively two-dimensionally static

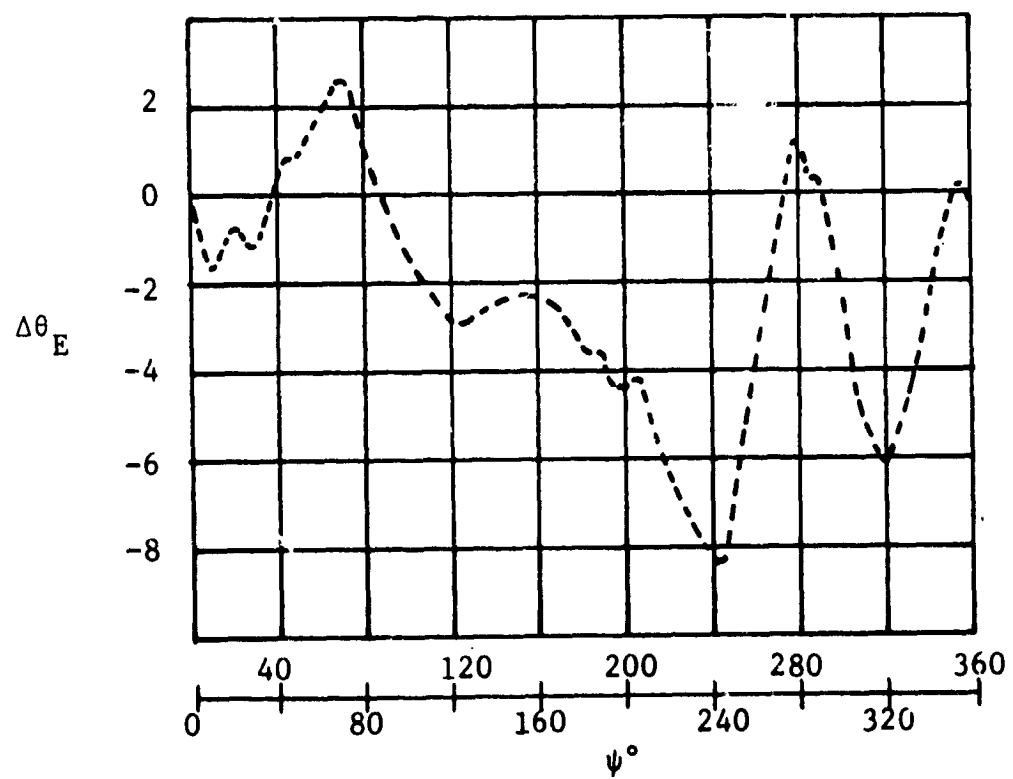
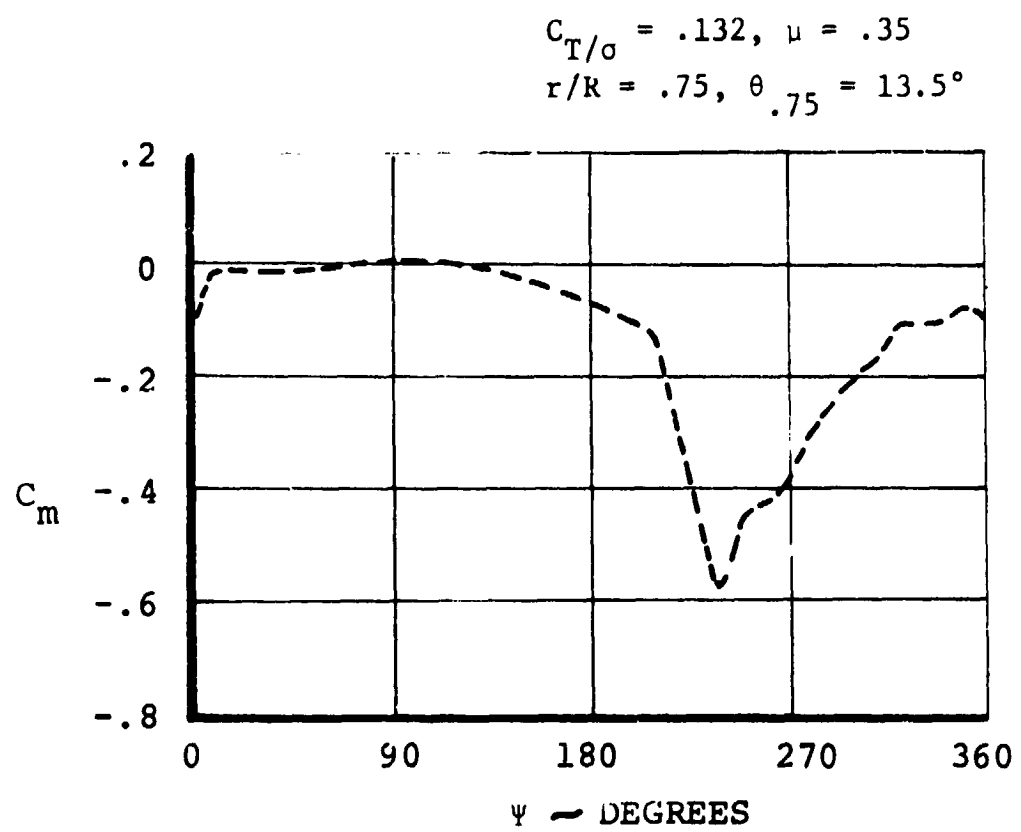
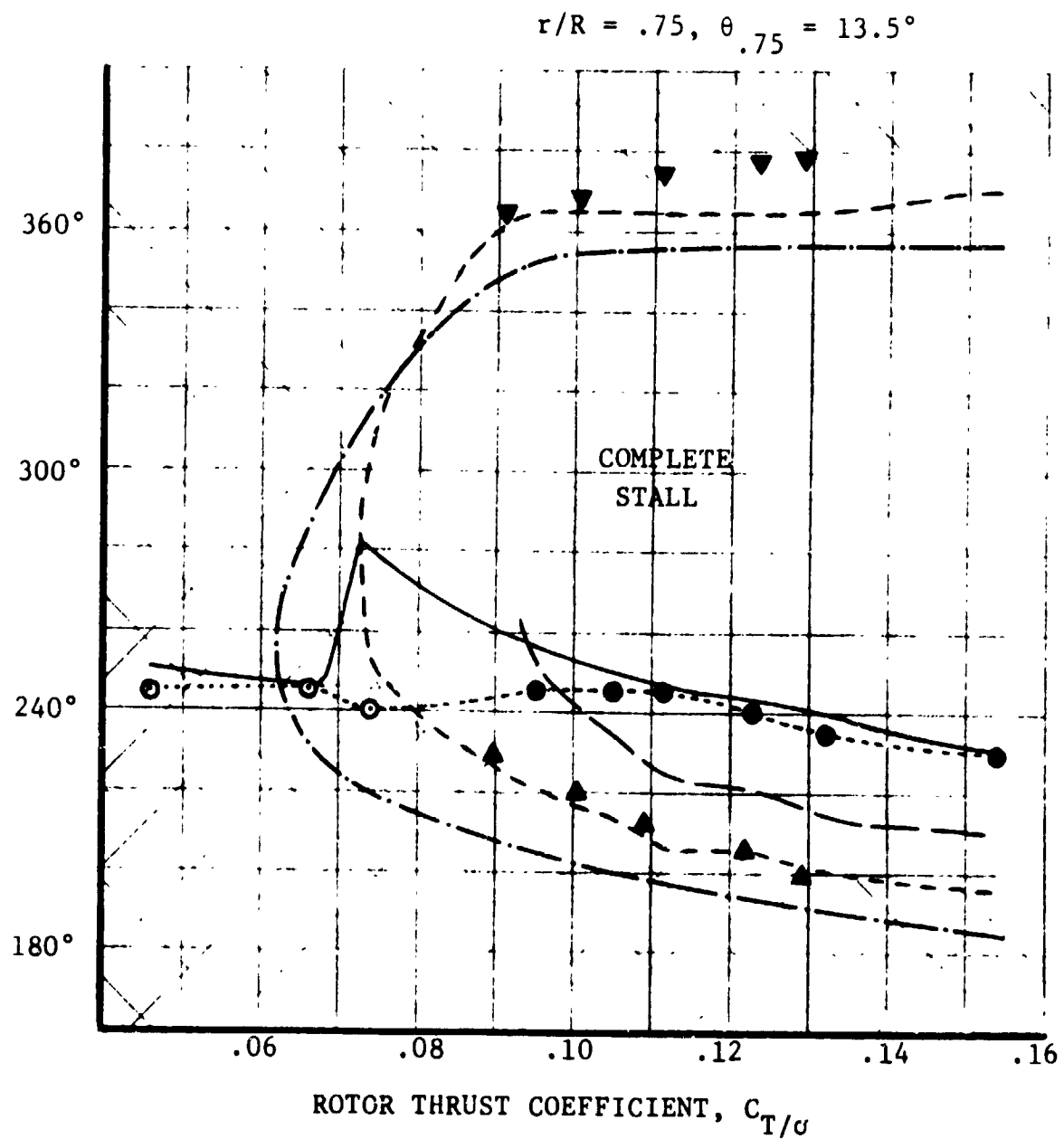


FIGURE 39 BLADE ELEMENT ELASTIC TWIST AND AIRLOADS



SOLID SYMBOLS INDICATE STALLED CONDITIONS

- Δ SKIN FRICTION DATA CHANGES RAPIDLY
- CENTER OF PRESSURE SHIFTS AFT
- LEADING EDGE SUCTION COLLAPSES
- $C_{N_{max}}$ ACHIEVED
- $C_{M_{max}}$ ACHIEVED
- CENTER OF PRESSURE RETURNS TO NORMAL
- ∇ SKIN FRICTION DATA RETURNS TO NORMAL
- STATIC STALL BOUNDARY

FIGURE 40 MAP OF STALL EVENTS, $\mu = .35, V_T = 500 \text{ FPS}$

in nature and quantitatively as two-dimensionally unsteady (like substall oscillating airfoils). The unshaded region indicates regions of retreating blade stall where a classical description of the flow does not suffice. Here the sequence of events that can be consistently identified as leading up to complete blade element stall is shown. These events are:

1. Onset of separation-like disturbances within the boundary layer and a slight shift of the center of pressure.
2. Beginning of a rapid rearward shift of the center of pressure and decrease in C_n .
3. Collapse of the leading edge suction peak.
4. Achievement of maximum C_n .
5. Achievement of maximum C_m .
6. Completion of the stalling process.
7. Re-establishment of leading edge suction.
8. Stabilization of the center of pressure.
9. Re-establishment of normal boundary layer characteristics.

The stall regions illustrated indicate that the rotor first experiences moment stall with the resultant onset of a rapid rise in blade torsional loads and then as the thrust is increased, the rotor experiences both moment and lift stall. The two separately identifiable stall events (Reference 8) exhibit themselves on both blade loads and rotor performance.

The data obtained during the $\mu = .35$, $V_T = 250$ feet/second run, exhibit trends similar to those at $\mu = .35$, $V_T = 500$ feet/second.

Because the measured pressures were a quarter as large, the lower tip speed run required correction for strain effects and zero shift. Figure 41 illustrates the stall region for the low tip speed run. Figure 42 illustrates the correlation of measured C_n and C_m at a $C_T/\sigma = .097$. The fact that the two run results correlate well indicates that the "cuff correction" technique is working well at this advance ratio. It also suggests that the stall events are independent of tip speed within the range of tip speeds tested.

This series of stall events that was observed characterizes the stalling process at the advance ratio of .35. The events seem to support the basic contention of Ham (Reference 10) that retreating blade stall is a dynamic phenomenon of three major phases:

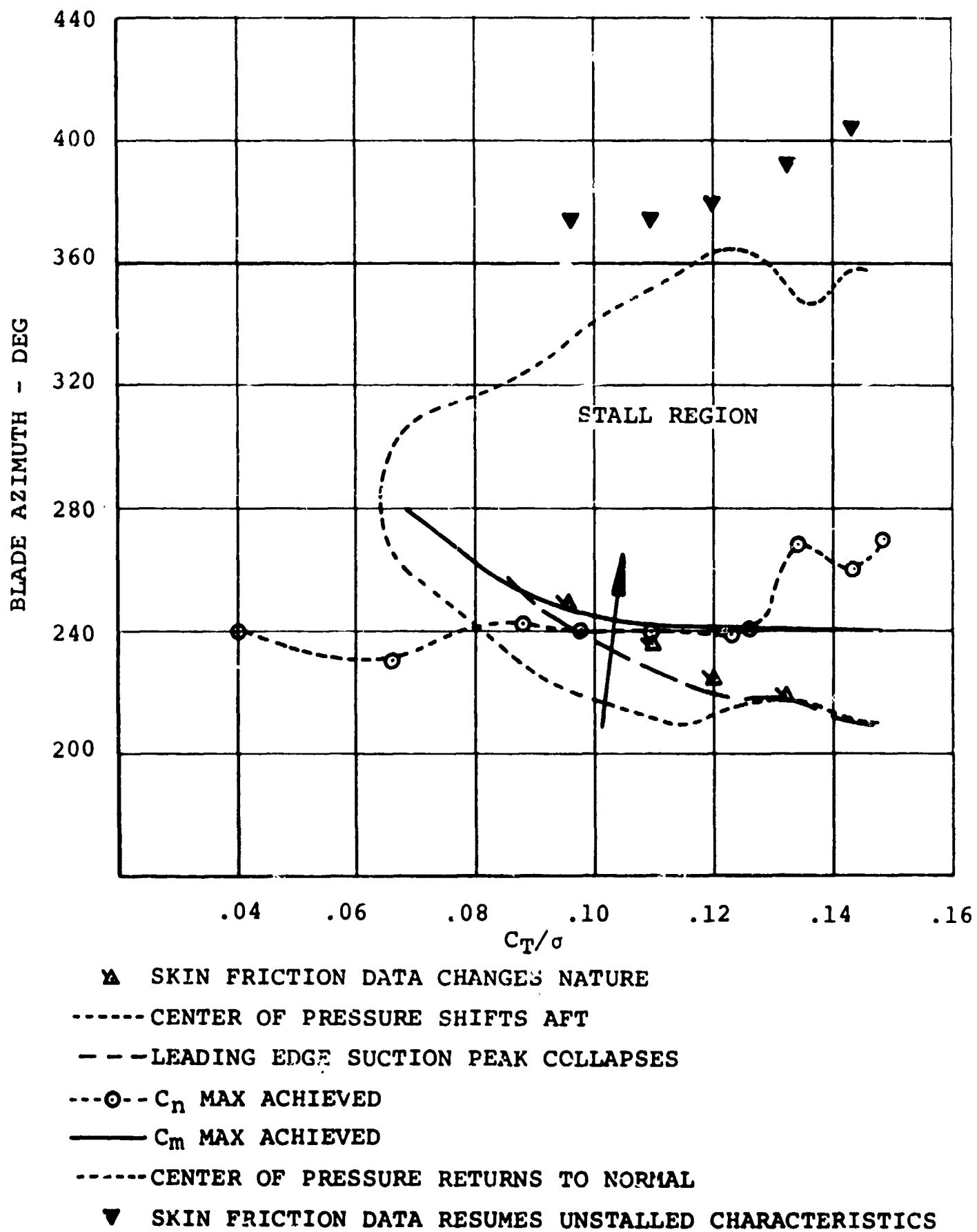


FIGURE 41 MAP OF STALL EVENTS - $\mu = .35$, $V_T = 250$ FPS

— $V_T = 500$ FPS
 - - - $V_T = 250$ FPS

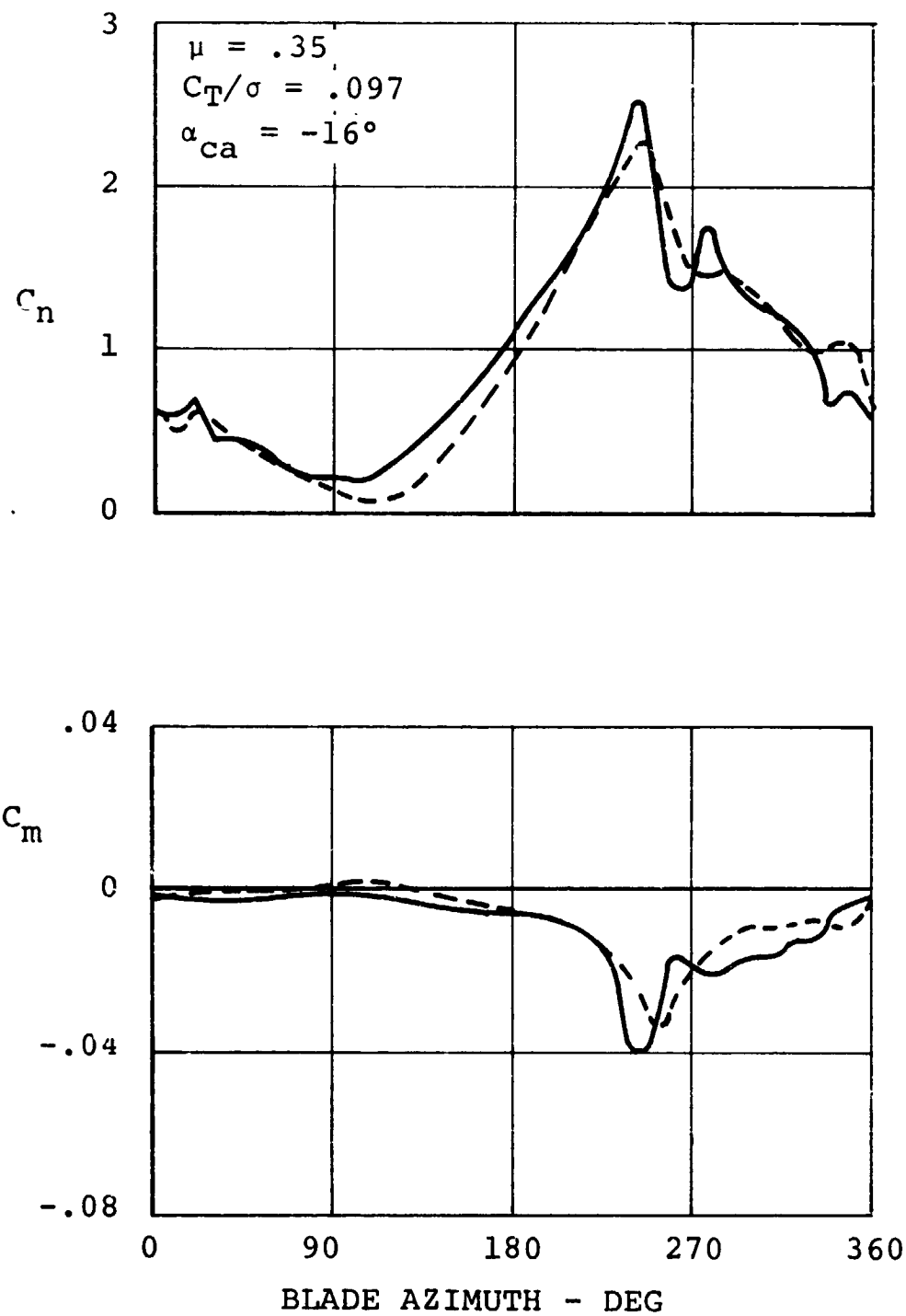


FIGURE 42

COMPARISON OF BLADE ELEMENT AIRLOADS
 AT $V_T = 250$ AND $V_T = 500$ FPS

1. A dynamic overshoot of statically experienced leading edge suction.
2. A subsequent loss of leading edge suction and the shedding of circulation from the leading edge region of the airfoil.
3. Complete upper surface separation.

This present experiment defines the boundaries of these phases more clearly and furnishes additional details of the flowfield development, especially during the onset of stall.

Airloads at an Advance Ratio of .15 - A map of the stall characteristics of the rotor at an advance ratio of $\mu = .15$ and a tip speed of 250 feet/second is presented in Figure 43. Moment stall characteristics indicated by the aft shift in center of pressure begin at rotor thrust coefficients of $C_T/\sigma = .085$. The blade loads obtained at thrust coefficients below this stall level are presented in Figure 44. The values of C_n at $C_T/\sigma = .08$ are well below the static $C_{n_{max}}$ level. The C_m levels, although low, are indicating the onset of moment stall. Figure 45 shows the C_n and C_m trends obtained at the highest thrust tested ($C_T/\sigma = .126$), and Figure 46 shows the C_n versus C_m loop. The associated pressure distributions at $C_T/\sigma = .126$ are given in Figures 47 and 48. These distributions appear similar to the static airfoil pressure distributions obtained in the non-rotating portion of the test when compared at similar angles of attack. A collapse of the leading edge suction and a sharp dropoff in lift with increasing angle of attack, usual indicators of lift stall, did not occur even at this high thrust level. An investigation of the normal force curve of Figure 45 indicates that the maximum C_n experienced in the stall region does not exceed the maximum static C_n value at full scale Reynolds numbers. The airload trends observed from these data indicate that the collapse of the leading edge suction and the rapid changes in the pressure distributions associated with the shedding of circulation from the leading edge do not occur at this Reynolds number and advance ratio.

Because of the low dynamic pressures present at this advance ratio, even the cuff correction technique was not sufficient for the removal of high frequency strain effects. For this reason, the harmonic content of the pressure data was truncated after the 5th harmonic.

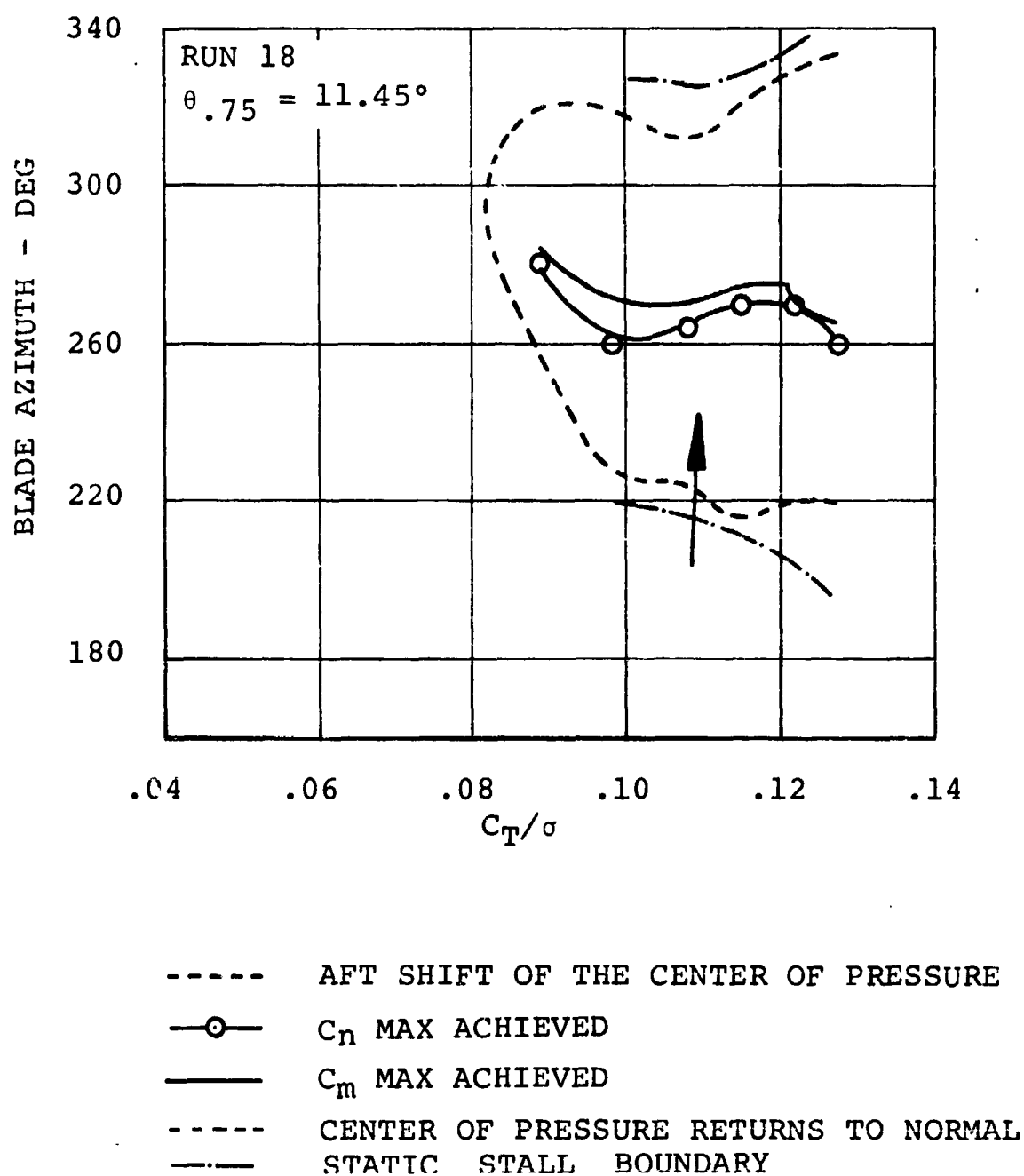


FIGURE 43 MAP OF STALL EVENTS - $\mu = .15$, $V_T = 250$ FPS

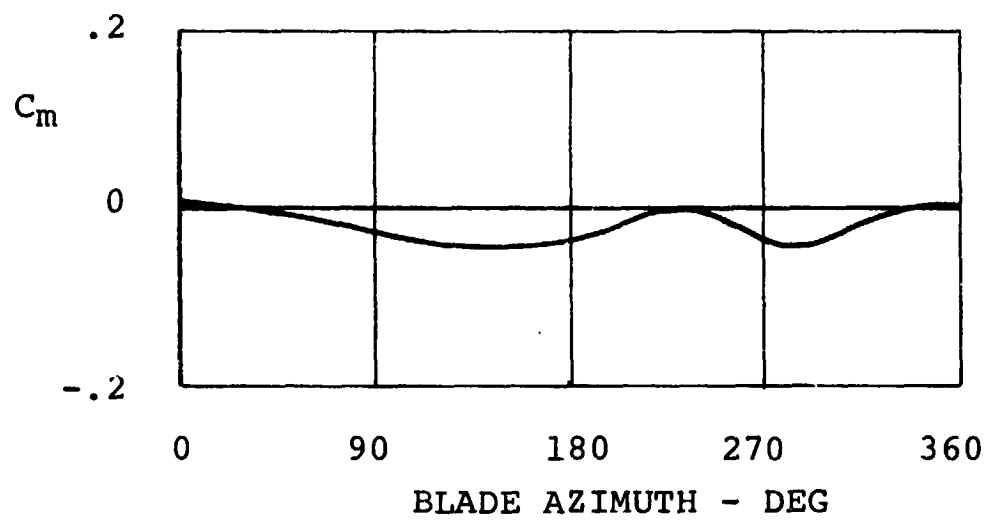
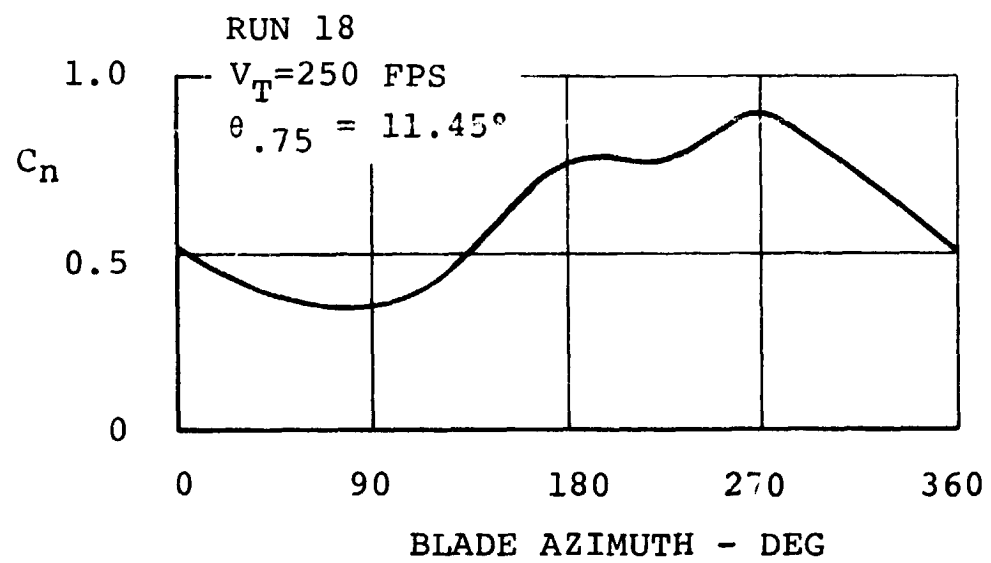


FIGURE 44

BLADE ELEMENT AIRLOADS BELOW STALL
 $\mu = .15, C_T/\sigma = .08$

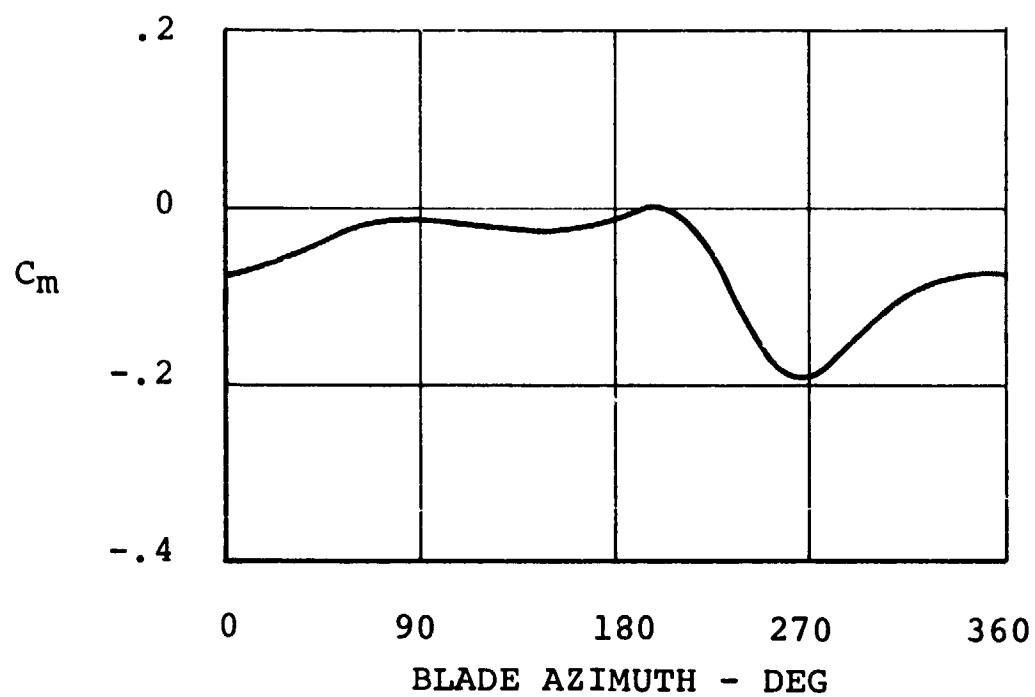
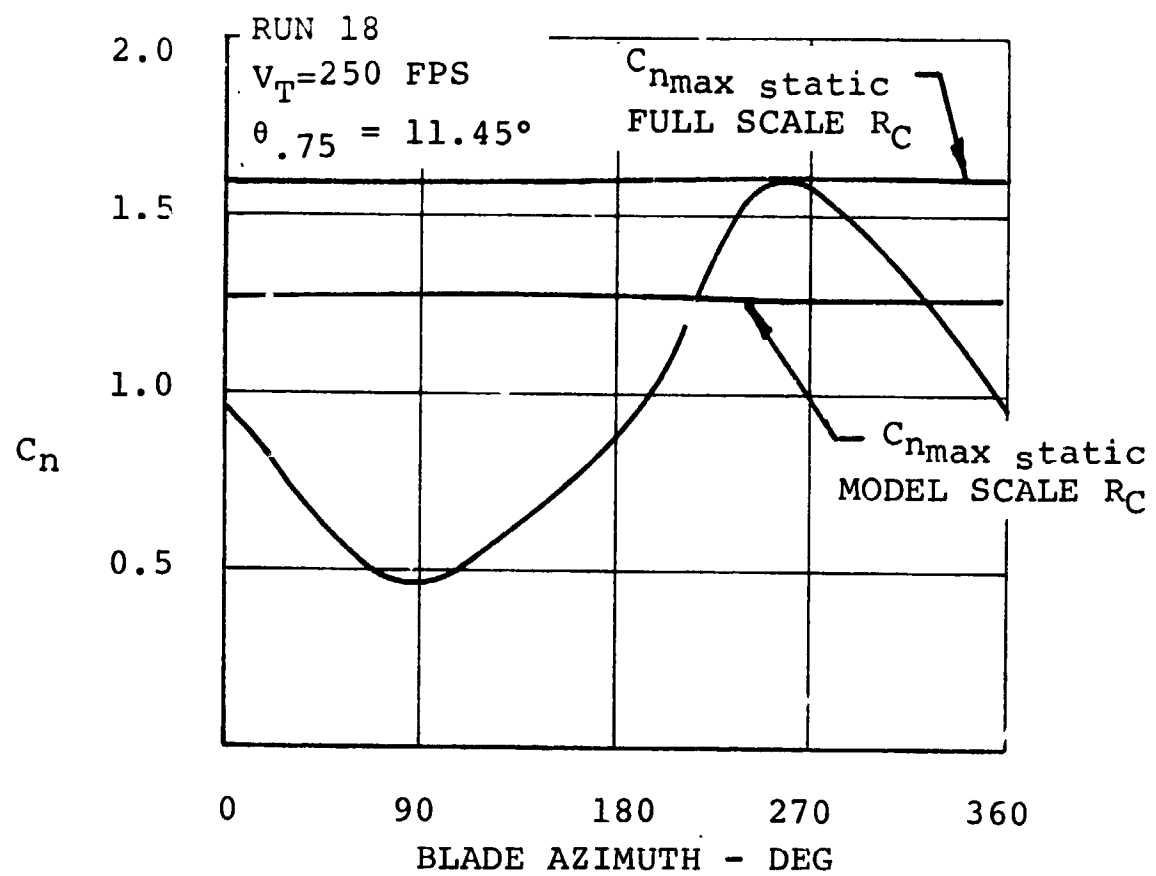


FIGURE 45

BLADE ELEMENT AIRLOADS IN STALL REGION
 $\mu = .15$, $C_T/\sigma = .126$

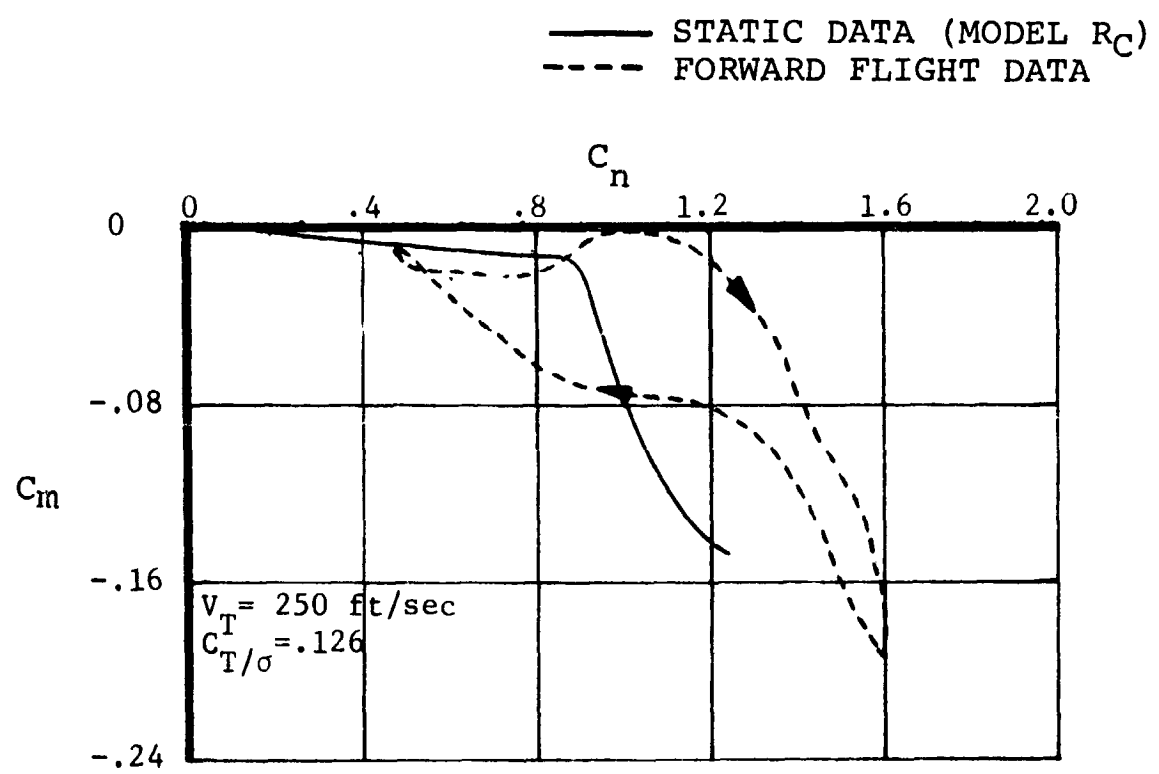


FIGURE 46

BLADE ELEMENT AIRLOADS AT $\mu = .15$

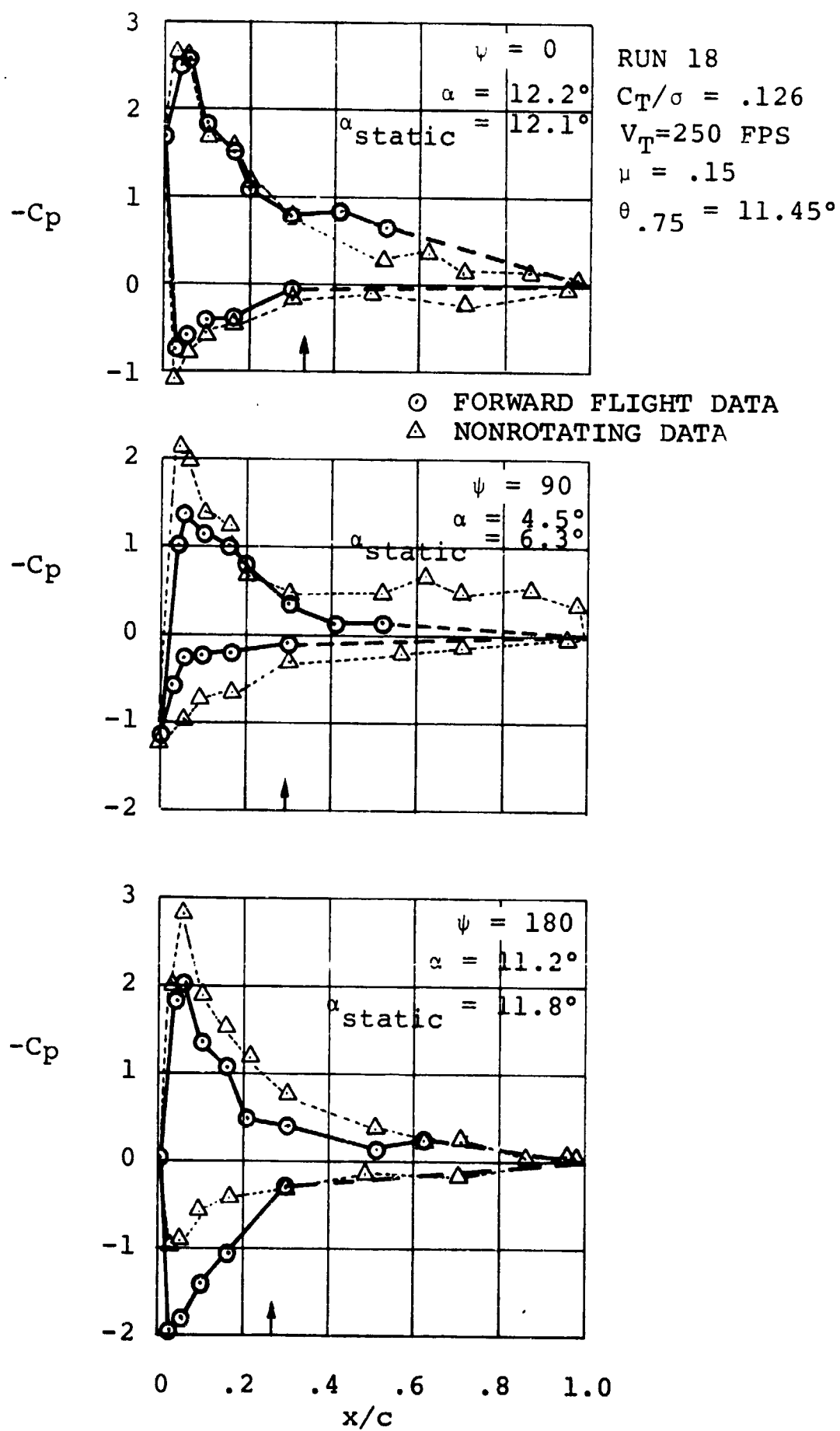


FIGURE 47 BLADE ELEMENT PRESSURE DISTRIBUTIONS

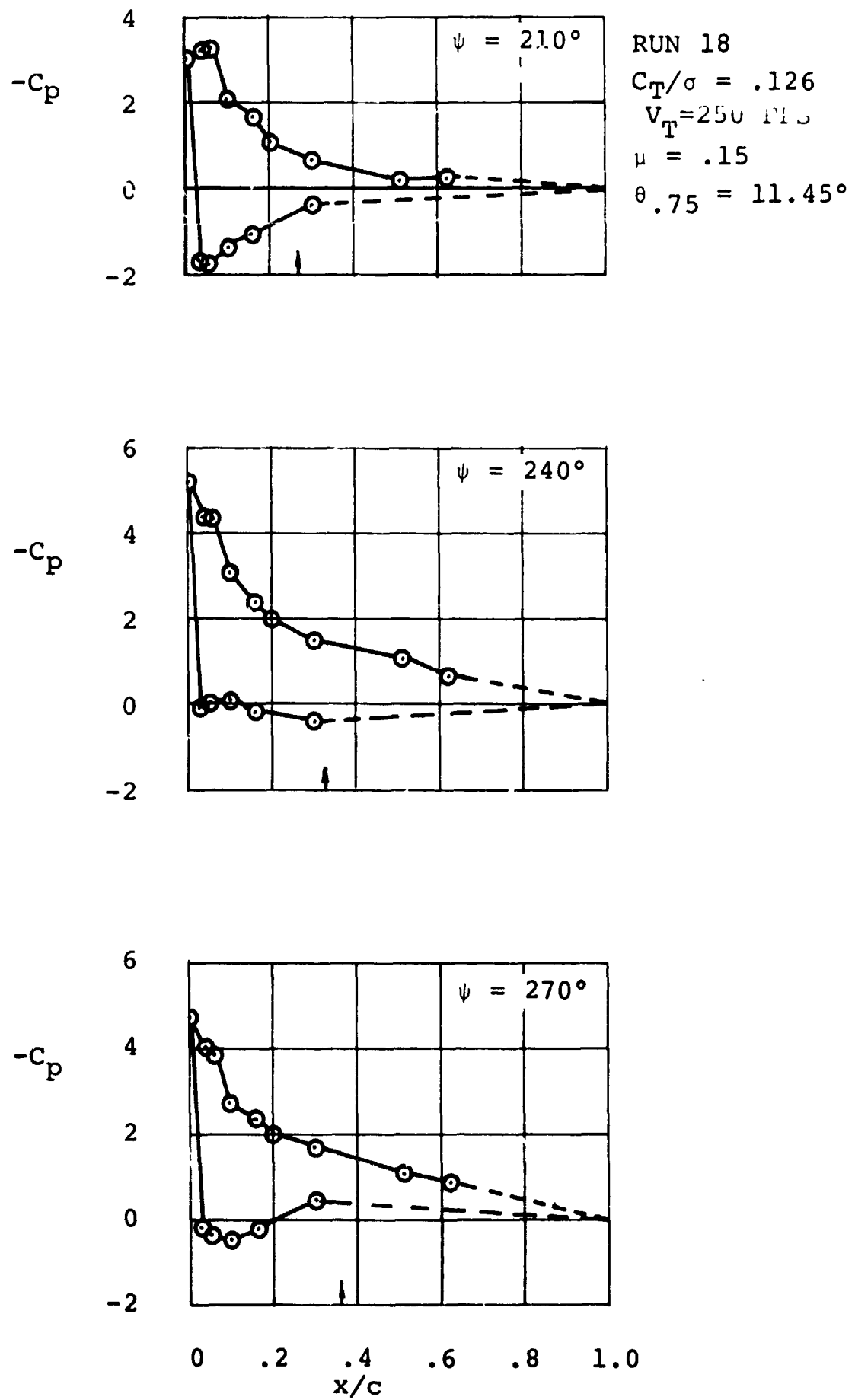


FIGURE 48 BLADE ELEMENT PRESSURE DISTRIBUTIONS

Airloads at an Advance Ratio of .6 - Illustration of the stall characteristics at this advance ratio was obtained at a tip speed of 400 feet/second and a $C_T/\sigma = .09$. Up to stall onset on the retreating side of the rotor disc, the pressure distributions of Figure 49 retain the appearance of unstalled conditions, with well established leading edge suction, even though the measured pressures as well as the integrated results (Figure 51) are greater than those obtained statically. As the blade progresses further in azimuth, Figure 50, the collapse of the leading edge suction and the subsequent shedding of circulation from the leading edge takes place and the stall events similar to those experienced at an advance ratio of $\mu = .35$ occur. The rearward drift of the shed circulation can be traced in the curves of Figure 50 by the movement of the higher pressure area on the upper surface aft with increasing azimuth angle. Figure 52 confirms through a plot of C_n versus C_m that trends of the integrated airloads similar to those obtained at $\mu = .35$ exist at the advance ratio of .6. A similar comparison of the stall events at these two advance ratios can also be seen in the stall map of Figures 53 and 40 at 250 feet/second. At both these advance ratios, the airloads in stall are dominated by the shed circulation due to the collapse of the large leading edge suction obtained through high positive rates of change of angle of attack while the angle of attack itself is high.

The magnitude of the local dynamic pressures on the retreating portion of the rotor disc may have affected the data at this high advance ratio. The calculated local dynamic pressures reach minimum values of .01 psi for the 250 feet/second tip speed run and .03 psi for the 400 feet/second tip speed run. These pressures are on the order of the accuracy of the transducers. The variations in measured pressures and the high steady pressure coefficients of the low q region could, therefore, be due to transducer error, strain effects that were not completely removed by the cuff correction technique, and/or oscillatory pressures inside the cuff. It is also possible that three dimensional effects are playing a larger role at this high advance ratio. Additional work on the pressures measured in the azimuth region between $\psi = 240$ and $\psi = 310$ degrees is required to clarify the source of the pressure coefficients obtained.

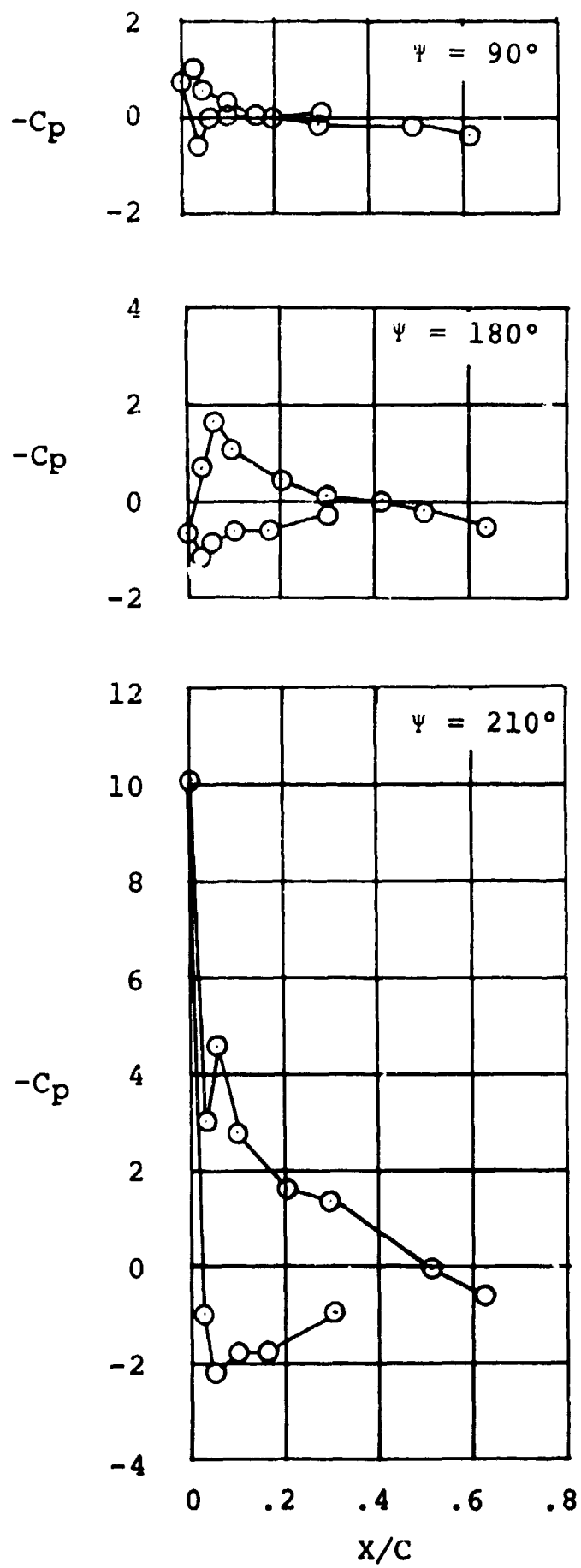


FIGURE 49 BLADE ELEMENT PRESSURE DISTRIBUTIONS AT AN ADVANCE RATIO OF .6, $C_{T/\sigma} = .09$, $V_T = 400$ FPS

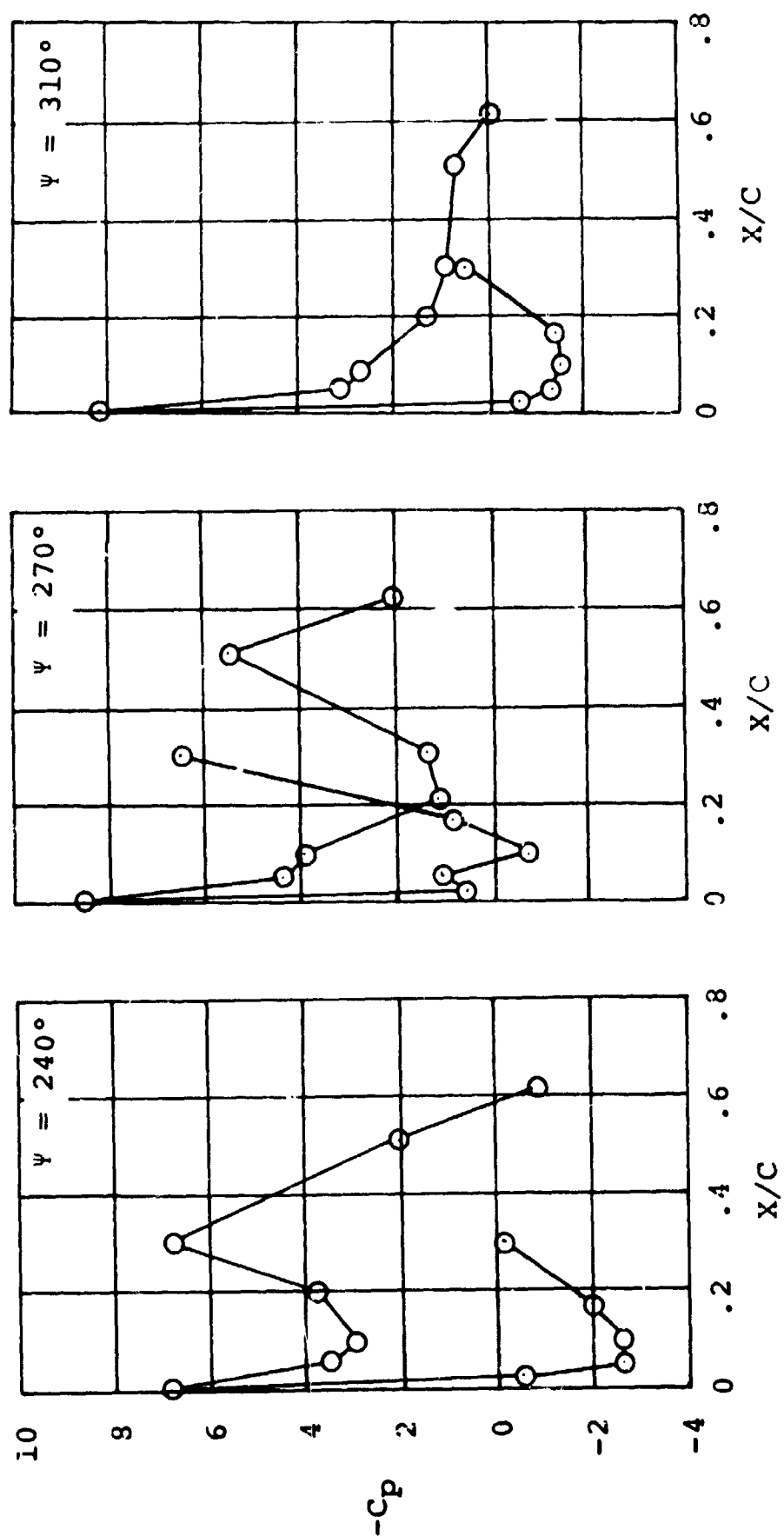


FIGURE 50 BLADE ELEMENT PRESSURE DISTRIBUTIONS AT AN ADVANCE RATIO OF .6, $C_T/\sigma = .09$, $V_T = 400$ FPS

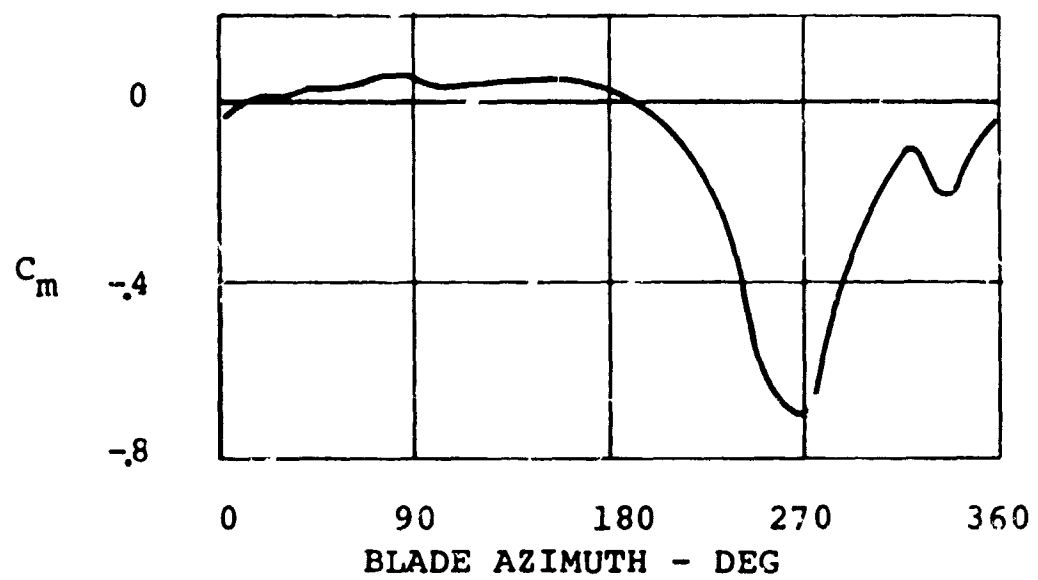
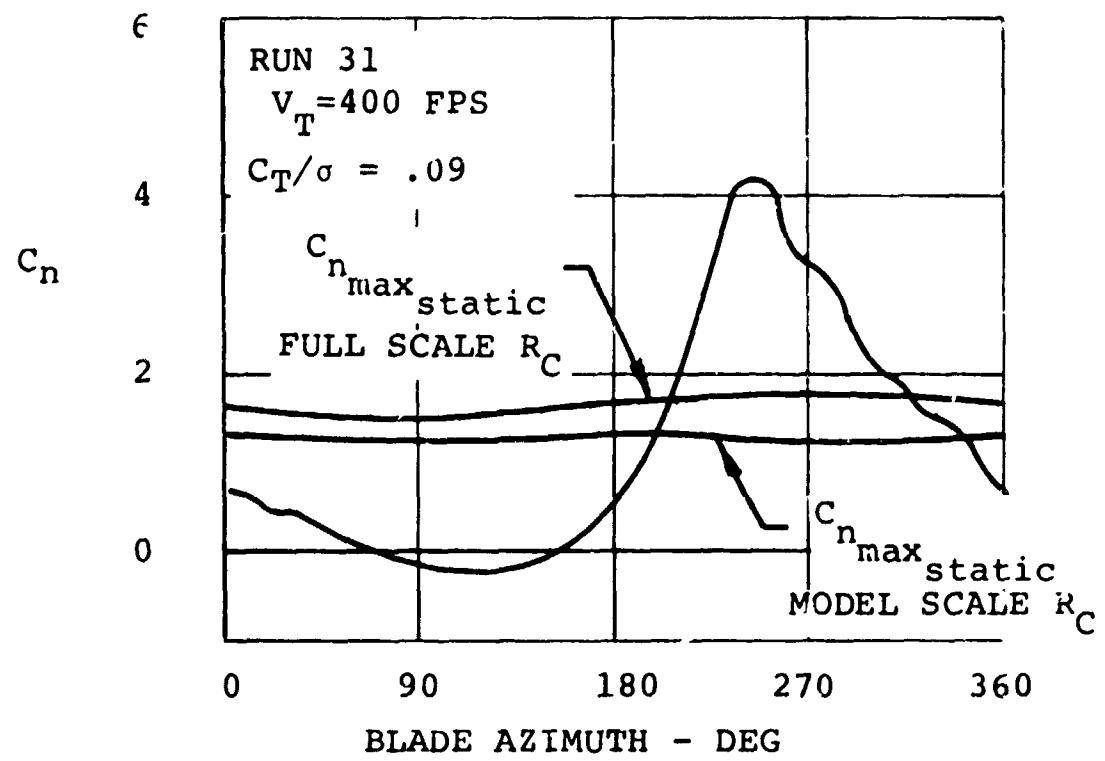


FIGURE 51

BLADE ELEMENT AIRLOADS AT
AN ADVANCE RATIO OF .6

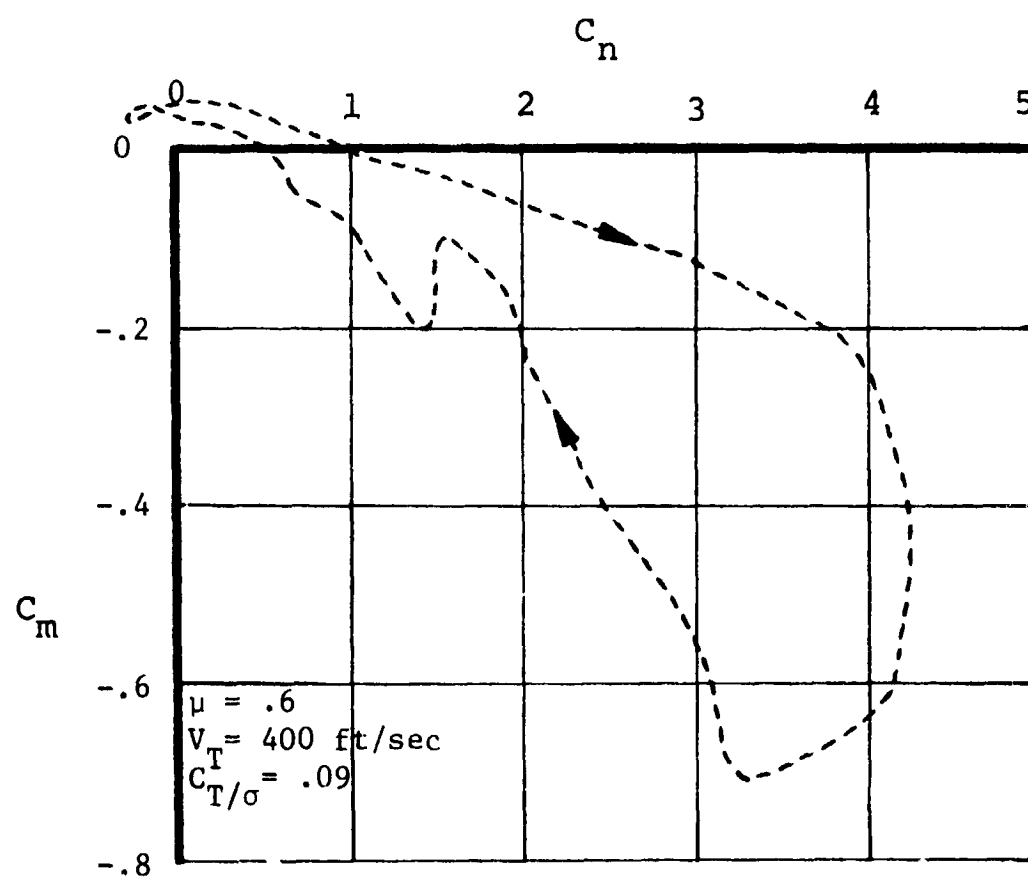


FIGURE 52

BLADE ELEMENT AIRLOADS AT AN
ADVANCE RATIO OF .6

Additional Comments on the Airloads in Stall

A Theory-Test Comparison. - Whether or not airfoil data achieved from two-dimensional testing are applicable to the three-dimensional unsteady rotor environment when the rotor is stalled has been of serious concern to those predicting rotor performance and blade loads. To shed some light on this subject, a theory-test correlation was undertaken with the data previously discussed at a $\mu = .35$, $C_T/\sigma = .132$, $\alpha_s = -3$ degrees, $\theta_{1s} = -5$ degrees, $V_T = 500$ feet/second, and $V = 105$ knots.

Two analyses were used; one analog and one digital. Both utilized the empirical techniques described by Tarzanin in Reference 11 for accounting for the three-dimensional unsteady aerodynamic environment of the rotor blade. The correlation was done in two ways. The first involved the correlation of the test data with the theory run at the rotor test condition. The second utilized a constant angle of attack schedule in the analysis and compared various representations of the aerodynamic theoretical model including quasistatic aerodynamic alone, quasistatic theory with sweep effects, quasistatic theory modified for unsteady aerodynamic effects, and the theory utilizing both the sweep and unsteady aerodynamic effects.

The angle of attack comparison is shown in Figure 54. This schedule of angle of attack was obtained from the angle measured through differential pressure transducer up to an angle of attack of 20 degrees, where the data from the ΔP transducer become unusable for a determination. Above this angle, some engineering judgment was used to construct α from the blade cyclic input, blade live twist, and theoretical blade flapping. The angle of attack was then broken down into θ , U_p , and U_t components.

Figure 55A shows the results when the low Reynolds number airfoil data obtained for the pressure blade during the nonrotating section of the subject model test were used at the constructed angle of attack, along with the unsteady aero effect empiricism obtained from full-scale Reynolds number oscillating airfoil tests. Although the unsteady aerodynamic effects do account for a C_n increase over C_n max predicted when the static data are used exclusively, that max C_n is far short of the one measured at the test point under discussion. At the

$$\mu = .35 \quad C_T/\sigma = .133$$

$$r/R = .75, \theta_{.75} = 13.5$$

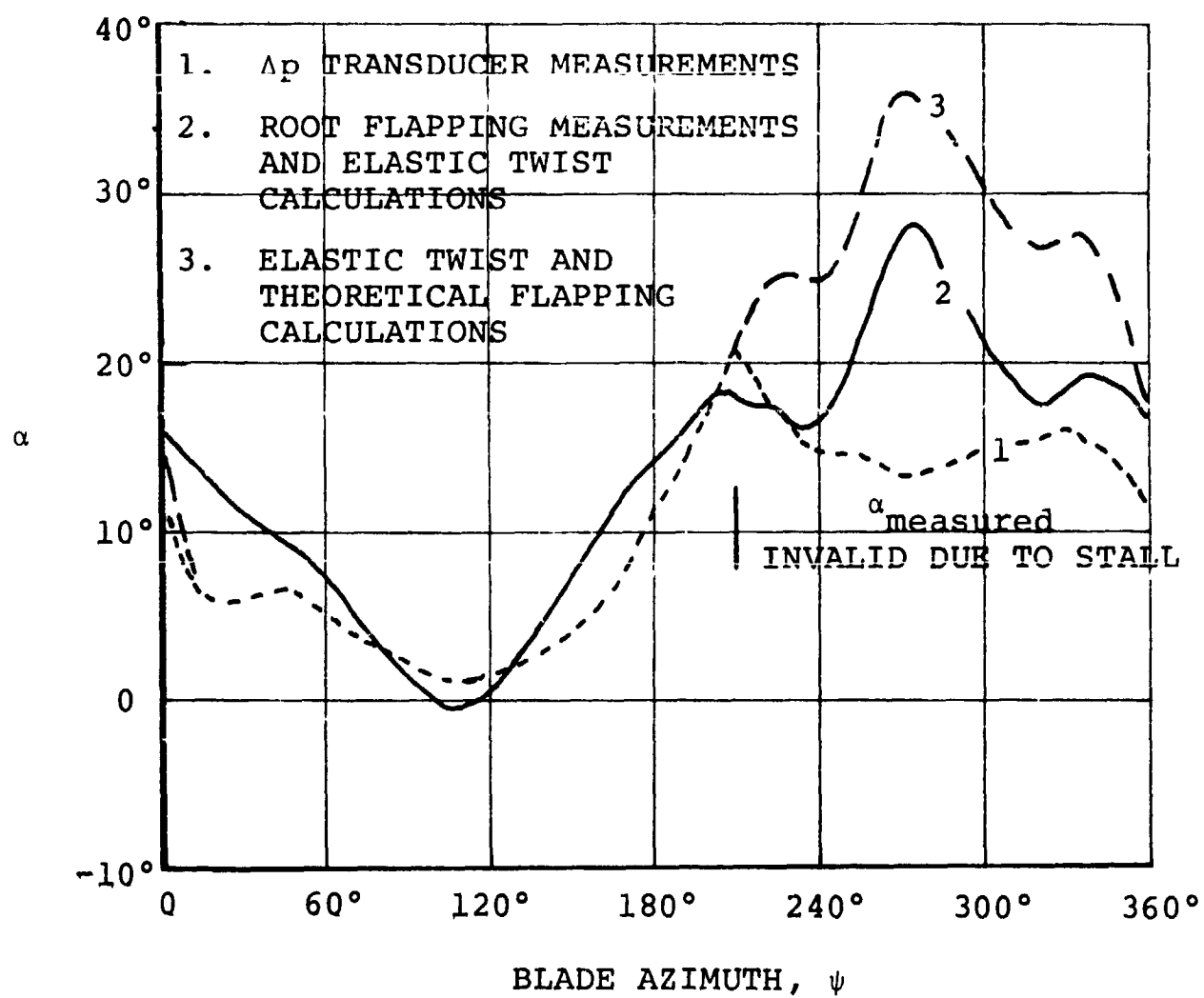
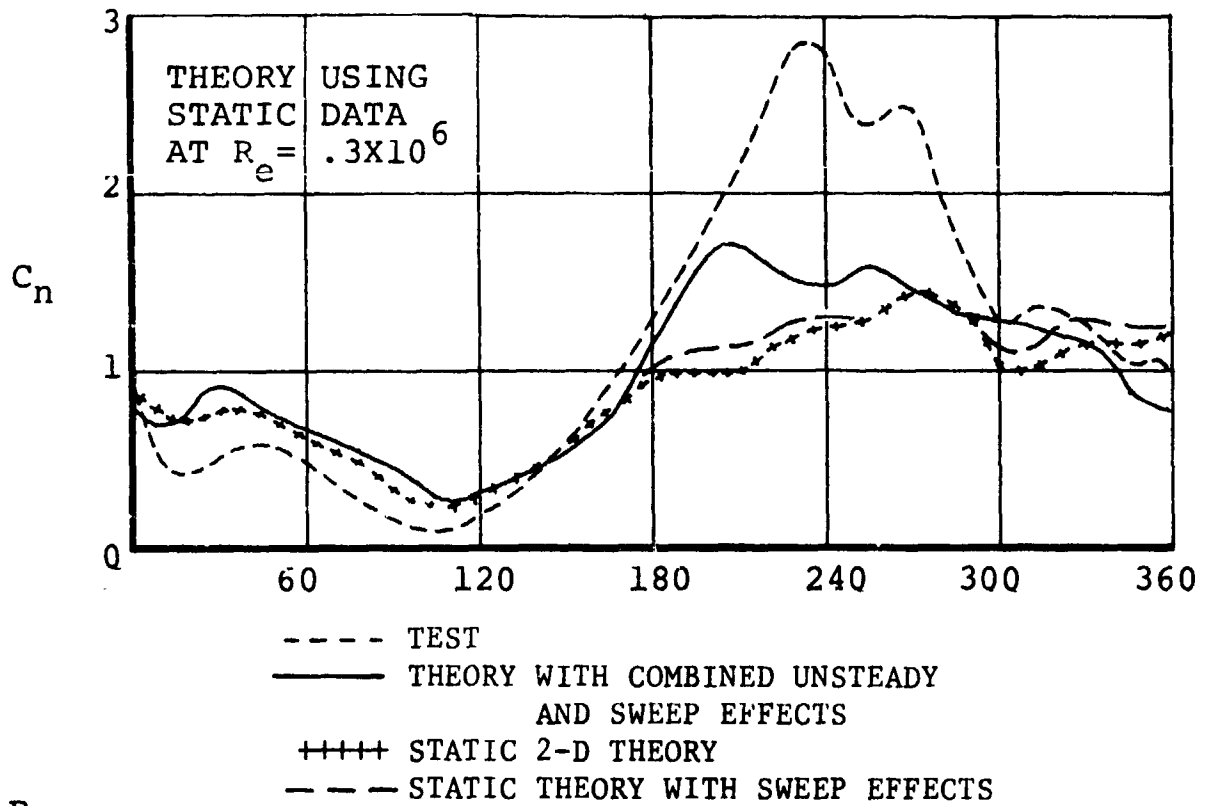


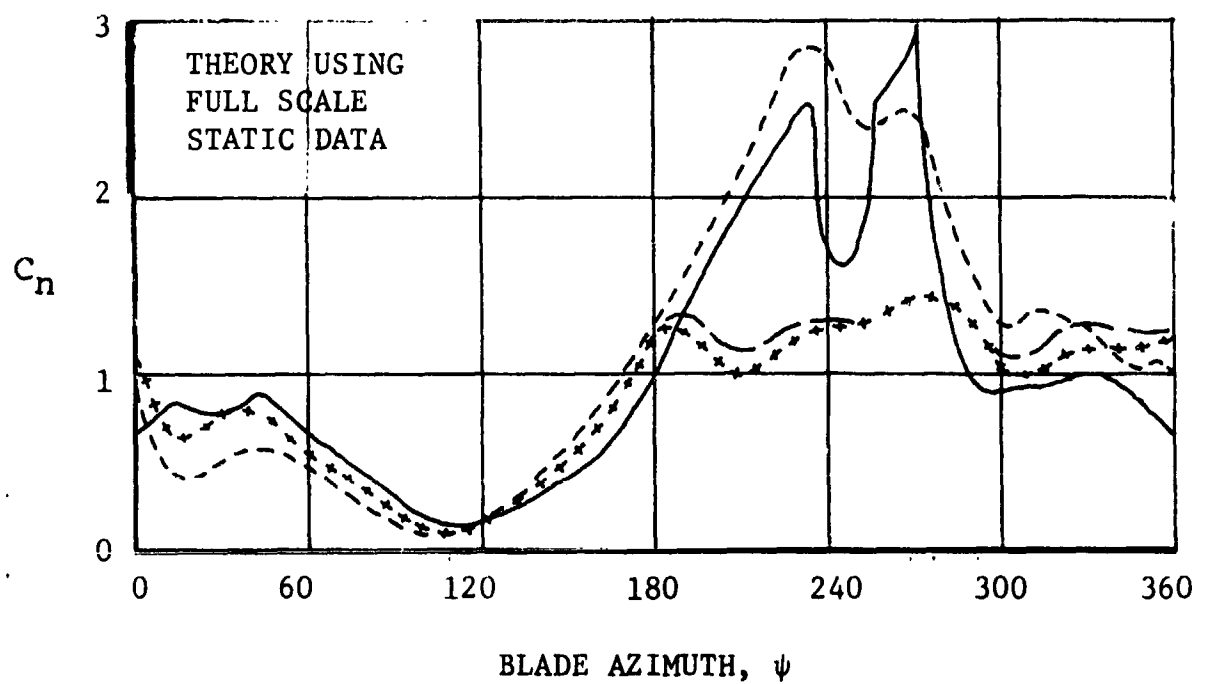
FIGURE 54 COMPARISON OF ANGLES OF ATTACK WITH BLADE STALL

A

$$\mu = .35, C_{T/\sigma} = .132, r/R = .75, \theta_{.75} = 13.5$$



B



THEORETICAL RESULTS INCLUDE PRESCRIBED
ANGLE OF ATTACK SCHEDULE

FIGURE 55 CORRELATION OF THEORETICAL AND EXPERIMENTAL
NORMAL FORCE COEFFICIENTS

C_n max azimuth region, the Reynolds number for the static and rotating data for this test point are the same.

Figure 55B shows the results obtained when full-scale Reynolds number data are utilized. The quasistatic theory alone is still inadequate on the retreating blade and the addition of sweep effects makes little difference. However, the combined three-dimensional unsteady theory results are very encouraging, for prior to C_n max, the correlation is quite good, with theory predicting the C_n versus ψ up to C_n max. This result indicates that the model rotor blade is experiencing airloads similar to those experienced on full-scale rotors. That is, even though the local Reynolds number on the model blades is an order-of-magnitude lower than the full-scale rotor blades, the unsteady aero environment of the blade in the region where C_n is above 1.0 is causing airloads similar to those characteristic of high Reynolds number data.

This result could be explained by interactions between unsteady aerodynamic effects and Reynolds numbers effects. Erickson and Reding (Reference 12) point out that static trailing edge stall can sometimes be converted to leading edge stall by dynamic effects. This could also explain why the data at $\mu = .15$ show stall characteristics similar to the present low Reynolds number static data, while the stall characteristics of $\mu = .35$ and $.6$, where $d\alpha/dt$ gets increasingly larger, resemble dynamic stall with vortex shedding from the leading edge of the airfoil.

After the occurrence of C_n max, the correlation deteriorates and the theory generally underpredicts the measured airloads. However, the brief rise in C_n after stall, associated theoretically (Reference 12) to re-establishment of a sufficiently high increase in α and $d\alpha/dt$ because of blade stall flutter (Figure 30) is both predicted and measured. The fact that the general level of the measured C_n values obtained in the azimuth region from $\psi = 240$ to $\psi = 360$ degrees are so large is contrary to most expectations, for those measured C_n 's remain well above the static values of C_n max, even for airfoils at full-scale Reynolds numbers. This lack of correlation can possibly be attributed to the lack of understanding of sweep and plunging effects on airfoils in stall, for it is in this region of the azimuth where plunging is large. Although much work has been done with airfoils oscillating in pitch, both in and out of stall, little work has been done with plunging airfoils in stall. What correlation with current theory has

been done indicates serious deficiencies when the airfoil is stalled.

A comparison of measured normal force coefficients with theoretically predicted normal force coefficients, run at the rotor test condition with no constraints on angle of attack, is given in Figure 56. In this figure, an improvement over the correlations shown in Figure 55 is observed in the segment of the rotor disc between the azimuths of 90 degrees and 210 degrees. This improvement over the results obtained from the specified angle of attack method of correlation is directly attributed to the $\dot{\alpha}$ effects on the differential pressure transducer incorporated for measuring the angle of attack. The measured α lags the true α in the region of ψ where α is increasing. The correlation obtained is shown in Figure 56.

Aerodynamic Uncertainties - It should be finally mentioned that the airloads in the complete stall regime, where the theory-test correlation deteriorates, are sensitive to blade-element angles of attack and local velocities. The values of local velocity that were inferred from C_p max exceeded the theoretical values consistently in the stall regime and the values of angle of attack inferred from the differential pressure were unusable in the stall regime. Both plunging and pitching motion make up the classical angle of attack, and whether this is a unique parameter as far as the blade element airloads is concerned is questionable and has not been answered by this experiment. The results of this investigation do indicate that local velocities were estimated satisfactorily prior to stall, and that the angle of attack is directly related to the blade element airloads. However, determination of V_{local} , and the meaning of α in stall remains a formidable challenge in experimental rotor aerodynamics research.

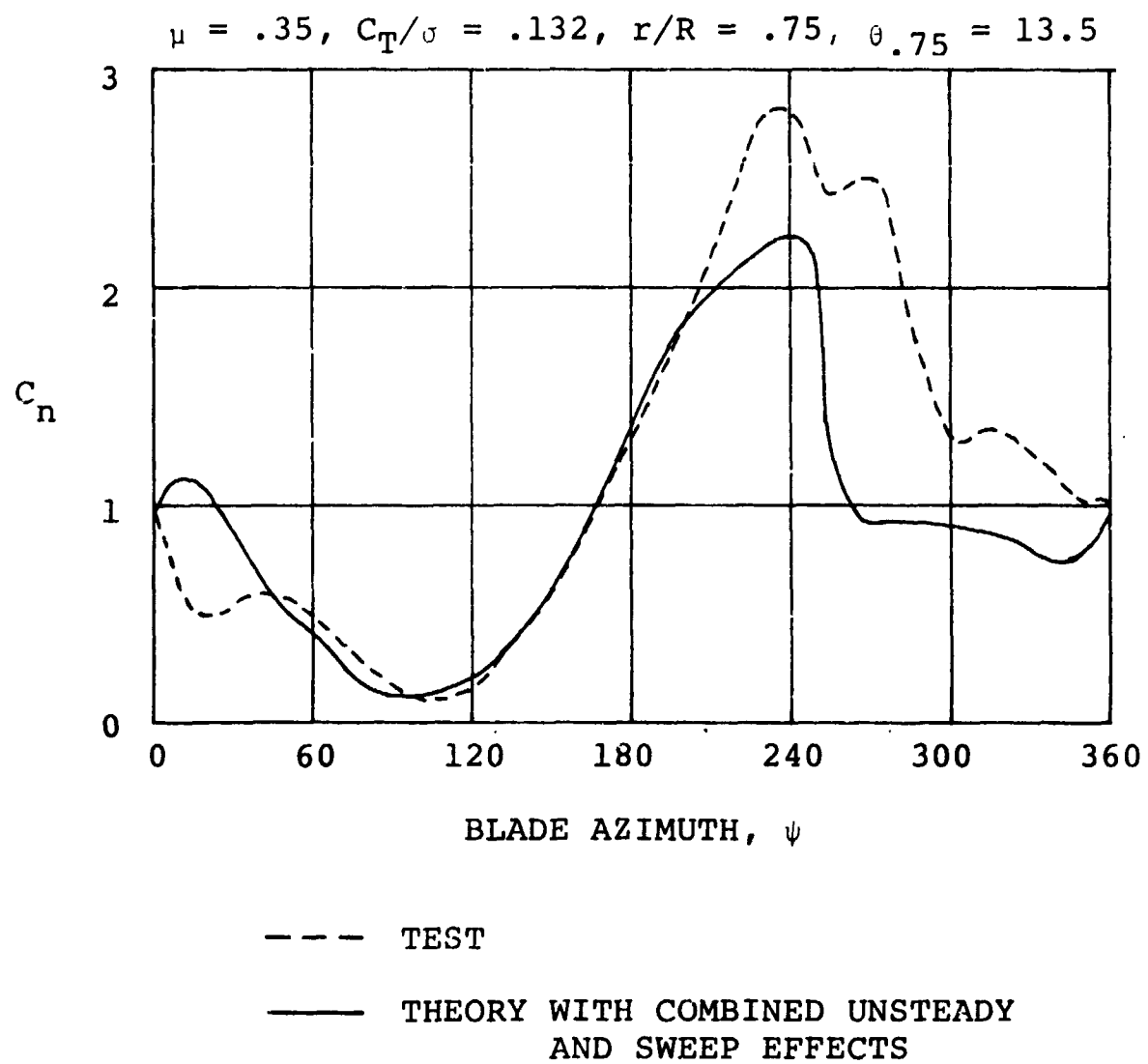


FIGURE 56

CORRELATION OF THEORETICAL AND EXPERIMENTAL
NORMAL FORCE COEFFICIENTS

CONCLUSIONS

The flowfield around a helicopter rotor blade in forward flight is generally acknowledged to be complex, unsteady, and three-dimensional. The results of this experimental investigation confirm some existing conclusions about the airloads of the flowfield, as well as permit certain new conclusions to be drawn about the nature of the flowfield and airloads experienced by the blades.

1. On the advancing blade region of the rotor disc, as well as during the onset of retreating blade stall, the three-dimensional nature of the flowfield does not significantly affect the blade-element airloads. Rather, the normal forces and moments resemble those that have been observed on two-dimensional airfoils oscillating in pitch and undergoing transient changes in angle of attack.
2. The rate of change of the local blade element angle of attack appears to be one of the primary factors that determines the departures from static theory on the advancing blade and during the delay in the onset of stall on the retreating blade. It also appears that the pitch rates encountered in high-speed flight, where $d\alpha/dt$ is high, tend to induce dynamic leading edge stall, regardless of the static stall characteristics.
3. Retreating blade stall is a series of separate events that build up over a significant segment of the rotor azimuth, rather than a single breakdown of the local flowfield. Previously observed distinctions between "lift stall" and "moment stall" occur because of the dynamic nature of this series of events as circulation is shed from the airfoil leading edge and passes over the airfoil during a finite time span.
4. The dynamic nature of the stall events is probably the primary reason that the basic stall mechanisms appear to be increasingly dominated by circulation shed from the leading edge of the airfoil as advance ratio increases. However, this does not preclude strong unsteady effects at low values of μ if rapid changes in angle of attack are encountered; i.e., maneuvering flight, blade-vortex intersections, or blade elastic excitations.

5. Contemporary empirical theories that account for three-dimensional unsteady effects can adequately predict blade-element forces and moments in the advancing blade and during the onset of stall but not after the blade stalls completely. The shortcomings are related to uncertainties in the angle of attack, in local blade element dynamic pressures, as well as in the basic behavior of unsteady three-dimensional separated flows.

The present experimental investigation has explored the mechanisms of retreating blade stall at one spanwise location of the rotor blade a little more deeply but much remains to be done. A continued investigation of the data obtained during the subject test program, as well as a review of other existing data, is proceeding.

APPENDIX

DATA REDUCTION PROGRAM Y-54

APPENDIX

DATA REDUCTION PROGRAM Y-54

A computer program has been developed which reduces data obtained during the pressure blade portion of the subject test program to useful engineering parameters. Data from pressure transducers, blade motion sensors, and blade loads gages are input to the program in harmonic coefficient form, along with data characterizing the rotor flight condition. These data are then operated on to provide time histories of the rotor blade environment, including: calculation of the blade element velocities, pressure coefficients, angle of attack, blade position, and blade motion; integration of the pressure data utilizing a trapezoidal technique, and plotting of the data.

Computation

The following calculations are made based on the harmonic input data and the test run condition data. To simplify presentation of these computations, the following ground rules shall be used:

At any given test point, each piece of data can be represented by a series of harmonic coefficients.

Let the steady term of the harmonic series be associated with a subscript (o).

Let the remaining (i) terms of the sin (s) and cos (c) coefficients of the harmonic series have the (ic) and (is) subscripts.

Therefore, the test data can be characterized by the data harmonic coefficients,

$$d = d_o + \sum_{i=1}^{24} (d_{is} \sin i\psi + d_{ic} \cos i\psi)$$

Let each data type be represented by an identification symbol.

Root Flapping	= β
Lead Lag Angle	= γ
Blade Root Torsional Moment	= RT
Pressure	= P_k

k = subscript designating a particular x/c and y/c transducer location. k = 1 to 20

APPENDIX

Additional data defining test conditions required in the calculations are input to the program along with the harmonic coefficients.

I. Flapping Deflection and Motion Normal to Disc Plane

$$\beta = \beta_0 + \sum_{i=1}^n (\beta_{is} \sin i\psi + \beta_{ic} \cos i\psi) \sim \text{Degrees}$$

$$\dot{\beta} = \frac{\pi}{180} \sum_{i=1}^n \Omega i (\beta_{is} \cos i\psi - \beta_{ic} \sin i\psi) \sim \text{Radians/Sec.}$$

$$\ddot{\beta} = \frac{\pi}{180} \sum_{i=1}^n (\Omega i)^2 (-\beta_{is} \sin i\psi - \beta_{ic} \cos i\psi) \sim \text{Radians/Sec.}^2$$

II. Lead Lag Deflection and Motion in the Disc Plane

$$\gamma = \gamma_0 + \sum_{i=1}^n (\gamma_{is} \sin i\psi + \gamma_{ic} \cos i\psi) \sim \text{Degrees}$$

$$\dot{\gamma} = \frac{\pi}{180} .75R \sum_{i=1}^n (\Omega i) (\gamma_{is} \cos i\psi - \gamma_{ic} \sin i\psi) \sim \text{Ft./Sec.}$$

$$\ddot{\gamma} = \frac{\pi}{180} .75R \sum_{i=1}^n (\Omega i)^2 (-\gamma_{is} \sin i\psi - \gamma_{ic} \cos i\psi) \sim \text{Ft./Sec.}^2$$

III. Blade Element Feathering Motion-Elastic Twist

$$\theta_E = K \left[R_{T0} + \sum_{i=1}^n (R_{Tis} \sin i\psi + R_{Tic} \cos i\psi) \right] \sim \text{Degrees}$$

$$\dot{\theta}_E = K \left[\sum_{i=1}^n (\Omega i) (R_{Tis} \cos i\psi - R_{Tic} \sin i\psi) \right] \sim \text{Degrees/Sec.}$$

$$\ddot{\theta}_E = K \left[\sum_{i=1}^n (\Omega i)^2 (-R_{Tis} \sin i\psi - R_{Tic} \cos i\psi) \right] \sim \text{Degrees/Sec.}^2$$

K = Deg/in-lb derived from first
modal properties

Kt_i = root torsion moment harmonics

APPENDIX

Total Feathering

$$\theta = \theta_0 + .75 \theta_T + \theta_{1c} \cos \psi + \theta_{1s} \sin \psi + \theta_E \sim \text{Degrees}$$

$$\dot{\theta} = \frac{\pi}{180} \left[(\Omega)(-\theta_{1c} \sin \psi + \theta_{1s} \cos \psi) + \dot{\theta}_E \right] \text{ Radians/Sec.}$$

$$\ddot{\theta} = \frac{\pi}{180} \left[(\Omega)^2 (-\theta_{1c} \cos \psi - \theta_{1s} \sin \psi) + \ddot{\theta}_E \right] \text{ Radians/Sec.}^2$$

IV. Determination of Three-Quarter Radius Velocities and Mach No.

$$u_P = \Omega R \lambda_s - .75 R \dot{\beta} - V_\infty (\cos \alpha_s) \left(\frac{\pi}{180} \beta \right) (\cos \psi) \sim \text{Ft./Sec.}$$

$$u_T = .75 \Omega R + V_\infty (\sin \psi) (\cos \alpha_s) + \dot{Y} \sim \text{Feet/Sec.}$$

$$V_{Loc} = [u_P^2 + u_T^2]^{1/2} \sim \text{Feet/Sec.}$$

$$M^\# = V_{Loc} / a$$

$$\dot{u}_P = -.75 R \ddot{\beta} - V_\infty (\cos \alpha_s) (\dot{\beta}) (\cos \psi) + V_\infty (\cos \alpha_s) \left(\frac{\pi}{180} \beta \right) (\Omega) (\sin \psi) \sim \text{Feet/Sec.}$$

$$\dot{u}_T = \Omega (V_\infty) (\cos \psi) (\cos \alpha_s) + \ddot{Y} \sim \text{Feet/Sec.}^2$$

$$R_c^\# = \frac{\rho V_{Loc} C}{\left[340.8 + .584 \left(\left(\frac{a}{49.1} \right)^2 - 459.6 \right) \right] \times 10^{-9}}$$

V. Determination of Reduced Frequency

$$h_1 = \frac{c \Omega}{2 V_{Loc}}$$

APPENDIX

VI. Determination of Pressures

$$PTO1 = P_{01_0} + \sum_{i=1}^n (P_{01_{iS}} \sin i\psi + P_{01_{iC}} \cos i\psi) \sim \text{PSI.}$$

$$PTO2 = P_{02_0} + \sum_{i=1}^n (P_{02_{iS}} \sin i\psi + P_{02_{iC}} \cos i\psi) \sim \text{PSI.}$$

.

.

.

$$PT19 = P_{19_0} + \sum_{i=1}^n (P_{19_{iS}} \sin i\psi + P_{19_{iC}} \cos i\psi) \sim \text{PSI.}$$

$$DPO1 = DP_{01_0} + \sum_{i=1}^n (DP_{01_{iS}} \sin i\psi + DP_{01_{iC}} \cos i\psi) \sim \text{PSI.}$$

$$PT20 = PT_{REF} - DPO1$$

$$(D\dot{P}O1) = \sum_{i=1}^n (\Omega i) (DP_{01_{iS}} \cos i\psi - DP_{01_{iC}} \sin i\psi) \sim \text{PSI./sec.}$$

$$(D\ddot{P}O1) = \sum_{i=1}^n (\Omega i)^2 (-DP_{01_{iS}} \sin i\psi - DP_{01_{iC}} \cos i\psi) \sim \text{PSI./sec.}^2$$

VII. Determination of Pressure Coefficients

$$CP_K = (PT_K) \frac{1}{\left(\frac{1}{288}\right) \rho V_{Loc}^2} \quad K = 1, 20$$

$$DCP = (DPO1) \frac{1}{\left(\frac{1}{288}\right) \rho V_{Loc}^2}$$

$$(D\dot{C}P) = (D\dot{P}O1) \frac{1}{\left(\frac{1}{288}\right) \rho V_{Loc}^2}$$

$$(D\ddot{C}P) = (D\ddot{P}O1) \frac{1}{\left(\frac{1}{288}\right) \rho V_{Loc}^2}$$

APPENDIX

VIII. Determination of Angle of Attack

Measured:

$$\alpha_{m_1} = A + B(DCP) + C(DCP)^2 + D(DCP)^3$$

$$\dot{\alpha}_{m_1} = (\dot{DCP}) [B + 2C(DCP) + 3D(DCP)^2]$$

$$\ddot{\alpha}_{m_1} = (\ddot{DCP}) [B + 2C(DCP) + 3D(DCP)^2] + (\dot{DCP})^2 [2C + 6D(DCP)]$$

A, B, C, D = CURVE FIT CONSTANTS SUPPLIED
IN PROGRAM INPUTS.

$$\alpha_{m_{1c}} = \alpha_{m_1} - \text{ARCSIN} \left[\frac{(.19)(C)(\cos \alpha_{m_1})(\dot{\Theta})}{V_{Loc}} \right]$$

Calculated:

$$\alpha_{CALC} = \Theta + \text{TAN}^{-1} (u_p/u_T)$$

$$\dot{\alpha}_{CALC} = \dot{\Theta} + \frac{1}{V_{Loc}^2} (u_T \dot{u}_p - u_p \dot{u}_T)$$

$$\alpha_{m_2} = \frac{C_N - C_{N_0}}{(\partial C_N / \partial \alpha)_0}$$

$$C_{N_0} = C_N @ \alpha = 0^\circ$$

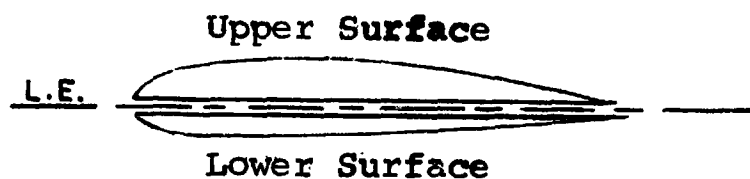
$$(\partial C_N / \partial \alpha)_0 = \left. \frac{\partial C_N}{\partial \alpha} \right|_{\alpha = 0^\circ}$$

APPENDIX

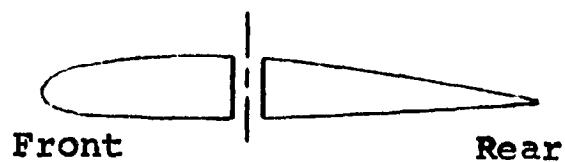
Trapezoidal Integration

For the trapezoidal integration technique, the airfoil is divided into various regions.

- a. for calculation of normal force and associated moments



- b. for calculation of chord force and associated moments



The integration takes place at each where data is reconstituted and uses the pressure coefficients of each transducer.

When the engineering approximation for missing data on the aft of the airfoil is utilized, the program makes a series of pressure coefficients as follows:

APPENDIX

Program Instructions for Including Engineering Approximation

Make following pressure coefficients at the following (x/c, y/c) coordinates:

<u>y/c</u>	<u>x/c</u>	
-.052	.303	Lower Surface
-.044	.5	
-.038	.6	
-.027	.7	
-.012	.85	
-.003	.95	
.00	1.0	
.00	1.0	Upper Surface
.003	.95	
.011	.85	
.026	.70	
.037	.617	

$$C_{P_{y/c}} = C_{P_{x/c}} = .303 \sqrt{\frac{1 - x/c}{.697}} \quad \text{LOWER}$$

$$C_{P_{y/c}} = C_{P_{x/c}} = .617 \sqrt{\frac{1 - x/c}{.383}} \quad \text{UPPER}$$

Include these pressure coefficients in the set for integration when the engineering approximation option is called.

Program Instructions for Doing Trapezoidal Integration

I. Upper Surface Program Instructions

- (1) Sort transducers in ascending x/c order (y/c > 0): Include transducer at x/c = 0 made from the differential pressure.
- (2) Integrate (Cp) on upper surface from x/c = 0 to last available transducer.
- (3) Integrate [(Cp)(x/c)] on the upper surface to get moment due to upper surface.

II. Lower Surface Program Instructions

- (1) Sort transducers in ascending x/c order (y/c < 0): Include transducer at x/c = 0 made from differential pressure.
- (2) Integrate (Cp) on lower surface from x/c = 0 to last available transducer.

APPENDIX

- (3) Integrate $[(C_p)(x/c)]$ on the lower surface to get moment due to lower surface.

III. Front Surface Program Instructions

- (1) Sort transducer into ascending order of y/c from $(y/c < 0)$ to $(y/c > 0)$ for $x/c \leq$ Card input #0012.
- (2) Integrate (C_p) on front surface from $-y/c$ to $+y/c$ over all transducers.
- (3) Integrate $[(C_p)(y/c)]$ on the front surface to get moment due to the front surface.

IV. Rear Surface Program Instructions

- (1) Sort transducers into ascending order of y/c from $(y/c < 0)$ to $(y/c > 0)$ for $x/c \geq$ Card input #0012.
- (2) Integrate (C_p) on rear surface from $-y/c$ to $+y/c$ over all transducers.
- (3) Integrate $[(C_p)(y/c)]$ on rear surface to get moment due to rear surface.

Normal Force Coefficient Calculation

Subtract upper surface integrated pressure coefficients from lower surface integrated pressure coefficients.

$$C_N = C_{N_{\text{LOWER}}} - C_{N_{\text{UPPER}}}$$

Chord Force Coefficient Calculation

Subtract right hand surface integrated pressure coefficients from left hand surface integrated pressure coefficients.

$$C_C = C_{C_{\text{FRONT}}} - C_{C_{\text{BACK}}}$$

Moments About Leading Edge (Nose up +)

Subtract bottom surface integrated moment coefficients from upper surface integrated moment coefficients.

$$\int_0^1 C_p(x/c) d(x/c)$$

APPENDIX

Add the above to the difference between the right hand integrated moment from the left hand surface integrated moment.

$$C_{m_{L.E.}} = C_{m_{L.E. UPPER}} - C_{m_{L.E. LOWER}} + C_{m_{L.E. FRONT}} - C_{m_{L.E. BACK}}$$

Harmonic Integration Option

A program option exists that provides an integration of the harmonic coefficients of pressure.

I. Coordinates of the Pressure Transducers Used for the Harmonic Integration

Upper Surface		Lower Surface	
x/c	y/c	x/c	y/c
XX { 0	-.021	XX { 0	-.021
.041	.010	.033	-.039
.058	.022	.054	-.041
.102	.037	.104	-.045
.158	.045	.165	-.047
.206	.049	.303	-.052
.303	.050	* { .483	-.044
.513	.043	* { .701	-.027
.617	.037	* { .955	-.003
* { .702	.026		
* { .861	.011		
* { .970	.003		

* These transducers will not be present for all cases.

XX This pressure is constructed from a differential pressure.

$$P(0, -.021) = P(.033, -.039) - DP_{01}$$

$$P_0 = P(.033, -.039)_0 - dP_0$$

$$P_{is} = P(.033, -.039)_{is} - dP_{is}$$

$$P_{ic} = P(.033, -.039)_{ic} - dP_{ic}$$

APPENDIX

II. Determination of Pressures Normal to the Chord

Integration is separated into top and bottom surfaces.

Upper Surface:

$$u_o = \int_0^1 p_{Ao} d(x/c)$$

$$u_{is} = \int_0^1 p_{Ais} d(x/c)$$

$$u_{ic} = \int_0^1 p_{Aic} d(x/c)$$

UPPER SURFACE
 p_A AND x/c

$i = 1, 2, 4$

Lower Surface:

$$L_o = \int_0^1 p_{Ao} d(x/c)$$

$$L_{is} = \int_0^1 p_{Ais} d(x/c)$$

$$L_{ic} = \int_0^1 p_{Aic} d(x/c)$$

LOWER SURFACE
 p_A AND x/c

$L = 1, 2, 4$

Total Normal Pressure:

$$N_o = L_o - u_o$$

$$N_{is} = L_{is} - u_{is}$$

$$N_{ic} = L_{ic} - u_{ic}$$

APPENDIX

III. Determination of Pressures Parallel to the Chord

Integration is separated into left and right surfaces.

Left surface $x/c \leq$ Card input value

Right surface $x/c \geq$ Card input value

Left Surface:

$$F_o = \int_{Y/C \text{ MIN}}^{Y/C \text{ MAX}} P_{h_o} d(Y/c)$$

$$F_{ls} = \int_{Y/C \text{ MIN}}^{Y/C \text{ MAX}} P_{h_{ls}} d(Y/c)$$

$$F_{lc} = \int_{Y/C \text{ MIN}}^{Y/C \text{ MAX}} P_{h_{lc}} d(Y/c)$$

LEFT SURFACE
 P_h AND Y/c

$L = 1, 24$

Right Surface:

$$G_o = \int_{Y/C \text{ MIN}}^{Y/C \text{ MAX}} P_{h_o} d(Y/c)$$

$$G_{ls} = \int_{Y/C \text{ MIN}}^{Y/C \text{ MAX}} P_{h_{ls}} d(Y/c)$$

$$G_{lc} = \int_{Y/C \text{ MIN}}^{Y/C \text{ MAX}} P_{h_{lc}} d(Y/c)$$

RIGHT SURFACE
 P_h AND Y/c

$L = 1, 24$

Total Chord Pressure:

$$C_n = F_o - G_o$$

$$C_{ls} = F_{ls} - G_{ls}$$

$$C_{lc} = F_{lc} - G_{lc}$$

APPENDIX

IV. Determination of Moments Due to the Pressures:

Integration is done in four parts:

Upper surface
Lower surface
Left surface
Right surface

Upper Surface:

$$Mu_o = \int_0^1 P_{Ao}(x/c) d(x/c)$$

$$Mu_{is} = \int_0^1 P_{Ais}(x/c) d(x/c)$$

$$Mu_{ic} = \int_0^1 P_{Aic}(x/c) d(x/c)$$

Lower Surface:

$$ML_o = \int_0^1 P_{Ao}(x/c) d(x/c)$$

$$ML_{is} = \int_0^1 P_{Ais}(x/c) d(x/c)$$

$$ML_{ic} = \int_0^1 P_{Aic}(x/c) d(x/c)$$

APPENDIX

Left Surface:

$$MF_o = \int_{Y/c \text{ MIN}}^{Y/c \text{ MAX}} P_{Ao} (Y/c) d(Y/c)$$

$$MF_{is} = \int_{Y/c \text{ MIN}}^{Y/c \text{ MAX}} P_{Ais} (Y/c) d(Y/c)$$

$$MF_{ic} = \int_{Y/c \text{ MIN}}^{Y/c \text{ MAX}} P_{Aic} (Y/c) d(Y/c)$$

Right Surface:

$$MG_o = \int_{Y/c \text{ MIN}}^{Y/c \text{ MAX}} P_{Ao} (Y/c) d(Y/c)$$

$$MG_{is} = \int_{Y/c \text{ MIN}}^{Y/c \text{ MAX}} P_{Ais} (Y/c) d(Y/c)$$

$$MG_{ic} = \int_{Y/c \text{ MIN}}^{Y/c \text{ MAX}} P_{Aic} (Y/c) d(Y/c)$$

Total Moment Pressure:

$$M_o = M_{u_o} - M_{L_o} + MF_o - MG_o$$

$$M_{is} = M_{u_{is}} - M_{L_{is}} + MF_{is} - MG_{is}$$

$$M_{ic} = M_{u_{ic}} - M_{L_{ic}} + MF_{ic} - MG_{ic}$$

APPENDIX

V. Computation of Resultant Harmonic and Phase Angle

$$R_L = \sqrt{(R_{Ls})^2 + (R_{Lc})^2}$$

$$\phi_L = \text{ARC TAN} \left(\frac{R_{Lc}}{R_{Ls}} \right)$$

REFERENCES

1. Gray, L., and Liiva, J., Two-Dimensional Tests of Airfoils Oscillating Near Stall, USAAVLABS TR 68-13, 1968
2. Ham, N.D., and Garelick, M.S., Dynamic Stall Considerations in Helicopter Rotors, Journal of the American Helicopter Society, Vol. 13, No. 2, April 1968
3. Purser, Paul E., and Spearman, M. Leroy, Wind Tunnel Tests at Low Speed of Swept and Yawed Wings Having Various Planforms, NACA TN 2445, December 1954.
4. Harris, F.D., Tarzanin, F.J., and Fisher, R.K., Jr., Rotor High Speed Performance, Theory vs. Test, Journal of the American Helicopter Society, Vol. 15, No. 3, July 1970
5. Lizak, A.A., Two-Dimensional Wind Tunnel Tests of an H-34 Main Rotor Airfoil Section, TREC Technical Report 60-53, September 1960
6. Theodorsen, T., General Theory of Aerodynamic Instability and the Mechanism of Flutter, NACA Report 496, National Advisory Committee for Aeronautics, Washington, D.C., 1935
7. Gessow, A., and Myers, G.C., Aerodynamics of the Helicopter, Frederick Ungar Publishing Co., New York, 1952
8. Harris, F.D. and Pruyn, R.R., Blade Stall - Half Fact, Half Fiction, Journal of the American Helicopter Society, Vol. 13, No. 2, April 1968, pp. 27-48.
9. Ham, N.D., and Young, M.I., Torsional Oscillation of Helicopter Blades Due to Stall, Journal of Aircraft, Vol. 3, No. 3, May-June 1966
10. Ham, N.D., Stall Flutter of Helicopter Rotor Blades: A Special Case of the Dynamic Stall Phenomenon, Journal of the American Helicopter Society, Vol. 12, No. 4, October 1967, pp. 19-21.
11. Tarzanin, F.J., Jr., Prediction of Control Loads Due to Blade Stall, American Helicopter Society 27th Annual National Forum, May 1971

REFERENCES

12. Ericson, L.E., and Reding, J., Unsteady Airfoil Stall, Review and Extension, NASA CR-66787, July 1969